University of Stavanger

Faculty of Science and Technology

MASTER'S THESIS

Study program/Specialization: Petroleum Geosciences Engineering	Spring Semester, 2016 Open
Writer: Rosita Maryam Haftbaradaran	 _____ (Writer's signature)
Faculty supervisor: Nestor Cardozo Charlotte Botter External supervisor(s):	
Title of thesis: Seismic imaging of salt-influenced extensional forced folding	
Credits (ECTS): 30	
Keywords: Salt-influenced extensional forced fold Faults Geomechanical modeling Finite Strain Seismic imaging	Pages: 93 +enclosure: CD Stavanger, June 15th, 2016

Seismic imaging of salt-influenced extensional forced folding

by

Rosita Maryam Haftbaradaran

Master Thesis

Presented to the Faculty of Science and Technology

The University of Stavanger

The University of Stavanger

06-2016

Acknowledgements

Abstract

Seismic imaging of salt-influenced extensional forced folding

Rosita Maryam Haftbaradaran
The University of Stavanger, 2016

Supervisors: Nestor Cardozo
              Charlotte Botter

Extensional forced folds are formed by the presence of a ductile salt layer, decoupling the overlying folded strata from the underlying faulted strata. Hydrocarbons are generally trapped within secondary structures of forced folds. The objective of this thesis is to analyze the impact of salt-influenced extensional forced folding and seismic parameters on the resultant seismic image. Fine-tuning the seismic parameters of illumination direction and wave frequency can help to better understand and potentially improve seismic imaging of salt-influenced extensional forced folding and secondary faults. To achieve this objective, a synthetic workflow is carried out in 2D, consisting of: i. mechanical modeling of salt-influenced extensional forced folding; ii. computation of finite strain in the mechanical model; iii. modification of the initial acoustic properties of the model based on finite strain; iv. seismic imaging using pre-stack depth migration (PSDM). This workflow is applied to three models; model 1 includes siliciclastic sediments, model 2 includes a salt layer below the siliciclastic sediments, and model 3 includes salt, siliciclastic sediments and growth strata. All the simulations produce realistic but different geometries and strain fields, with model 1 resembling a graben, localized above the major fault zone, model 2 displaying a forced fold with a wide distribution of associated secondary faulting, and model 3 displaying a steeper forced fold, and a wider distribution of secondary faulting. Seismic images of these models include different illumination directions (specular, left side and right side) and wave frequencies (10, 20, 30 and 40 Hz). Specular illumination highlights the flat reflectors outside the fault zone, also highlighting fault related diffractions. Offside illuminations target the dipping reflectors, where the left side illumination highlights the antithetic faults and right side illumination highlights the forelimb of the forced fold and synthetic faults. At a high frequency (30 Hz), the seismic images are more defined, creating better characterization of forced folding and secondary faulting. The evaluation of the combination of seismic parameters (i.e. illumination direction and wave frequency) is to generate a better seismic characterization salt-influenced extensional forced folds and faults.

Table of Contents

List of Tables

List of Figures

1 Introduction

Extensional forced folds are formed due to normal fault movement of a competent rock unit (e.g. basement) below a less competent sedimentary cover. The forced folds are typically monoclines with a steep limb and two relatively flat limbs (Figure 1). Salt is primarily composed of halite (NaCl) and has a low permeability, providing a good seal for the preservation of hydrocarbon accumulation (Massimi et al., 2007). The presence of a ductile unit like salt facilitates the development of extensional forced folds by decoupling the overlying folded strata from the underlying faulted strata (Figure 1; Withjack and Callaway, 2000). Extensional forced folds and its associated faults may significantly influence the migration of fluids, such as oil (Cosgrove and Ameen, 1999). Hydrocarbons are generally trapped within secondary structures, associated with extensional forced folding, such as the anticlinal area, and the faulted and tilted sedimentary strata (Saltzer and Pollard, 1992) (Figure 1). Examples of systems associated with salt-influenced extensional forced folds are the Haltenbanken area, offshore Norway (Withjack et al., 1989), Upper Rhine Graben, Central Europe (Maurin and Niviere, 1999), Gulf of Suez rift basin, Egypt (Jackson et al., 2006), and Basque-Cantabrian Basin, Northern Spain (Tavani and Granado, 2015).
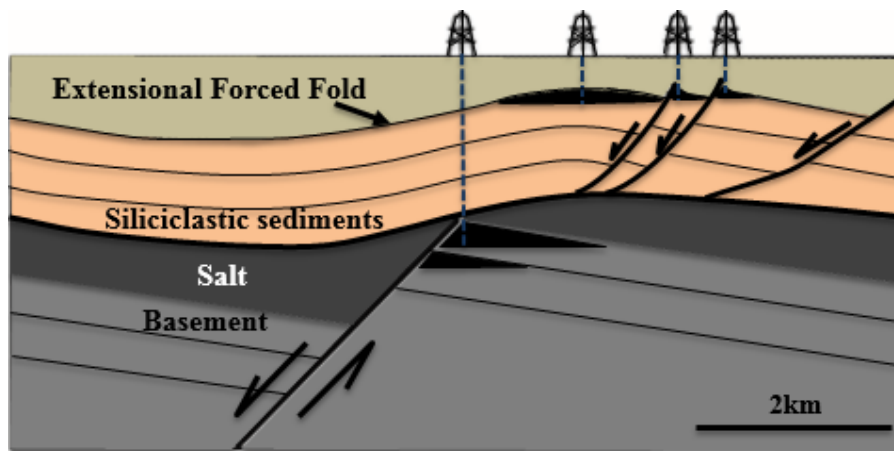
Figure 1: Illustration of extensional forced fold above major normal fault. Dark grey represents a ductile salt layer. Orange represents brittle siliciclastic sediments. Black represents hydrocarbons. Modified from Withjack and Callaway (2000).

Analogue models provide important insight into the deformation of extensional forced folds (e.g. Vendeville et al., 1995; Withjack and Callaway, 2000; Finch et al., 2004). In an extensional setting, salt can facilitate the development of forced folding and a wider

distribution of deformation. Figure 2 shows two analogue models illustrating the influence of salt in extensional forced folding. The salt layer is represented by silicone putty and the basement is represented by a metal base (Withjack and Callaway, 2000). The pre-kinematic sequence consists of sand added before deformation. The syn-kinematic sequence consists of sand added during deformation. Model A does not have salt, and model B has a salt layer between the basement and the sedimentary cover. In Model A, a graben forms directly above the major normal fault and no monocline develops in the cover sequence. In Model B, flow of the salt layer causes a broad monocline (extensional forced fold) in the cover sequence. The decoupling of the basement and brittle overburden due to the viscous salt layer, causes the deformation to propagate from the basement to the overburden as a broad forced fold. In Model B, a detached graben forms in the hanging wall, approximately more than 15cm from the major normal fault, indicating that faulting in the cover is not linked to the underlying basement fault.
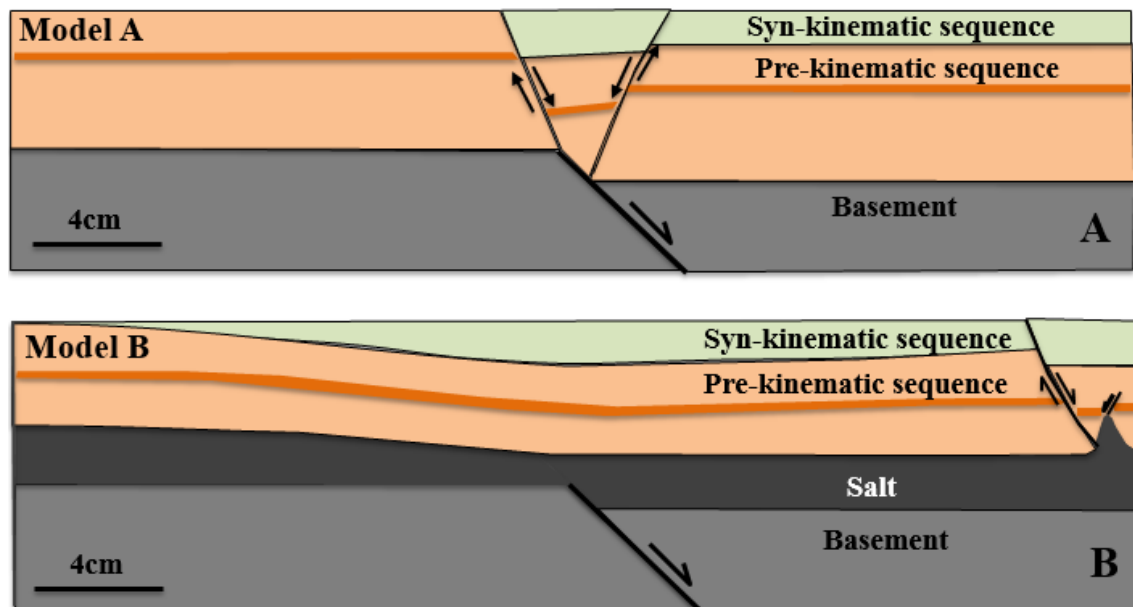
Figure 2: Analogue Models: (A) Model without salt; (B) Model with a salt layer resulting in a broad forced fold (monocline). Modified from Withjack and Callaway (2000).

The geometry and distribution of extensional forced folds and associated secondary faults are dependent on several variables, such as the rate of fault displacement, displacement rate of salt, salt thickness, overburden thickness, and properties of the ductile salt layer (e.g. viscosity and density) (Withjack and Callaway, 2000). Major fault displacement increase, increase in salt displacement rate and thickness, decrease in overburden thickness, and

decrease in viscosity of the ductile salt layer can contribute to more decoupling of overlying folded strata from the underlying faulted strata, therefore resulting in more distributed forced fold deformation. The impact of these variables indicates the complexity of the geometry and distribution of forced folds.

Outcrop evidence of extensional forced folds is rare (Maurin and Nieviere, 1999) because these folds are often associated to large-scale faults that are rarely completely exposed. There are some exceptions however (e.g. Hadahid monocline in Western Sinai, Egypt; Whipp, 2011). Seismic data can show large-scale normal faults and extensional forced folds (Figure 3). However, seismic imaging of extensional forced folds is challenging as these folds have steep limbs that often are steeper with depth (Withjack and Callaway, 2000). Seismic imaging of salt-influenced extensional forced folding, is particularly challenging because salt is mechanically weak, hence it flows easily creating complex structures. Additionally, there are large velocity contrasts between the high-velocity salt and the surrounding lower-velocity sediments (Raymer et al., 2000). These contrasts in mechanical and elastic properties between the salt and its surrounding strata can potentially obscure or distort the seismic image (Withjack and Callaway, 2000).

Seismic imaging of certain structures is challenging, therefore the analysis of the seismic response to different seismic acquisitions and seismic parameters is important. Figure 3 shows an example of a seismic image and interpretation of a salt-influenced extensional forced fold of the Stavanger Fault System (SFS) (Figures 3A and 3B) and Sele High Fault System (SHFS) (Figures 3C and 3D), offshore Norway. Figure 3 illustrates the influence of salt in inhibiting fault propagation and decoupling the deformation in the cover above. Figures 3B and 3D illustrate a forced fold forming above the SFS and SHFS normal faults. Similarly, to the analogue model (Figure 2), in both fault systems, strata above the weak salt unit were subjected to forced folding and brittle faulting (Figure 3). Figures 3A and 3C show that salt is challenging to characterize on seismic. They also illustrate that the high dip angles of the faults and steeply dipping limbs of the forced folds are challenging to interpret in the seismic images. Steeply dipping structures such as high-angle faults and steeply dipping limbs of forced folds are poorly imaged in seismic by conventional seismic surveys, due to the reflected sound waves that return to the surface at a high angle, hence are not picked up by the recording array (Nichols, 2009).
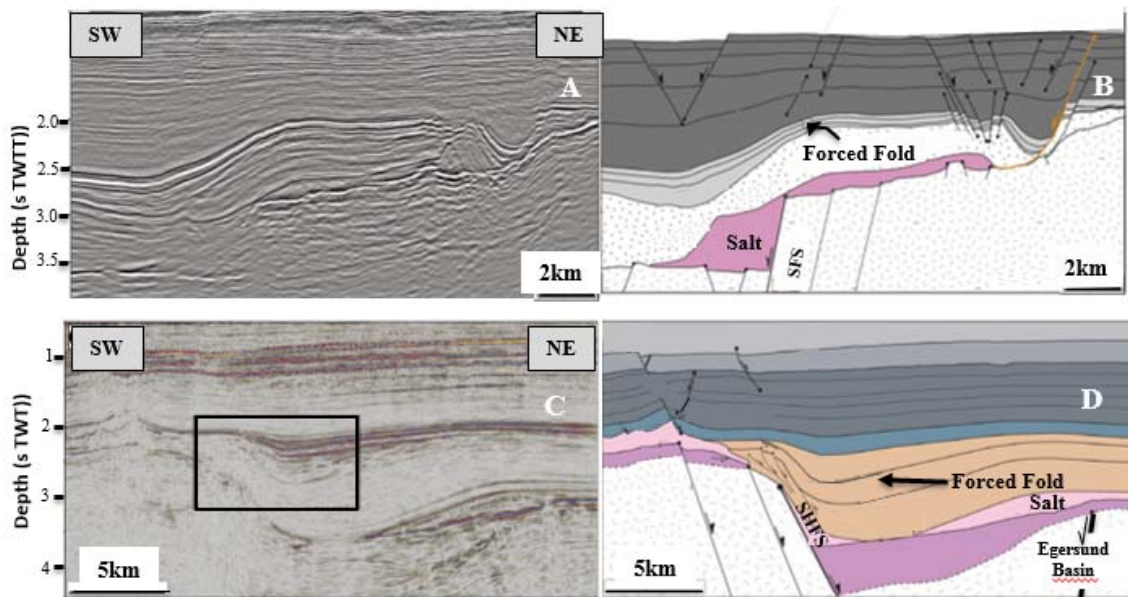
Figure 3: (A) and (C) Seismic, (B) and (D) Seismic interpretation of forced folding with presence of salt (Lewis et al., 2013 – (A) and (B)) (Jackson et al., 2014 – (C) and (D))

The improvement of seismic imaging of salt-influenced structures is of interest to the exploration industry as hydrocarbon traps are often associated with salt and extensional forced folding. Some studies have focused on seismic imaging of fault zones and salt-related deformation. Botter et al (2014) studied fault and fault damage characterisation on seismic images through a synthetic workflow in siliciclastic sequences by modifying seismic parameters and resolution. Ratcliff et al (1992) discussed seismic imaging of salt structures in the Gulf of Mexico, focusing on the recognition, preservation and migration of salt signals, with the use of different acquisition techniques. Jones and Davidson (2014) focused on seismic imaging of salt bodies, reviewing seismic acquisition and processing, leading to improvements on image quality.

The objective of this thesis is to analyze the impact of salt-influenced extensional forced folding and seismic parameters on the resultant seismic image. Given the challenges of imaging salt-influenced structures, it is questionable whether it is possible to interpret these structures from seismic data correctly. Therefore, fine tuning seismic parameters, such as illumination direction and wave frequency, can help to evaluate their impact on seismic to better understand and potentially improve seismic imaging of salt-influenced extensional forced folds and its associated secondary faults.

To achieve the objective of this thesis, a synthetic workflow similar to that of Botter et al. (2014) is carried out in 2D. This forward modeling workflow consists of i. mechanical modeling of salt-influenced extensional forced folds; ii. computation of finite strain in the mechanical model; iii. modification of the initial acoustic properties of the model based on finite strain, and iv. seismic imaging. This workflow is applied to three 2D kilometer-scale models; model 1 includes only siliciclastic sediments, model 2 includes a layer of salt below the siliciclastic sediments, and model 3 includes salt, siliciclastic sediments and growth strata. Different seismic parameters, such as illumination directions and wave frequencies are applied to these models. The main result of this work is to analyze which seismic parameters applied to the models improve the resultant seismic image of these geological structures. This work can contribute to better seismic acquisition, processing, and interpretation of salt-influenced extensional forced folds.

2 Methodology

The workflow follows the methodology of Botter et al (2014) to model seismic images of extensional forced folds with the influence of a ductile salt layer and growth strata, to study the structural evolution, and to evaluate the seismic acquisition and processing parameters for seismic imaging and interpretation. This methodology is used to generate a seismic image from a known structure; in this case the structure is a model of an extensional setting. Applying forward modeling is a good approach to improve extensional forced folding and associated faulting characterisation. Figure 4 illustrates the steps of this forward modeling workflow (Botter et al., 2014): 1. mechanical modeling of salt-influenced extensional forced folding using a 2D discrete element method (DEM) (Hardy et al., 2009), 2. computation of finite strain in the mechanical model using SSPX software (Cardozo and Allmendinger, 2009), 3. modification of the initial acoustic properties of the model based on finite strain (Botter et al., 2014), and 4. seismic imaging using pre-stack depth migration (PSDM) simulator (Lecomte, 2008). To investigate the influence of a salt layer and growth strata on the geomechanical evolution and seismic imaging, the workflow is applied to three 2D kilometer-scale models; model 1 includes only siliciclastic sediments, model 2 includes a layer of salt below the siliciclastic sediments, and model 3 includes salt, siliciclastic sediments and growth strata.

Figure 4: Methodology: From mechanical model (DEM) to seismic image. Workflow from Botter et al (2014).

2.1 Discrete element method (DEM) mechanical modeling

A two-dimensional discrete element method (DEM) is used to simulate the evolution of three models in an extensional setting. The discrete element method (DEM) as introduced by Cundall and Strack (1979) has evolved as an important method for modeling particle systems by tracking each particle's movement and its interaction through its evolution (Kruggel-Emden et al., 2007). The DEM is a discontinuum method (Cundall and Strack, 1979) that tracks the interactions of rigid particles under applied forces or displacement boundary conditions (Gray et al., 2014). These particles obey Newton's equations of motion (Hardy et al., 2009). This allows the observation of the dynamic evolution of a system. Hence, the

DEM provides easy accessibility to the monitoring of displacement and location of particles through time (Vidal-Royo et al., 2011). Therefore displacement and kinematic evolution of the system can be easily followed at any stage of the model (Vidal-Royo et al., 2011). Mechanical modeling has become increasingly popular in the study of different geological settings, as it can provide significant insights into evolution and geometries of complex geological features (Gary et al., 2014). Many previous studies have used the DEM and have produced realistic fault geometries of: normal faulting in layered sequences (Egholm et al., 2008), detachment folding (Hardy and Finch, 2005), fault propagation folding (Cardozo et al., 2005; Hardy and Finch, 2006), and fold and thrust belts (Strayer and Suppe, 2002). Hence, DEM is a suitable method to study the evolution of fault formation, from initiation to propagation, resulting in potential folding and faulting in a realistic manner.

In this thesis, the DEM is used to produce a realistic evolution of fault, salt-related structural geometry in an extensional setting. The 2D DEM code used in this thesis is called cdem2D and it was developed by Stuart Hardy (ICREA, University of Barcelona). The DEM model of the cdem2D code consists of 24 layers; layers 1 to 12 are defined as salt and layers 13 to 24 are defined as siliciclastic sediments. The DEM is composed of a ductile-brittle assemblage of circular rigid particles, which represent siliciclastic sediments, salt, and growth strata, which obey Newton's equations of motion and interact with viscous (salt) and frictional (siliciclastic sediments) forces under gravity (Hardy et al., 2009). The circular particles undergo motion relative to one another. The particle properties are shown in table 1. The siliciclastic sediments are modeled as homogeneous, purely frictional materials, and the salt as a viscous material. In a kilometer-size simulation, the particles are meter-size in scale and have a given density. Although, this indicates that the particles do not represent rock grains, this method is able to generate a realistic geometry of the extensional setting. Figure 4 shows the 2D particle assemblage before and after deformation. In addition, the DEM provides sequential changes to the model, from the addition of growth strata. The influence of the ductile salt and growth strata are evaluated on the evolution of the siliciclastic assemblage, to observe the resulting changes from these variables. A displacement boundary condition is applied at the base of the model to simulate normal faulting. An advantage of DEM is the development of strain localization and shear zone formation in granular materials, as this method is meshless, no re-meshing is required when large deformations accumulate, and geometry and strain are handled in a natural manner (Egholm, 2007). The three models will

7

be observed, compared and contrasted in terms of its kinematic evolution and strain distribution.

	Minimum element radius (m)	Maximum element radius (m)	Average element radius (m)	Density of particles (kg/m^3)	Particle stiffness (GPa)	Particle friction	Viscosity constant (N . S . m^{-1})
Siliciclastic sediments	6.250	15.625	9.711	2500	5.6	0.35	-
Salt	6.250	15.625	9.711	2100	-	-	3.0E+07

Table 1: Particle properties in siliciclastic and salt type materials.
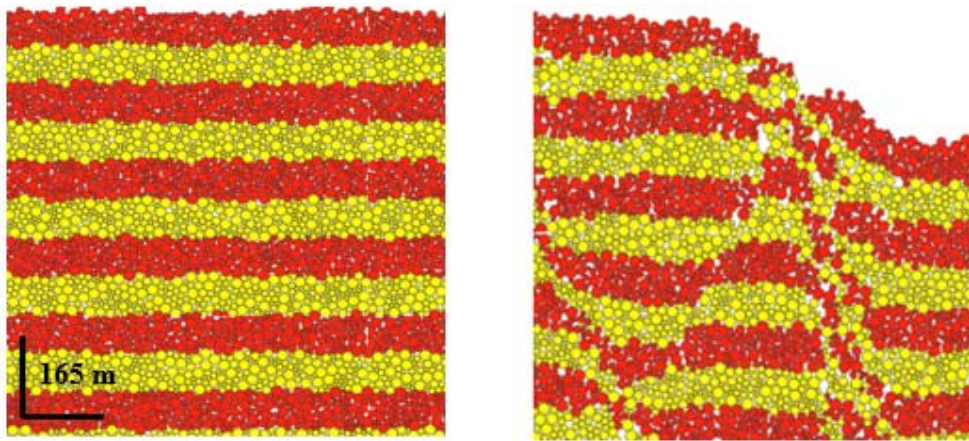
Figure 5: 2D particle assemblage before (left) and after (right) deformation of siliciclastic sediments.

2.2 Finite strain computation

Finite strain computation of the DEM model is carried out using the program SSPX. The SSPX program implemented by Cardozo and Allmendinger (2009) can be used to interpret the strain from the particle displacements of the DEM. Strain allows the visualization of a deformed material and provides ways to determine where and when the material has been deformed (Cardozo and Allmendinger, 2009). SSPX facilitates the computation of strain from displacement data in 2D. The DEM simulation records at any stage the incremental and total particle displacement values. These particle displacement values can be used to compute incremental or total strains (Cardozo and Allmendinger, 2009). The SSPX program is used to compute total, finite strain using the nearest-neighbor routine (Cardozo and Allmendinger, 2009). This involves the DEM model being divided into regular cells; at the center of each cell, finite strain is computed from the displacement of particles within a user-defined radius. The heterogeneous strain in the fault volume is thus converted into a cell-based strain

(Cardozo and Allmendinger, 2009). Figure 6 shows the application of the SSPX software to the 2D DEM model. Figure 6 shows the results of the finite strain computation of the DEM; figure 6A shows maximum shear strain and figure 6B shows volumetric strain.
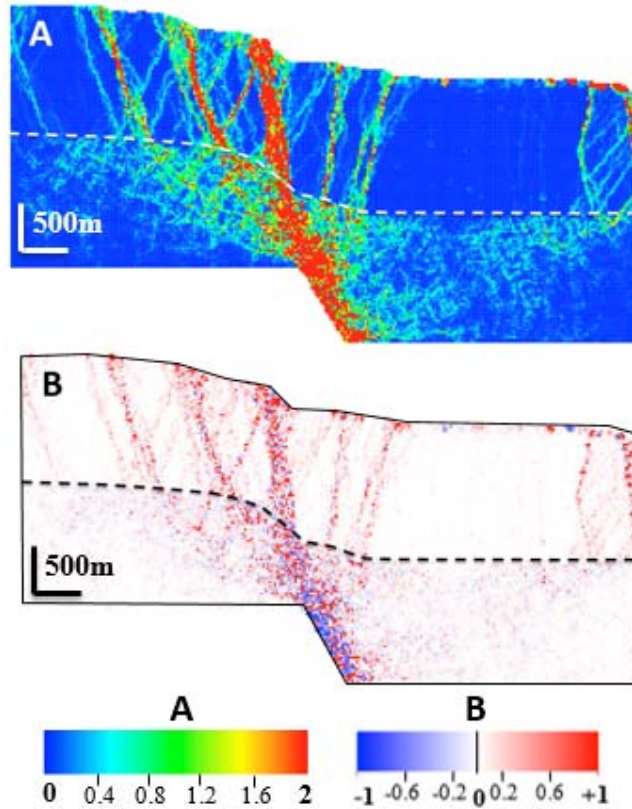
Figure 6: Maximum shear strain (A) and volumetric strain (B). Dashed lines indicate the boundary between salt (located below) and siliciclastic sediments (located above).

2.3 Modify seismic properties due to finite strain

Density and seismic velocity values are assigned to the rock materials before faulting. These values are averages taken from the literature (Table 2; Mavko et al., 2009). Table 2 shows that density is lower in salt in comparison to siliciclastic sediments. Seismic velocities in salt are generally higher in comparison to siliciclastic sediments (Table 2). The siliciclastic sediments are homogeneous in the DEM model, however, for the purpose of seismic imaging, the siliciclastic sediments are considered to be layers of sandstone and shale, which are assigned different densities and seismic velocities, to obtain a change in reflectivity and seismic reflections between these layers.

9

The seismic properties shown in table 2 are modified due to fault related finite strain. As we are dealing with large deformations, elastic linear stress-strain relations are not applicable. Instead, in this thesis, very simple empirically based relationships between porosity and seismic velocities and volumetric strain are used. These relationships are taken from Botter et al. (2014). Equations 1-4 allow the computation of the change of seismic properties (density, P-wave velocity and S-wave velocity) due to finite volumetric strains. Initial porosity values are modified according to a linear relation between porosity and volumetric strain (Figure 7; Botter et al., 2014). The modified porosity (ϕ) is used to compute the new density (ρ). P-wave seismic velocity is assumed to follow a sigmoidal relation with respect to volumetric strain (Figure 7; Botter et al., 2014). S-wave velocity (Vs) is computed from P-wave velocity (Vs) using Han's relation. In model 3 growth strata is present. These strata are unconsolidated and therefore their velocities are assumed to be 75% of the velocity values of the pre-growth sandstone and shale (table 2). Dilation increases porosity, thereby decreasing density and seismic velocities. Inversely, compaction decreases porosity, thereby increasing density and seismic velocities (Figure 7; Botter et al., 2014). However, salt does not follow these relationships. Salt is ductile and their properties don't vary significantly in comparison to the siliciclastic sediments. Therefore, the relations of Figure 7 are only applied to the brittle siliciclastic sediments. The properties of the salt remain the same. The estimated property changes may not be completely accurate, however, they are still within reasonable ranges, thereby being a reasonable approach to evaluate the impact of forced folding and faulting on seismic data. Also, relative changes of seismic properties are more important for seismic imaging than absolute values (Botter et al., 2014).

$$\phi = \phi_{ini}(0.25\varepsilon_v + 1), \quad -1 \leq \varepsilon_v \leq 1 \qquad (1)$$

$$\rho = \rho_g(1 - \phi) + \rho_w\phi \qquad (2)$$

$$\rho_g = \text{grain density}, \quad \rho_w = \text{fluid density}$$

$$Vp = \begin{cases} Vp_{ini}(-0.25\varepsilon v - 0.5\varepsilon v\text{^}2 + 1), & -1 \leq \varepsilon v < 0 \text{ (compaction)} \\ Vp_{ini}(0.25\varepsilon v - 0.5\varepsilon v\text{^}2 + 1), & 0 \leq \varepsilon v \leq 1 \text{ (dilation)} \end{cases} \qquad (3)$$

$$Vp_{ini} = \text{initial P-wave velocity}$$

$$Vs = 0.794Vp - 0.787 \qquad (4)$$

	Density (g/cm³)	P-wave velocity (Vp) (km/s)	S-wave velocity (Vs) (km/s)
Salt	2.16	4.50 – 4.55	2.59 – 2.63
Sandstone	2.65	4	2.389
Shale	2.65	2	0.801

Table 2: Initial properties values for salt and siliciclastic sediments (sandstone/shale) (Mavko et al., 2009).
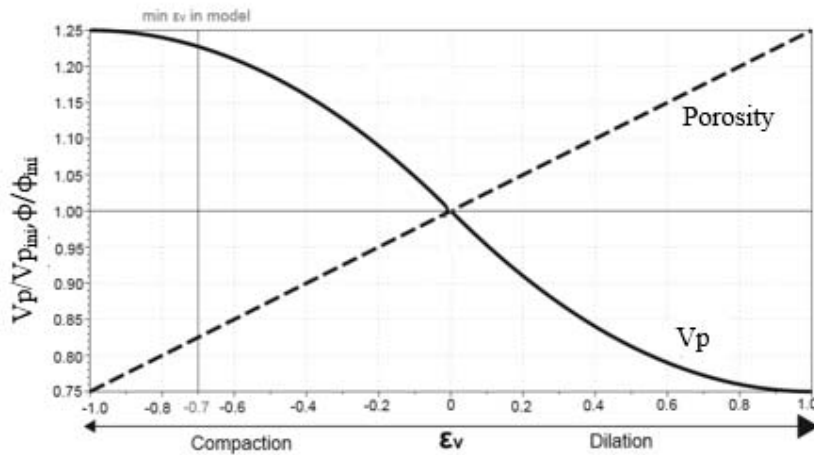
Figure 7: Empirical relationships between P-wave velocity (Vp) and volumetric strain (εv) and between porosity (ϕ) and volumetric strain (εv). From Botter et al. (2014).

2.4 Seismic Imaging; Pre-stack depth migration (PSDM) simulation

The seismic imaging simulator is used to evaluate the impact of the salt-influenced structures and properties on the resultant seismic image. The technique used is a pre-stack depth migration (PSDM) simulator (Lecomte, 2008). The PSDM simulator is in the pre-stack domain and seismic images are in depth. The PSDM simulator is a fast and robust FFT-based imaging approach (Lecomte and Pochon-Guerin, 2005). The software running the PSDM simulator is SeisRoX by NORSAR. The inputs to create the seismic image are the density and seismic velocities after faulting. The PSDM seismic response of a model takes into account survey geometry and overburden structures. The PSDM simulator acts as an image-processing method by distorting the input reflectivity to reproduce the effects on seismic imaging (Lecomte, 2008).

The input of the PSDM simulator is the input reflectivity, which is obtained from the modified seismic properties (i.e. density and seismic velocities) from the DEM model after faulting (Figure 8a). This input reflectivity is converted into the wavenumber domain using a Fast Fourier Transform (FFT) (Figure 8a). Using ray-based methods, illumination vectors are applied to the considered point as a combination of the incident and scattered rays (Botter et al., 2014). The illumination vectors are selected according to the angle intervals chosen by the interpreter. A PSDM filter is generated in the wavenumber domain, from ray methods, which are dependent on survey, frequency content, wave type, and velocity model (Figure 8b) (Botter et al., 2014). PSDM filters for two types of illumination directions are generated: specular and offside illuminations. Figure 8c, d and e shows the corresponding PSDM filters for the different illumination directions. Figure 8c shows the PSDM filter corresponding to a complete survey, to generate specular illumination. The illumination direction allows the option of choosing a specific part of the seismic to image. Figures 8d and 8e show the PSDM filter corresponding to a sub-selection of the survey. Illuminating the left and right side of the seismic image, respectively, generates an offside illumination.

An inverse Fast Fourier Transform (FFT-1) is applied to the PSDM filter in the wave number domain, to produce the point spread function (PSF) in the spatial domain (Lecomte et al, 2015). PSF is an image response of a point scatterer at the reference point (Lecomte, 2008). The PSF response indicates the proficiency of the PSDM simulator, providing vertical and lateral resolution, angle and direction of the reflectors, which are indicated on the resultant PSDM seismic images. Geological structures that are not comprised within the PSF range, such as high-angle faults or steep limbs of folds, will not be visible on seismic, causing difficulty to interpret these features. Therefore, changing the illumination direction can help to highlight features that would typically not be visible in seismic. The application of the PSDM filters on the input reflectivity, plus the inverse FFT on the result of this operation produces the PSDM seismic images (Botter et al., 2014).

The PSDM simulator allows parameters such as illumination direction and wave frequency to be fine-tuned to evaluate their impact on the seismic image, to better understand seismic imaging of salt-influenced faulting and extensional forced folding in the brittle siliciclastic sediments. The illumination direction allows the option of choosing a specific part of the seismic to image, therefore impacting the total fault volume illuminated in the seismic image

(Botter et al., 2014). Wave frequency controls the resolution of the fault in the resulting seismic image. The DEM model involves many increments of deformation. Therefore, different evolutionary stages in the model can be selected to seismic image. This can provide an understanding of the impact of deformation on the seismic image.
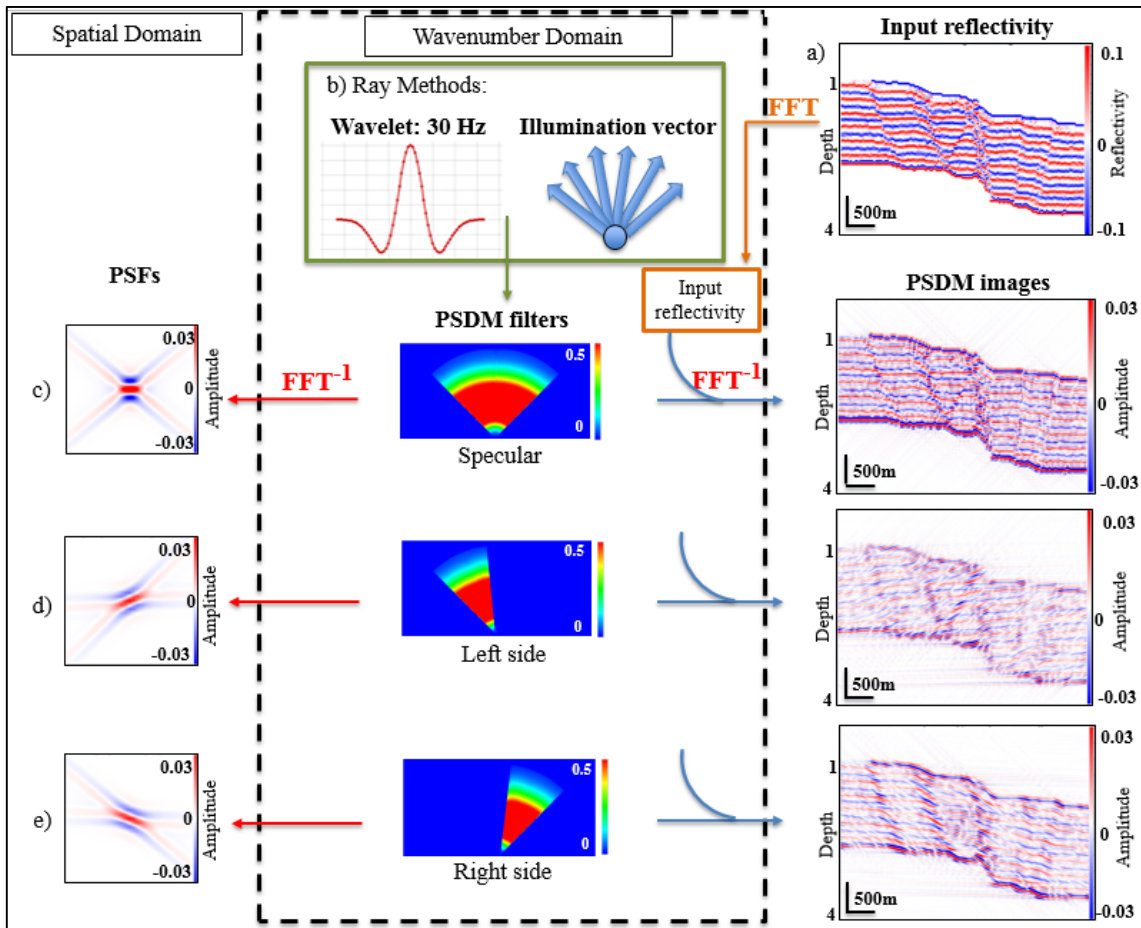
Figure 8: Illustration of the PSDM simulator. (a) Reflectivity grid in the spatial domain. (b) Ray methods used to calculate PSDM filters in the wavenumber domain. Wave frequency of 30 Hz is used in this illustration. Types of illumination directions: (c) specular, (d) left side and (e) right side. More details are explained in the text.

3 Results

3.1 Mechanical Modeling

Three 2D DEM models are considered: Model 1 includes only siliciclastic sediments, model 2 includes salt and siliciclastic sediments, and model 3 includes salt, siliciclastic sediments and growth strata. All models have a displacement boundary condition at the center of the base, corresponding to a 60° dipping normal fault. The siliciclastic sequence has the same mechanical properties (purely frictional), and the salt has viscous behaviour. Layers in the siliciclastic sequence and the salt are passive and help to visualize the resultant structures. All three models have an initial width of 6.25 kilometers (km) and height of 2.80 km (Figure 9). Each increment of the model is 1 meter (m) of fault displacement. The total fault displacement of the models is 1 km (1000 increments), corresponding to a total horizontal extension of 500 m.
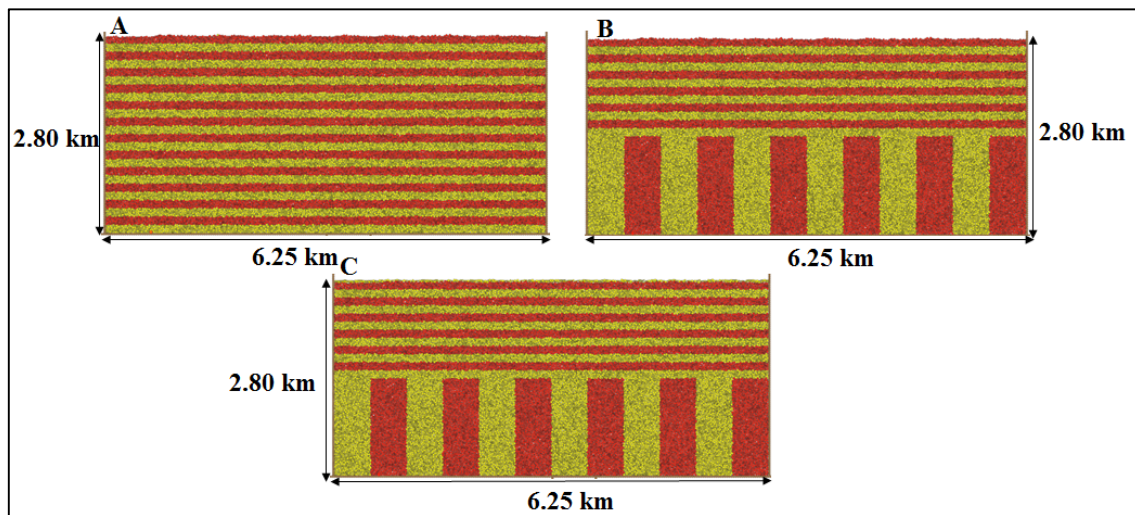
Figure 9: Initial configuration of models 1, 2 and 3; initial width of 6.25 km and height of 2.80 km. (A) model 1; (B) model 2; (C) model 3. Horizontal layers are siliciclastic sediments and vertical layers are salt.

The models provide important insight into the evolution of salt-influenced extensional forced folds and their associated secondary faulting. The models provide comparison on how the salt layer and syn-kinematic sedimentation (growth strata) influence the evolution of the extensional forced fold. Figures 10, 11 and 12 show the interpretation of models 1, 2 and 3 at the end of the simulation after 1 km fault displacement. Letters indicate faults as described in the text.

14

a.
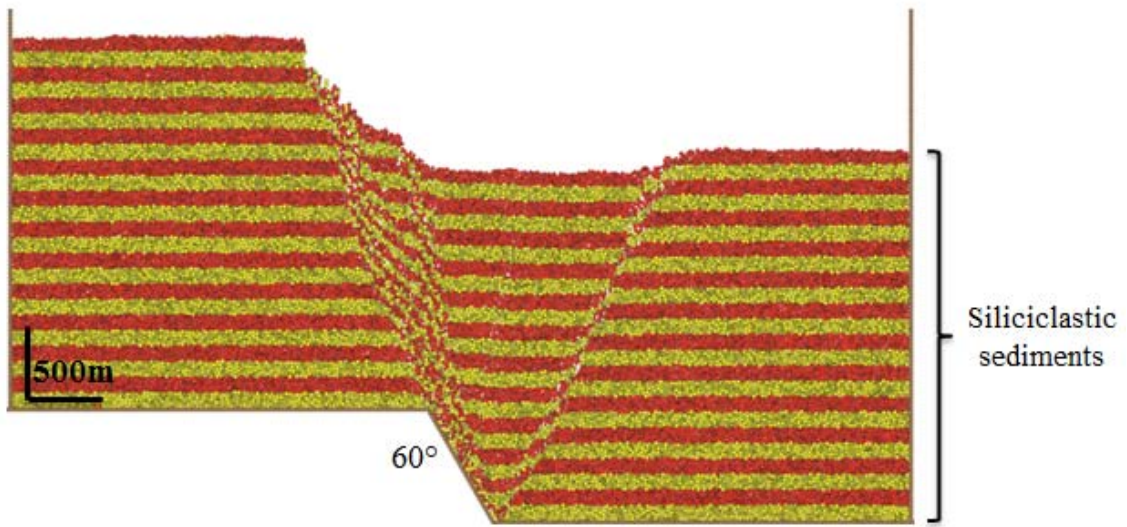
b.
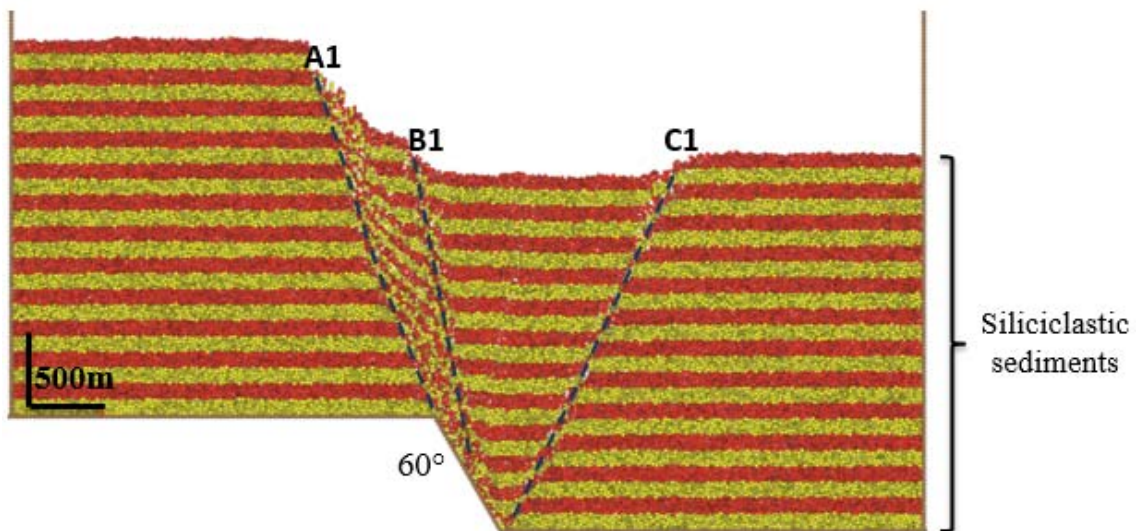
Figure 10: a. DEM Model 1 at 1 km fault displacement. b. Interpretation of the model.

a.

b.
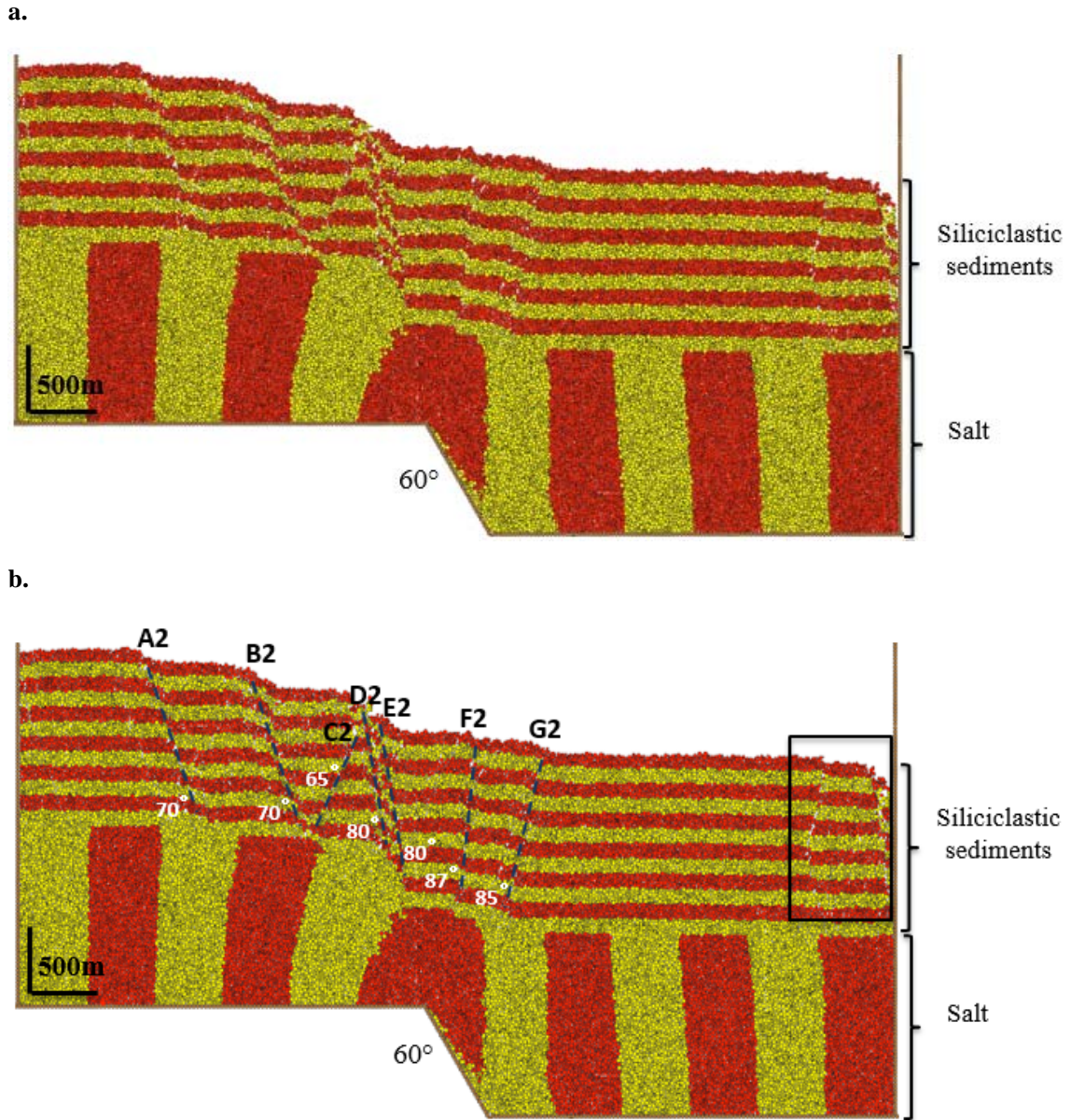
Figure 11: a. DEM Model 2 at 1 km fault displacement. b. Interpretation of the model. The rectangle highlights a collapse area located at the right side-wall of the model.

a.

b.
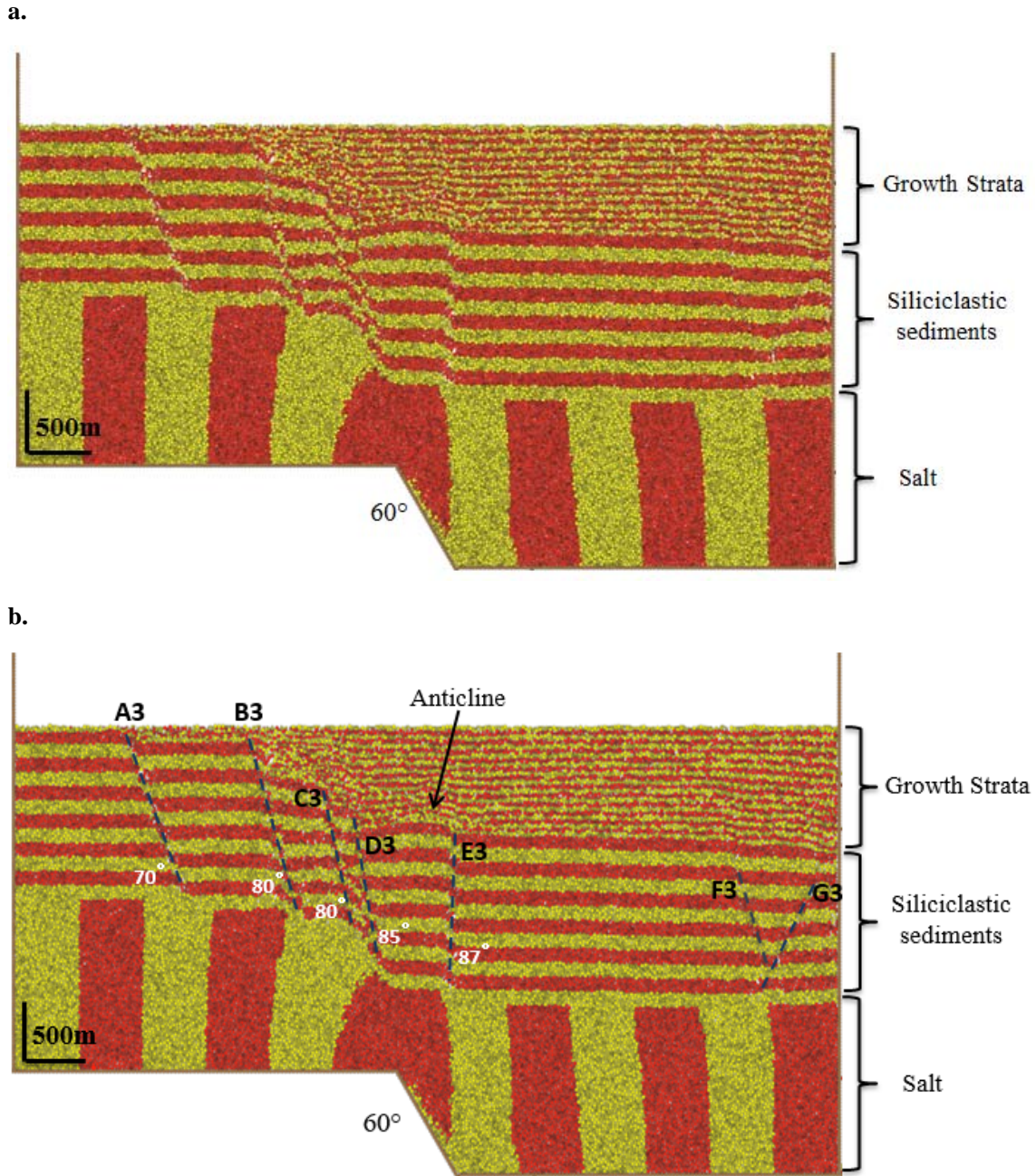
Figure 12: a. DEM Model 3 at 1 km fault displacement. b. Interpretation of the model.

3.1.1 Evolution of geometry and strain

Figures 13, 14, and 15 show the evolution of the models 1, 2 and 3, respectively; geometry (left), shear strain (centre) and volumetric strain (right) at four stages corresponding to fault displacements of: 200, 500, 800, and 1000 m.

3.1.1.1 Model 1: Siliciclastic sediments

Model 1 consists of siliciclastic sediments, with the absence of salt. At 200 m major fault displacement, a synthetic fault (fault B1) propagates towards the footwall developing a monocline. As model 1 evolves, the monocline is breached, where minor synthetic faults contribute to the collapse of the monocline (Figure 13b). At ≈ 300 m major fault displacement, an antithetic fault (fault C1) dipping 55-60˚ is developed in the hanging wall. At 500 m displacement, a normal fault scarp has developed, evidently dividing the hanging wall and footwall of the model (Figure 13b). The mechanical geometry, shear strain and volumetric strain show secondary normal faults linking with the major normal fault, which is similar to the sandbox model by Withjack and Callaway (2000). The synthetic faults (faults A1 and B1) are steep: 80˚ to 85˚ fault dip. The secondary faults are localized above the major normal fault and have high shear and volumetric strain.

Model 1 produces a depression resembling a graben structure. The evolution of model 1 shows the breach of the monoclinal fold, and continued displacement of the major fault, resulting in footwall uplift and subsidence of the hanging wall. This is similar to Withjack and Callaway (2000), where in a sandbox model with the absence of a salt layer, a monocline did not develop in the cover sequence, but instead a graben formed directly above the major fault zone (Figure 2A).

3.1.1.2 Model 2: Siliciclastic sediments and salt

An extensional forced fold is formed by the presence of the ductile salt layer, decoupling the overlying folded strata from the underlying salt layer (Withjack and Callaway, 2000). At 200 m major fault displacement, a broad monoclinal forced fold is visible (Figure 14a). A steep reverse fault propagating towards the hanging wall is the earliest fault to develop at $\approx$ 150 m displacement. Reverse faults are consistently the first structures to develop (Hardy, 2011). At 200 m fault displacement, a normal fault (fault E2) is located below the reverse fault (Figure 14a). This normal fault propagates upwards eventually replacing the reverse fault at $\approx$ 450 m major fault displacement. Therefore this early reverse fault does not appear to be reactivated at later stages of the model. This is also confirmed in a normal fault model consisting of homogeneous frictional particles by Hardy (2011).

Faults D2 and A2 develop at $\approx$ 300 m and $\approx$ 350 m fault displacement, respectively. Fault F2, develops at $\approx$ 400 m fault displacement and fault B2 at $\approx$ 450 m fault displacement. Faults A2 and B2, are synthetic faults located in the footwall. Fault G2 develops at $\approx$ 500 m fault displacement. An antithetic fault (fault C2) starts to develop at $\approx$ 850 m fault displacement (Figure 14d). Two reverse faults (faults F2 and G2) are located in the hanging wall. A similar deformation pattern has been reported in the Gulf of Suez (Sharp et al., 2000; Jackson et al., 2006). The highest shear strain and volumetric strain are localized directly above the major fault tip (Figure 14). As model 2 evolves, the forelimb of the forced fold steepens, due to the influence of the salt layer and increase in major fault displacement, hence increasing displacement of associated secondary faulting in the cover sequence.

Shear strain illustrates salt migration; as fault displacement increases, salt migrates farther away from the major fault footwall and towards the hanging wall. The initial thickness of the salt was $\approx$ 1400 m and throughout evolution; the thickness of the salt near the footwall and hanging wall of the major fault are < 900 m and 1500 m, respectively. Therefore the thickness of the salt layer changes, as it thins near the footwall of the major fault and thickens near its hanging wall (Withjack and Callaway, 2000).

3.1.1.3 Model 3: Siliciclastic sediments, salt and growth strata

Growth strata are added throughout the evolution of the model, to simulate deposition during deformation. The rate of sedimentation is larger than the rate of uplift resulting in the growth strata covering the structure, with evidence of thinning and onlapping towards the structural highs (i.e. footwall) (Figure 15). Similarly to model 2, a steep reverse fault is the earliest fault to develop at ≈ 200 m major fault displacement. As the mechanical model evolves, this reverse fault is replaced by a younger normal fault at ≈ 400 m major fault displacement. Therefore the early reverse fault does not appear to be reactivated later in the model. Fault B3 starts to develop at ≈ 250 m major fault displacement, along with fault C3 at ≈ 300 m major fault displacement, and faults A3 and E3 at ≈ 400 m major fault displacement. In the cover sequence, the secondary faults are synthetic normal faults, apart from fault E3, which is a reverse fault and fault G3 which is an antithetic fault. Shear and volumetric strain are highest at faults C3 and D3 in comparison to the other secondary faults, as they are located almost directly above the major fault (Figure 15). The lowest shear and volumetric strains are faults F3 and G3, as these faults are located furthest from the major fault zone (Figure 15c-d).

The syn-kinematic sequence (growth strata) influences the deformation within the pre-kinematic sequence (siliciclastic sequence). Figure 15b shows the geometry of model 3 at 800 m major fault displacement. An anticline develops in the growth strata, thereby influencing the pre-kinematic siliciclastic sequence. The additional load from the growth strata causes a steeper forelimb of the forced fold (Figure 15). This is illustrated by the steeper dip angles of the secondary faults in the cover sequence (Figure 12). The widespread distribution of growth strata induces deformation in more areas of the model, hence, faults F3 and G3 formed in the hanging wall on the right side of the model, superficially resembling a graben structure. The location of faults F3 and G3 is controlled by the model boundary conditions; if model 3 had been wider, these faults could potentially have formed farther from the major normal fault (Withjack and Callaway, 2000). In an experimental model by Withjack and Callaway (2000), a detached graben formed in the hanging wall near the boundary of the model (Figure 2B) similarly to model 3.

The evolution of forced folding and secondary faulting commonly leads to salt migration resulting in variations in strain (Kane et al., 2010). The changes in salt thickness are relatively unaffected by the growth strata. Similarly to model 2, in model 3 the salt layer thins near the footwall and thickens near the hanging wall (Withjack and Callaway, 2000).

20

Figure 13: Model 1 at (a) 200, (b) 500, (c) 800, and (d) 1000 m major fault displacement. Left column is geometry, middle column is shear strain, and right column is volumetric strain (red = dilation, blue = compaction).

21

Figure 14: Model 2 at (a) 200, (b) 500, (c) 800, and (d) 1000 m major fault displacement. Left column is geometry, middle column is shear strain, and right column is volumetric strain (red = dilation, blue = compaction). Salt and siliciclastic boundary marked by a dashed line in second and third column.
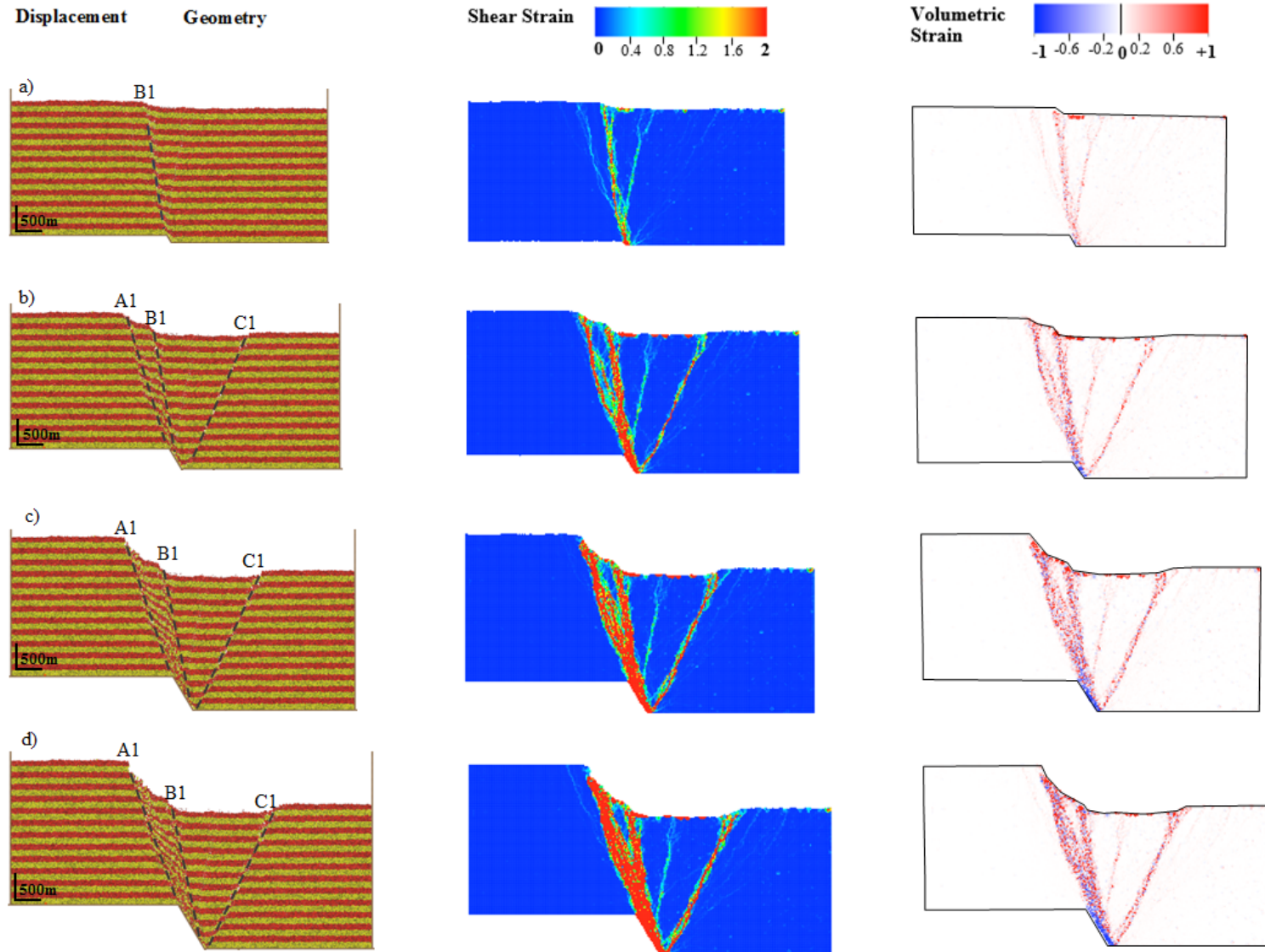
22

Figure 15: Model 3 at (a) 200, (b) 500, (c) 800, and (d) 1000 m major fault displacement. Left column is geometry, middle column is shear strain, and right column is 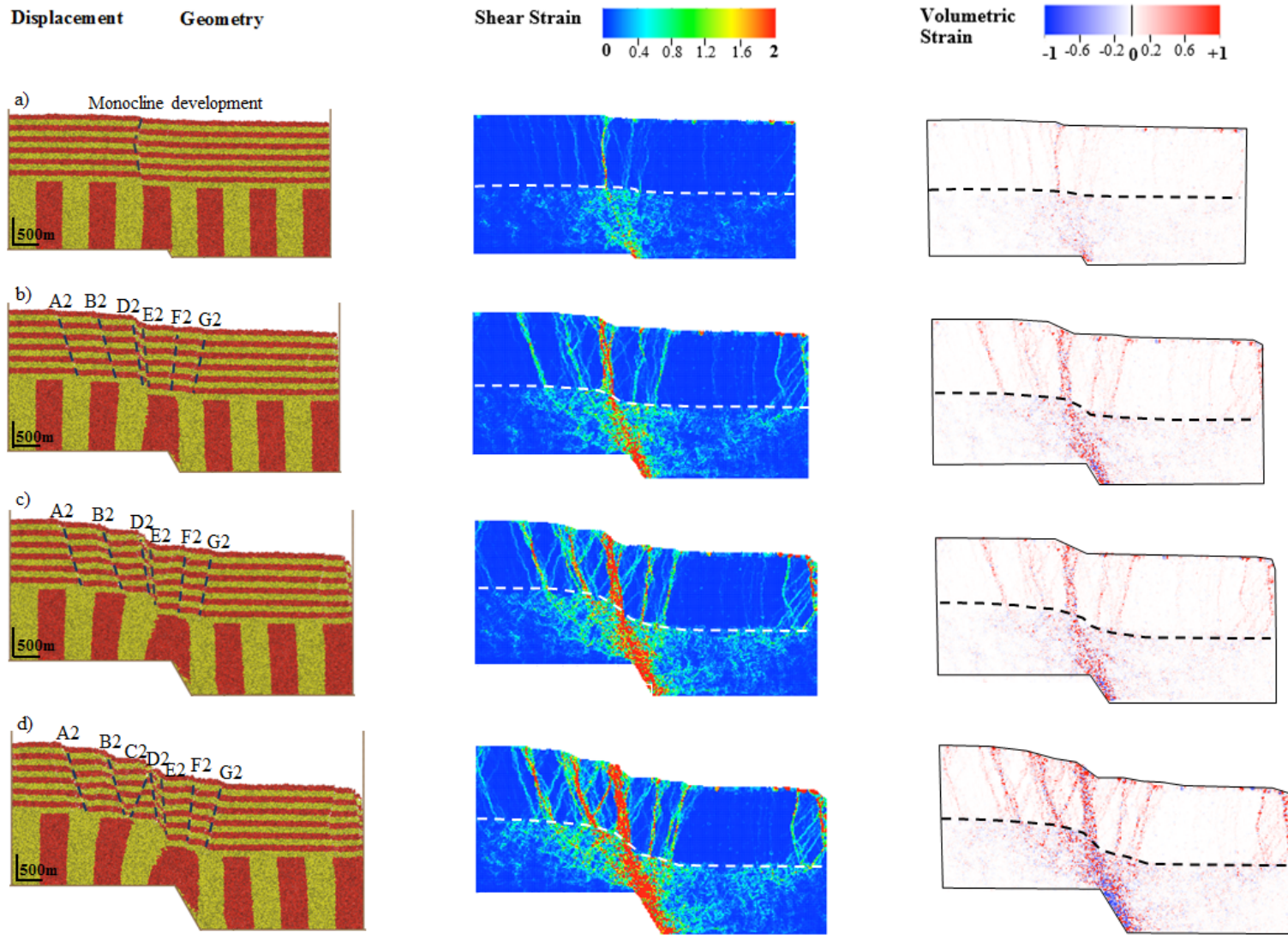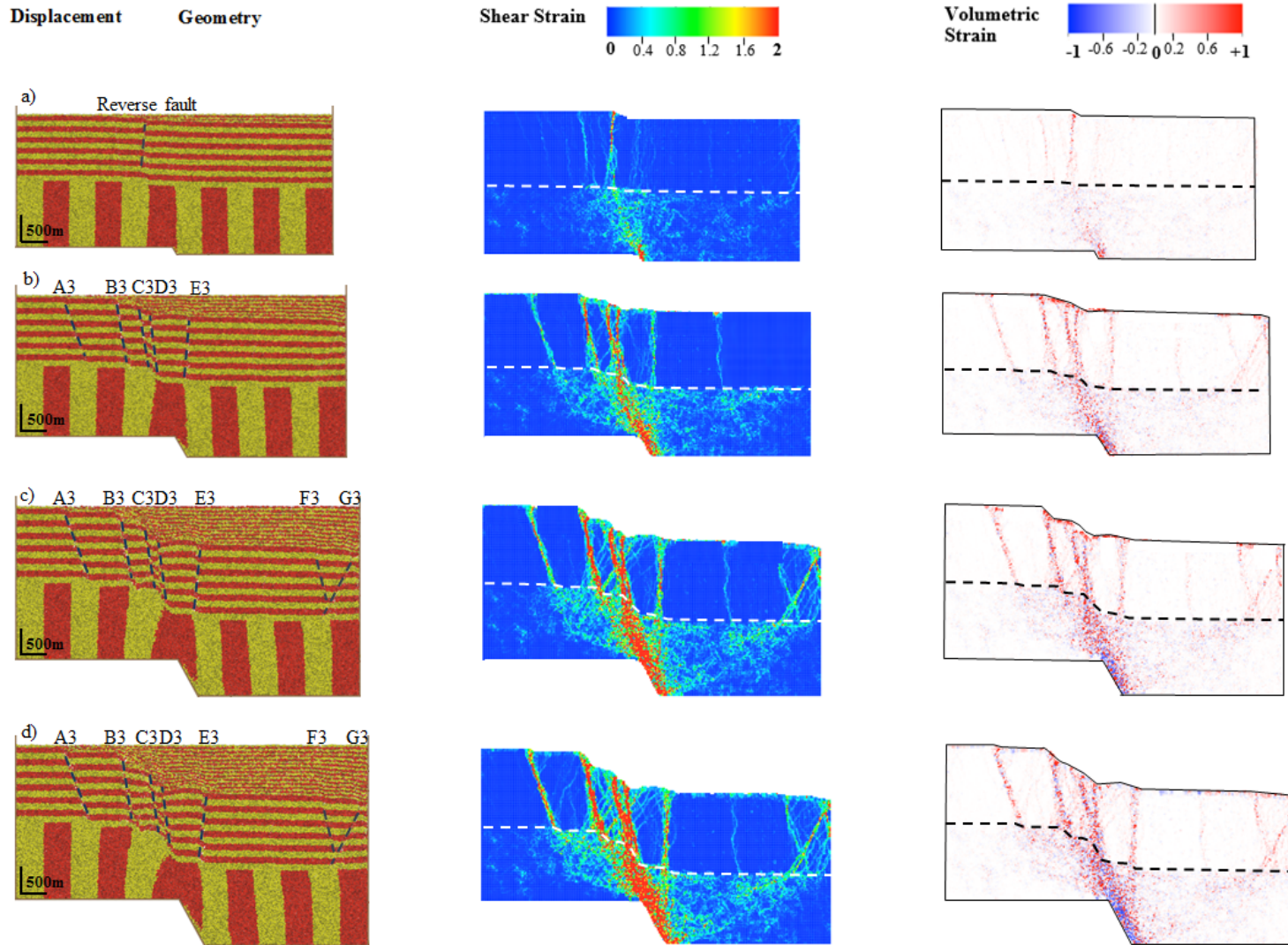volumetric strain (red = dilation, blue = compaction). Strain was not computed in the growth strata. Salt and siliciclastic boundary marked by a dashed line in second and third column.

23

3.1.1.4 Discussion: Mechanical Modeling

Model 1, with the absence of a ductile salt layer, shows mostly faulting localized directly above the major normal fault (Figure 13). In comparison, in model 2 with the presence of a ductile salt layer, deformation consists of forced folding and more widely distributed associated secondary faulting (Figure 14). The salt layer diffuses deformation in the brittle siliciclastic sequence because it cannot sustain high enough differential stresses to allow localized deformation due to its weak and ductile nature (Vendeville et al., 1995). In model 3, due to the additional load of growth strata, the secondary faulting appears more widely distributed. In model 2, fault A2, which is the furthest secondary fault from the major fault zone, is located ≈ 1800 m from the major normal fault. In comparison, in model 3, fault G3, which is the furthest fault from the major fault zone, is located ≈ 2600 m from the major normal fault. This indicates that the growth strata result in a wider distribution of secondary faulting. This is because, in addition to the salt layer, the growth strata is distributed throughout the entire model, thinning towards the footwall and thickening towards the hanging wall. Therefore the growth strata has the potential to induce deformation in more areas of the model due to the wide spread distribution of their loads.

Normal and reverse faulting are important deformation mechanisms in extensional forced folding (Jackson et al., 2006). Hardy (et al., 2011) stated that typically, models with a basement fault dip of less than 65° do not show the development of reverse faulting in the early stages of evolution. Models 2 and 3 have a 60° major fault dip, and at the earlier stage of evolution a reverse fault developed (Figures 14a and 15a). Therefore, the influence of a ductile salt layer, may have potentially initiated the development of these early reverse faults.

In the three models; the increase in major fault displacement causes an increase in deformation in existing structural geometries and production of new structures, which is shown, as shear strain and volumetric strain increases. The closer the faults are to the major fault zone, the higher the shear strain and volumetric strain, as more deformation occurs. The highest shear strain regions correlate with the highest dilation and compaction. The sediments associated with these models do not conform to source, reservoir and seal rock to observe possible plays, however only structures will be observed. With this in mind, potential trapping structures are produced from models 2 and 3, such as tilted fault blocks in the footwall of models 2 and 3 and the anticlinal structure in model 3.

3.2 Changes of seismic properties

Seismic imaging simulation requires an input reflectivity model at a given amount of fault displacement. In models 1, 2 and 3 fault displacement of 200, 500, 800, and 1000 m are chosen to seismic image. This can provide an understanding of the impact of deformation on the seismic image. To compute seismic properties in the faulting structures, elastic properties are assigned to sandstone, shale and salt before faulting, which are average values from the literature (Table 2; Mavko et al., 2009). In models 1, 2 and 3, the computed volumetric strain at 200, 500, 800, and 1000 m fault displacement (Figures 13, 14 and 15) are used to modify the initial elastic properties (Table 2) using equations 1-4. The initial values of salt are not modified, as salt is ductile and their properties may not vary significantly. The initial property values for growth strata are not modified, mainly because growth strata in comparison to pre-growth is fairly unconsolidated and behaves differently. Also although growth strata properties may change with deformation, they do less than the pre-growth, because the growth strata are less deformed. Therefore, assuming no change of properties in the growth strata induces relatively small errors. It facilitates the workflow though, because finite strain in the growth strata must be computed incrementally, thus taking a fair amount of time for each simulation. Figures 16 to 19 shows the changes of density and seismic velocities at 200, 500, 800 and 1000 m fault displacement in models 1, 2 and 3. The zones of deformation, consisting of forced folding and faulting, result in more density and velocity changes (Figures 16 to 19). The density and velocity changes are higher at the later stages of the models (i.e. 1000 m major fault displacement).

Figure 16: Density changes (left column) and seismic velocity changes (right column) at 200 m of major fault displacement. Model 1 (first row), model 2 (second row), model 3 (third row). The growth strata in model 3 is assumed to not experience property changes.

Figure 17: Density changes (left column) and seismic velocity changes (right column) at 500 m of major fault displacement. Model 1 (first row), model 2 (second row), model 3 (third row). The growth strata in model 3 is assumed to not experience property changes.

27

Figure 18: Density changes (left column) and seismic velocity changes (right column) at 800 m of major fault displacement. Model 1 (first row), model 2 (second row), model 3 (third row). The growth strata in model 3 is assumed to not experience property changes.
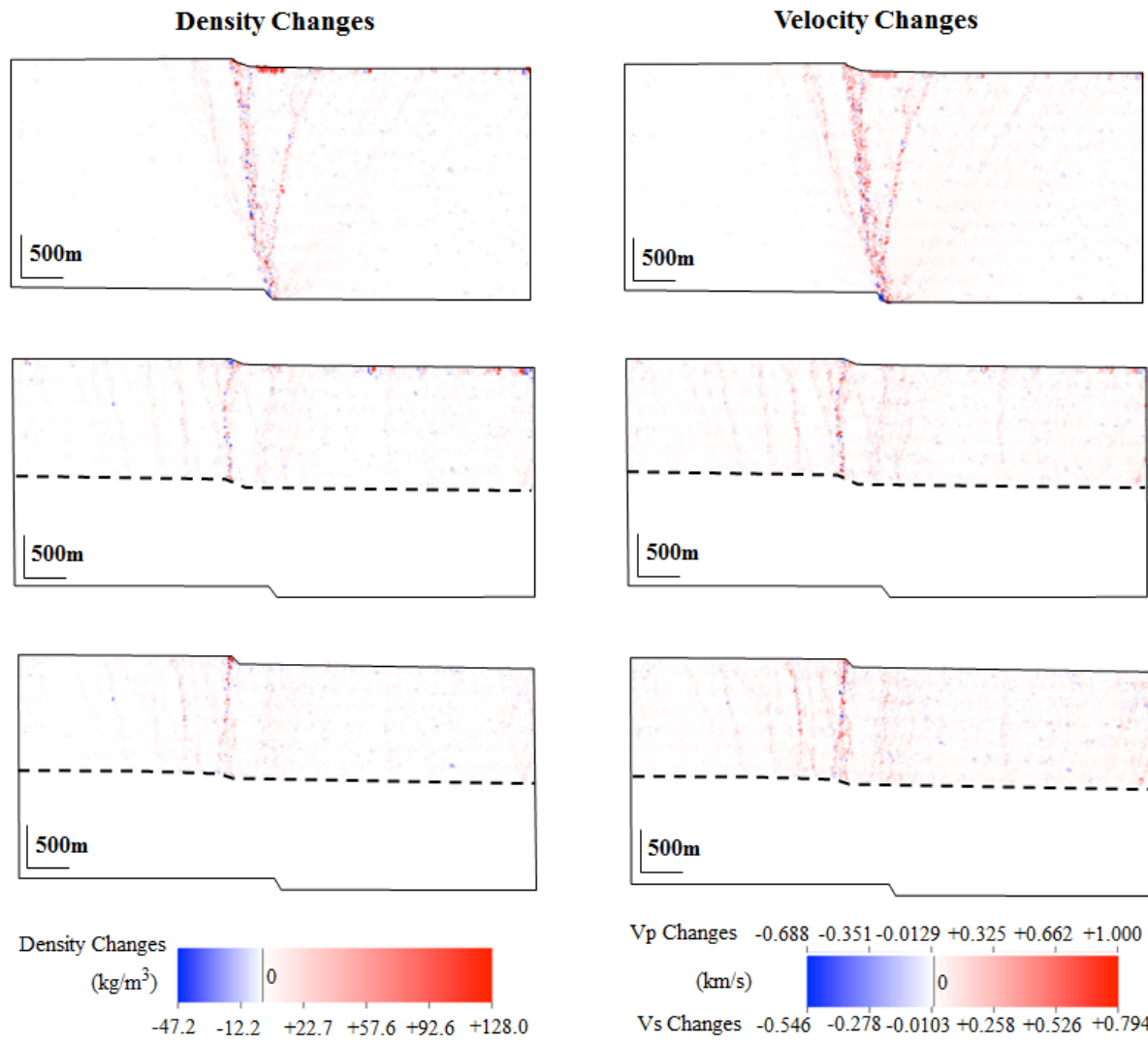
Figure 19: Density changes (left column) and seismic velocity changes (right column) at 1000 m of major fault displacement. Model 1 (first row), model 2 (second row), model 3 (third row). The growth strata in model 3 is assumed to not experience property changes.
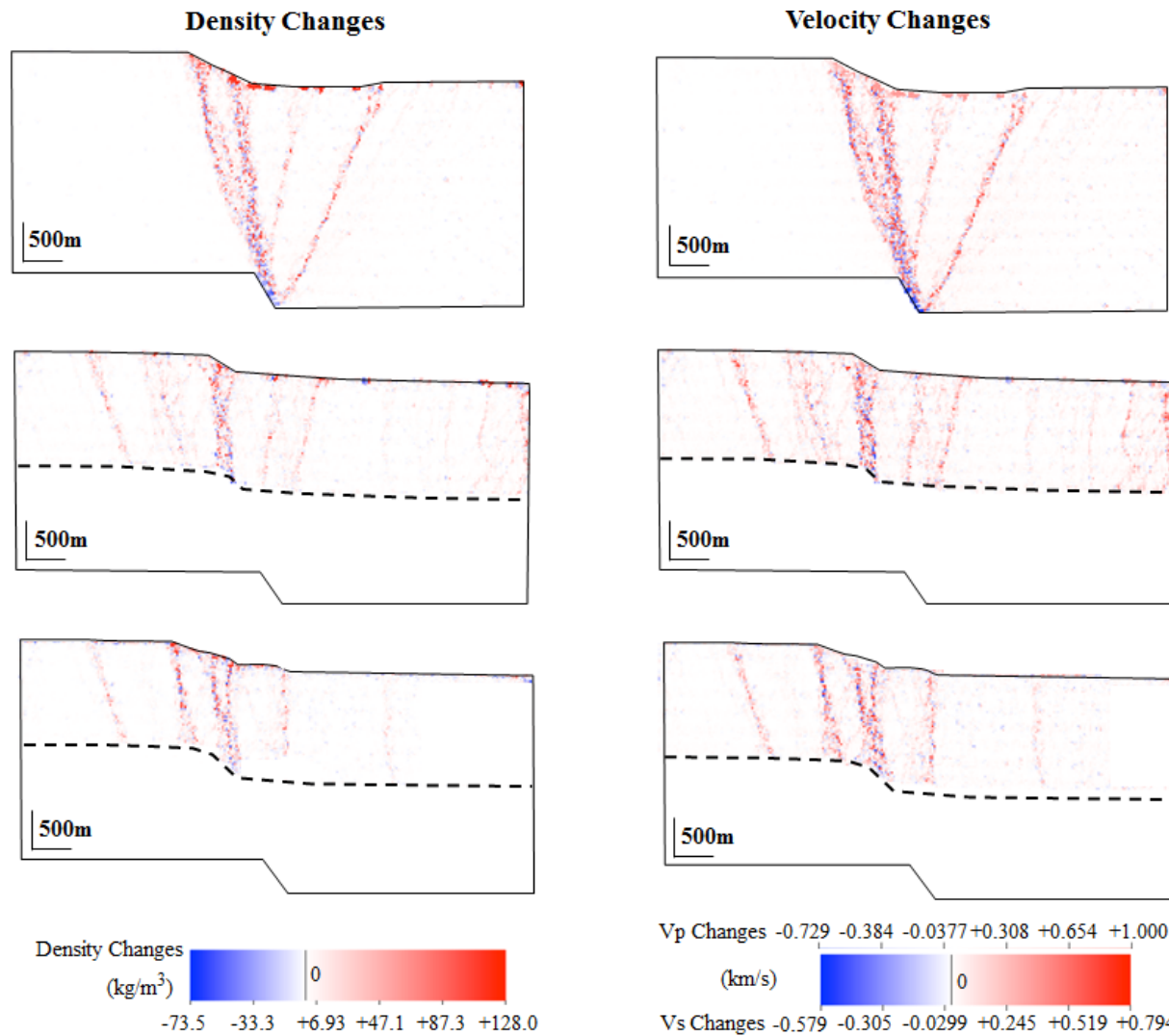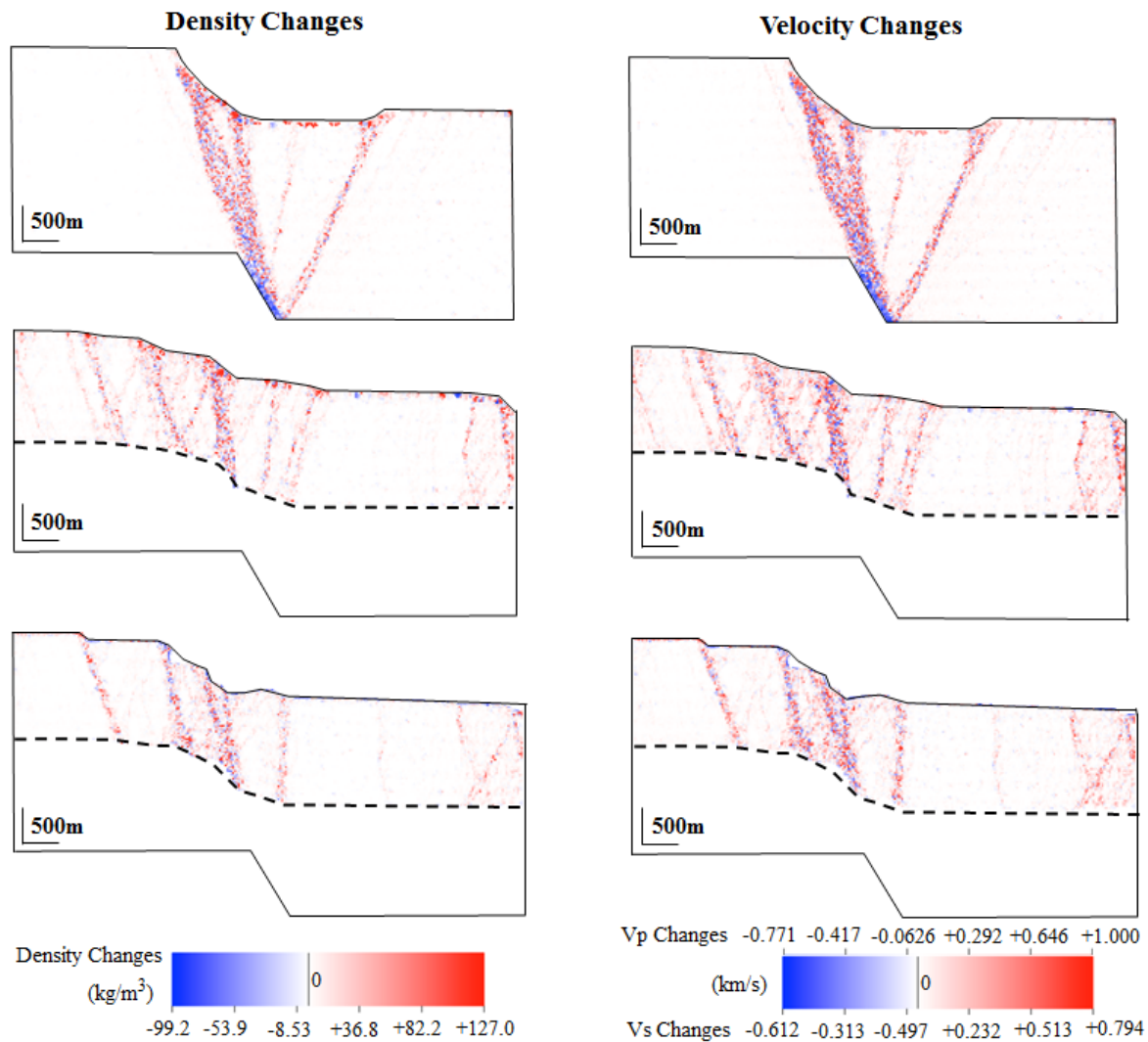
29

3.3 Seismic Imaging

Sensitivity studies were ran to illustrate the impact of faulting and extensional forced folding and its associated secondary faulting on the resultant seismic image. The model parameters explored are illumination direction and wave frequency. Other parameters that were kept fixed in the model are background model, overburden, survey geometry, and wave type (Botter et al., 2014). The PSDM simulator was set at a depth of 1 km for a homogeneous sandstone-like overburden with a P-wave velocity of 4.0 km/s, S-wave velocity of 2.4 km/s, and density of 2.4 g/cm^3. The wave frequency consists of a zero-phase Ricker pulse of 10 to 40 Hz (Figure 20). Ricker pulse is a zero-phase wavelet, meaning the wavelet is symmetrical with a maximum amplitude at time zero (Botter et al., 2014). Figure 21 shows P-wave velocity (Vp), S-wave velocity (Vs) and density (ƿ) in the input models; specifying that the assignment of lower values represent shale (blue layers) and the assignment of larger values represent sandstone (pink layers). These elastic properties are required to generate the reflectivity grid. Figure 22 shows the reflectivity grids at an incident angle of 0º for models 1 to 3 at different fault displacements. These reflectivity grids are the input of the PSDM simulator.

There are some parameters of particular importance in seismic imaging and interpretation, which will be evaluated in the resultant seismic images. Reflector continuity is a direct response to how continuous the sedimentary beds are, and is vital for interpretation of the sedimentary environment (Bjorlykke, 2010) and faulting. Reflection amplitude is important as it shows the strength of the reflections at layer boundaries, which are dependent on the difference in acoustic impedance between these layer boundaries. The acoustic impedance (Z) of an interface is dependent upon density (ƿ) and velocity (v), as expressed by the equation $Z = Vp \cdot ƿ$. Table 3 shows calculations of the acoustic impedance of salt, sandstone and shale, using density and velocity values from table 2. It is challenging to relate acoustic impedance to a specific rock property, however, generally the harder and denser a rock is, the higher its acoustic impedance (Kearey et al., 2002).

	P-wave velocity (Vp) (m/s)	Density (p) (kg/m³)	Acoustic Impedance
Salt	4500	2160	$Z = Vp \cdot p = 9.7 \cdot 10^6$
Sandstone	4000	2650	$Z = Vp \cdot p = 10.6 \cdot 10^6$
Shale	2000	2650	$Z = Vp \cdot p = 5.3 \cdot 10^6$

Table 3: Calculations of acoustic impedance
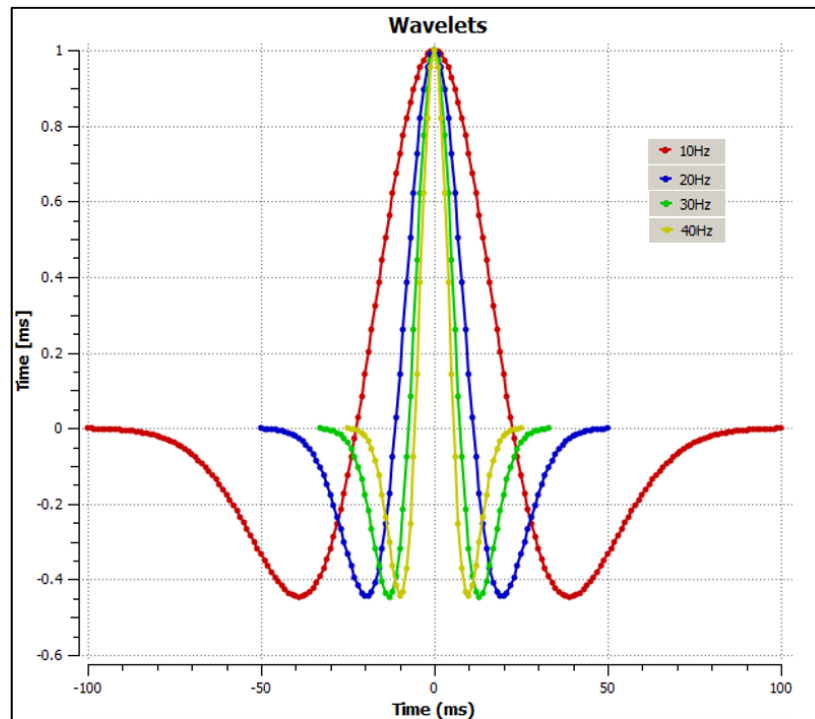
Figure 20: Zero-phase Ricker pulses of 10 to 40 Hz
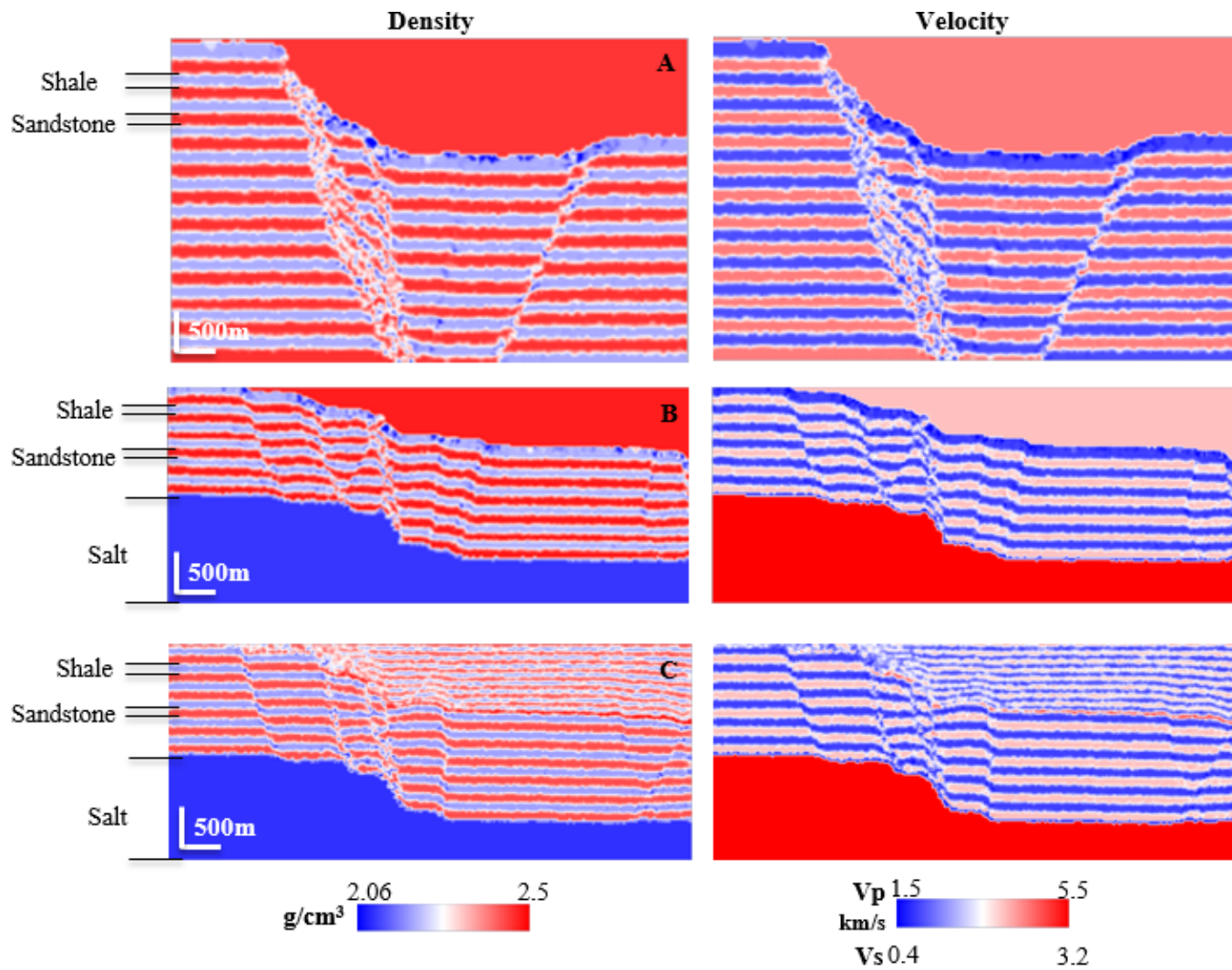
Figure 21: Density (left column) and Seismic velocity (right column); specifying the layers that represent salt, sandstone and shale. In Models 1 and 2, the overburden is sandstone-like. (A) Model 1, (B) Model 2, (C) Model 3.

32
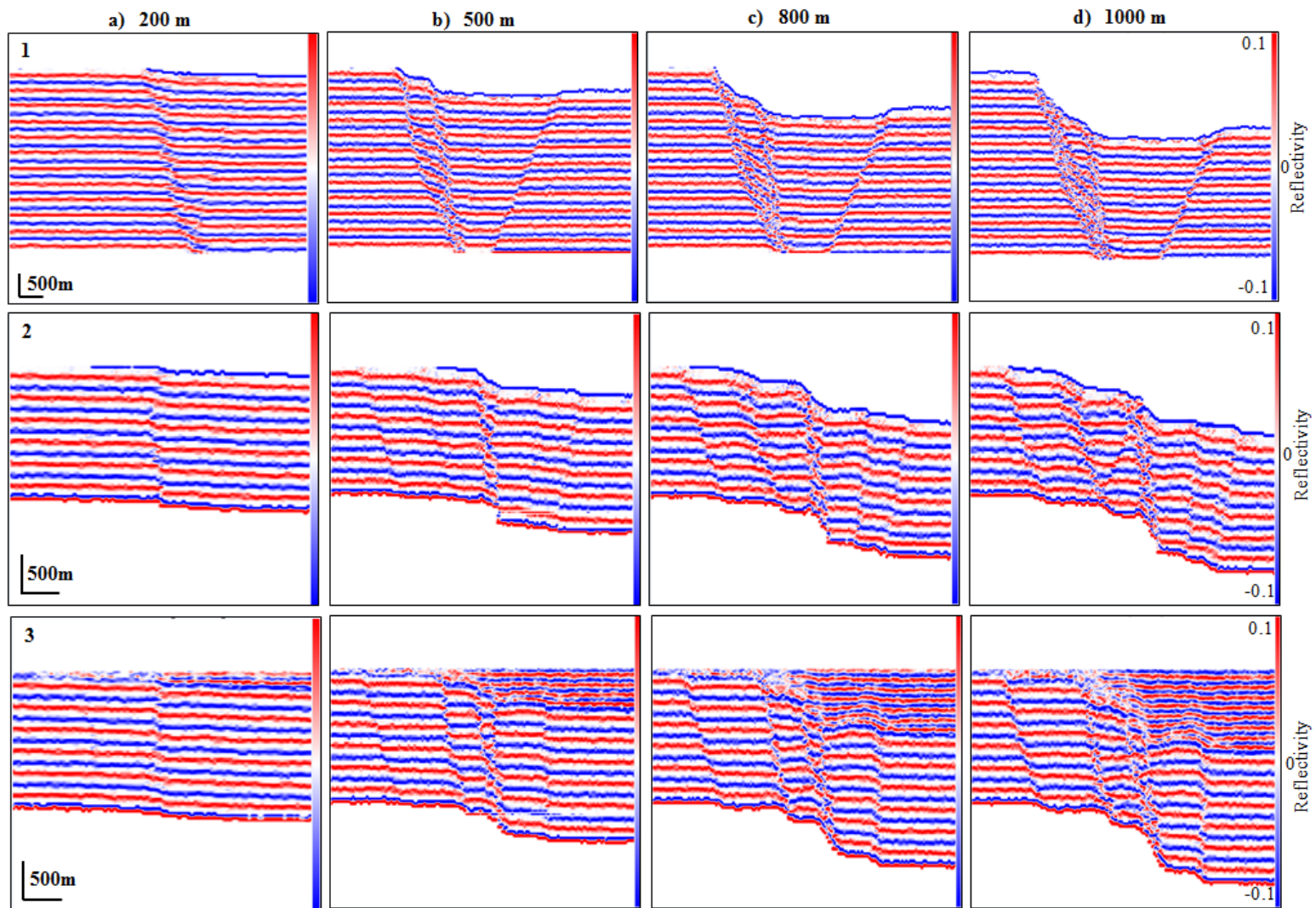
Figure 22: Reflectivity grid at an incident angle of 0º. Columns correspond to major fault displacement: (a) 200, (b) 500, (b) 800, and (d) 1000 m. First row; model 1, second row; model 2 and third row; model 3.

Illumination can be defined as seismic wave energy hitting a reflector and reflected, therefore producing the resultant seismic image (Laurain et al., 2004). The illumination direction allows choosing a specific part of the model image, therefore impacting the total fault volume illuminated in the seismic image (Botter et al., 2014). Three different illumination directions are used in this study: specular, left (from the footwall) and right (from the hanging wall) side illuminations. A survey is how the seismic vessel acquires the seismic response. In SeisRoX software there are three survey options: fixed, marine and coil. In this thesis the marine survey type is used. To achieve a specular illumination, the survey consists of a single streamer centered at the fault (Botter et al., 2014). To achieve a left and right side illumination, the survey consists of a single streamer offset towards the footwall or hanging wall of the normal fault (Botter et al., 2014).

SeisRoX software requires the survey to define the shot and streamer/receiver configuration (Table 4). The shot configuration consists of defining the number of shot lines, shot line length, shot line spacing, and shot spacing. Shot line spacing is the distance between each shot line. Shot spacing is the distance between each shot on one single line. The streamer/receiver configuration consists of defining the minimum offset, number of streamers, streamer length, streamer spacing and receiver spacing. The minimum offset is the distance from the source to the nearest receiver on the streamer. The streamer spacing is the distance between separate streamers. The receiver spacing is the distance between each receiver on the streamer.

Shot Configuration	
Number of shot lines	1
Shot line length (km)	60
Shot line spacing (km)	0.3
Shot spacing (km)	0.1

Streamer/Receiver Configuration	
Minimum offset (km)	0.1
Number of streamers	6
Streamer length (km)	2
Streamer spacing (km)	0.2
Receiver spacing (km)	0.025

Table 4: Shot configuration and streamer/receiver configuration.

Figure 23 shows the illumination vector I_{SR}, which is defined around one considered reference point in a background model (Lecomte, 2008). The background model shows raypaths to demonstrate the propagation effect (Figure 23a; Lecomte, 2008). p_R and p_S are two local vectors and the difference between these two vectors is defined as the $I_{SR} = p_R - p_S$. p_S is attached to the incident wave (from source S) and p_R is attached to the scattered wave (toward receiver R) (Lecomte, 2008). θ_{SR} is the incident angle between $- p_S$ and p_R (Figure 23b). The illumination and resolution of the PSDM simulated seismic images at the reference point are dependent upon the orientation and length of the illumination vector (I_{SR}) (Lecomte et al., 2016). For example, the illumination of horizontal reflectors will be imaged on seismic, if the illumination vector is vertical (Lecomte et al., 2016). Similarly, the illumination of vertical reflectors will be imaged on seismic, if the illumination vector is horizontal (Lecomte et al., 2016).
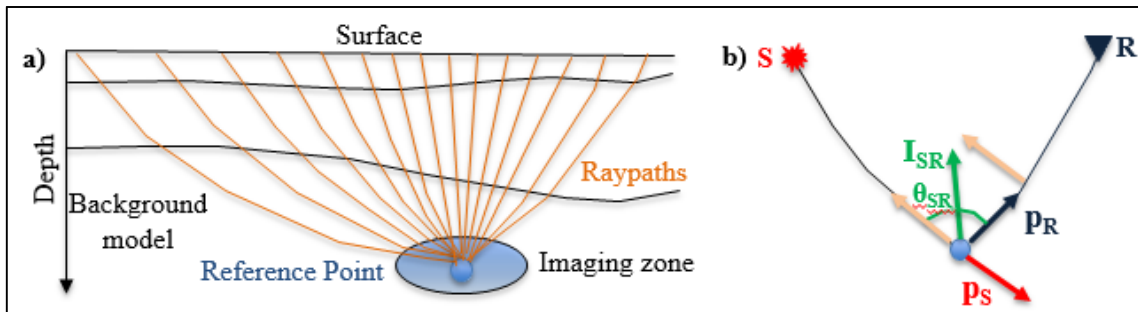
Figure 23: Illumination vector (a) Raypaths illustrate the propagation effect in the background model. (b) Illumination vector (I_{SR}), (S = source and R = receiver) (Modified from Lecomte et al., 2016).

When illumination vectors at any image point in depth have been verified, illumination plots can be generated (Lecomte and Kaschwich, 2008). The illumination vectors are illustrated in a rose diagram, showing the azimuth and dip of potentially illuminated reflectors (Figure 24). The coloured sections in the plots refer to the number of illumination vectors, which are correlated to the colour scale (Figure 24). The illumination vectors are selected according to the dip angles of the reflectors. Figure 24a shows the specular illumination, where reflectors dipping less than 10° are illuminated. Figures 24b and 24c show the left side and right side illumination, respectively. These offside illuminations illuminate reflectors dipping more than 10°, therefore the flat reflectors outside the fault zone, are poorly imaged.
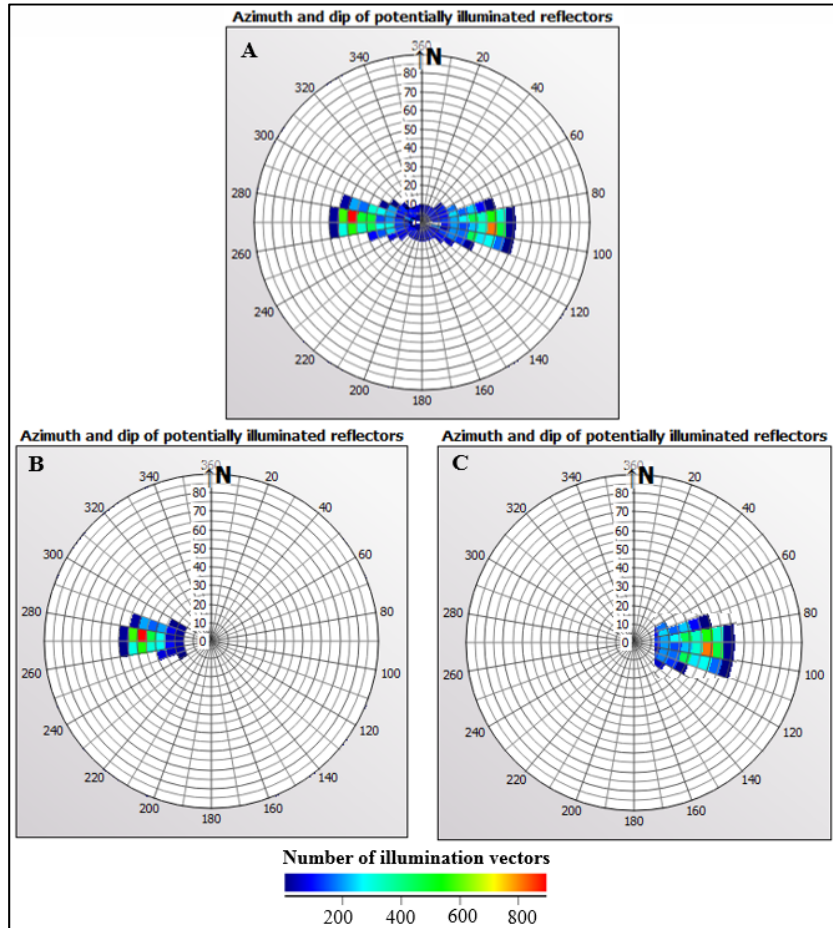
Figure 24: Illumination vectors: (A) specular illumination, (B) left side illumination, and (C) right side illumination.

3.3.1 Impact of illumination direction

In models 1, 2 and 3, different stages of deformation are chosen to seismic image: 200, 500, 800 and 1000 m major fault displacement, which can provide an understanding of the impact of deformation on the seismic image.

3.3.1.1 Model 1

Specular illumination, at all evolutionary stages of this model, clearly images the flat reflectors, which are located outside the fault zone (Figures 25 to 32). In these areas, the salt-siliciclastic and shale-sandstone interfaces have a strong amplitude and are clearly imaged. At a low frequency of 10 Hz, the salt-siliciclastic and shale-sandstone interfaces are difficult to distinguish, due to the reflectors large width, indicating its low resolution (Figures 25, 27, 29, and 31). Therefore at a high frequency of 20 to 40 Hz, the interfaces are better distinguished

(Figures 25 to 32). At 200 m major fault displacement, the faulted monocline is visible by curved continuous reflectors (Figures 25 and 26). For specular illumination, from 500 to 1000 m major fault displacement, the fault-related diffractions are also visible; as well as the synthetic faults A1 and B1 and antithetic fault C1, by the offset of the reflectors (Figures 27 to 32).

The offside (left and right side) illuminations poorly image the flat reflectors, as these illuminations only target dipping reflectors on the fault planes and folds limbs. The left side illumination at 500 to 1000 m fault displacement illuminates the antithetic fault plane (Figures 27 to 32). In comparison, the faulted monocline at 200 m fault displacement and synthetic faults at 500 to 1000 m fault displacement are poorly imaged, when using the left side illumination, as it generates low amplitude, weak and blurry reflectors, which make distinguishing the layers and location of the faults challenging. Despite the poor imaging of these structures, the diffracted energy of these structures are evident in the resultant seismic image (Figures 25 to 32). The higher frequencies of 20 to 40 Hz with left side illumination, produces a better seismic image of the antithetic fault plane (fault C1) and the fault related diffracted energy. In the seismic sections, the internal structure of the antithetic fault (fault C1) appears as a line, as it is one single fault with no other geological features located within a close location.

The right side illumination, at all evolutionary stages of model 1, targets the synthetic fault zone with strong reflections (Figures 25 to 32). Although the antithetic fault is poorly imaged with the use of right side illumination, the diffracted energy from this fault is evident in the seismic image (Figures 27 to 32). The higher frequencies of 20 to 40 Hz with right side illumination, produces a better seismic image of the faulted monocline and the synthetic faults, where the reflectors are better defined and there is a strong reflection amplitude of these structures (Figure 25 to 32). With regards to the evolution of the model, the more deformed the siliciclastic sediments are, the higher the intensity on the resultant seismic image. For example, although the antithetic fault plane is visible at the earlier stage of 500 m major fault displacement, the structure has a lower amplitude in comparison to the later stages of the model (800 m and 1000 m major fault displacement). In the seismic sections, the synthetic faults appear as an area in the footwall, as the development of the normal fault scarp

evidently divides the hanging wall and footwall of the model, creating a depression, resembling a graben structure.

Figure 25: PSDM seismic images of model 1 at 200 m major fault displacement. The columns correspond to three different illumination directions: specular (left), left side (center) and right side (right). The rows correspond to two different frequencies: 10Hz (first row) and 20Hz (second row). The PSDM filter and point spread function (PSF) are shown above each seismic image.

Figure 26: PSDM seismic images of model 1 at 200 m major fault displacement. The columns correspond to three different illumination directions: specular (left), left side (center) and right side (right). The rows correspond to two different frequencies: 30Hz (first row) and 40Hz (second row). The PSDM filter and point spread function (PSF) are shown above each seismic image.

Figure 27: PSDM seismic images of model 1 at 500 m major fault displacement. The columns correspond to three different illumination directions: specular (left), left side (center) and right side (right). The rows correspond to two different frequencies: 10Hz (first row) and 20Hz (second row). The PSDM filter and point spread function (PSF) are shown above each seismic image.

40
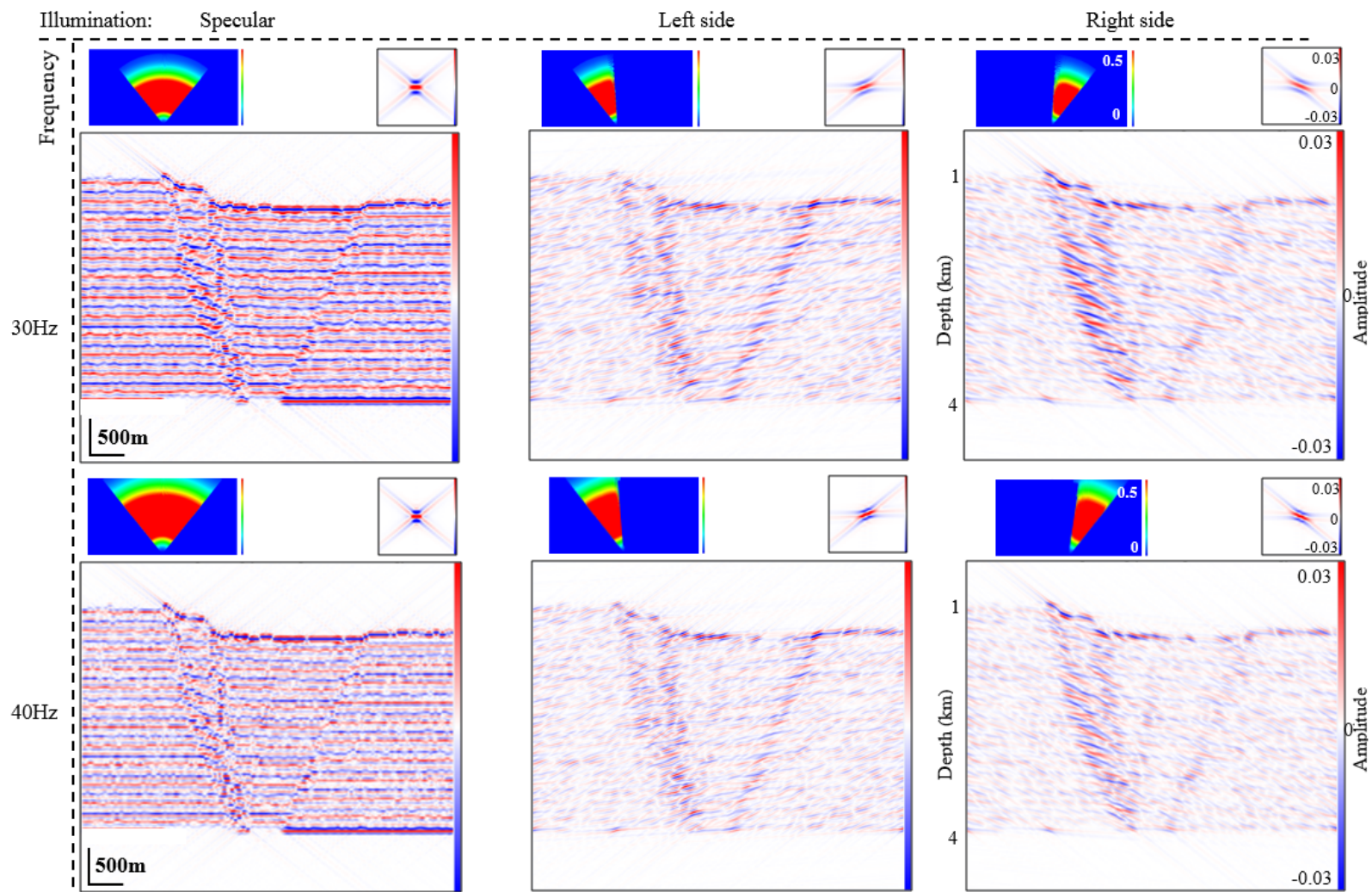
Figure 28: PSDM seismic images of model 1 at 500 m major fault displacement. The columns correspond to three different illumination directions: specular (left), left side (center) and right side (right). The rows correspond to two different frequencies: 30Hz (first row) and 40Hz (second row). The PSDM filter and point spread function (PSF) are shown above each seismic image.
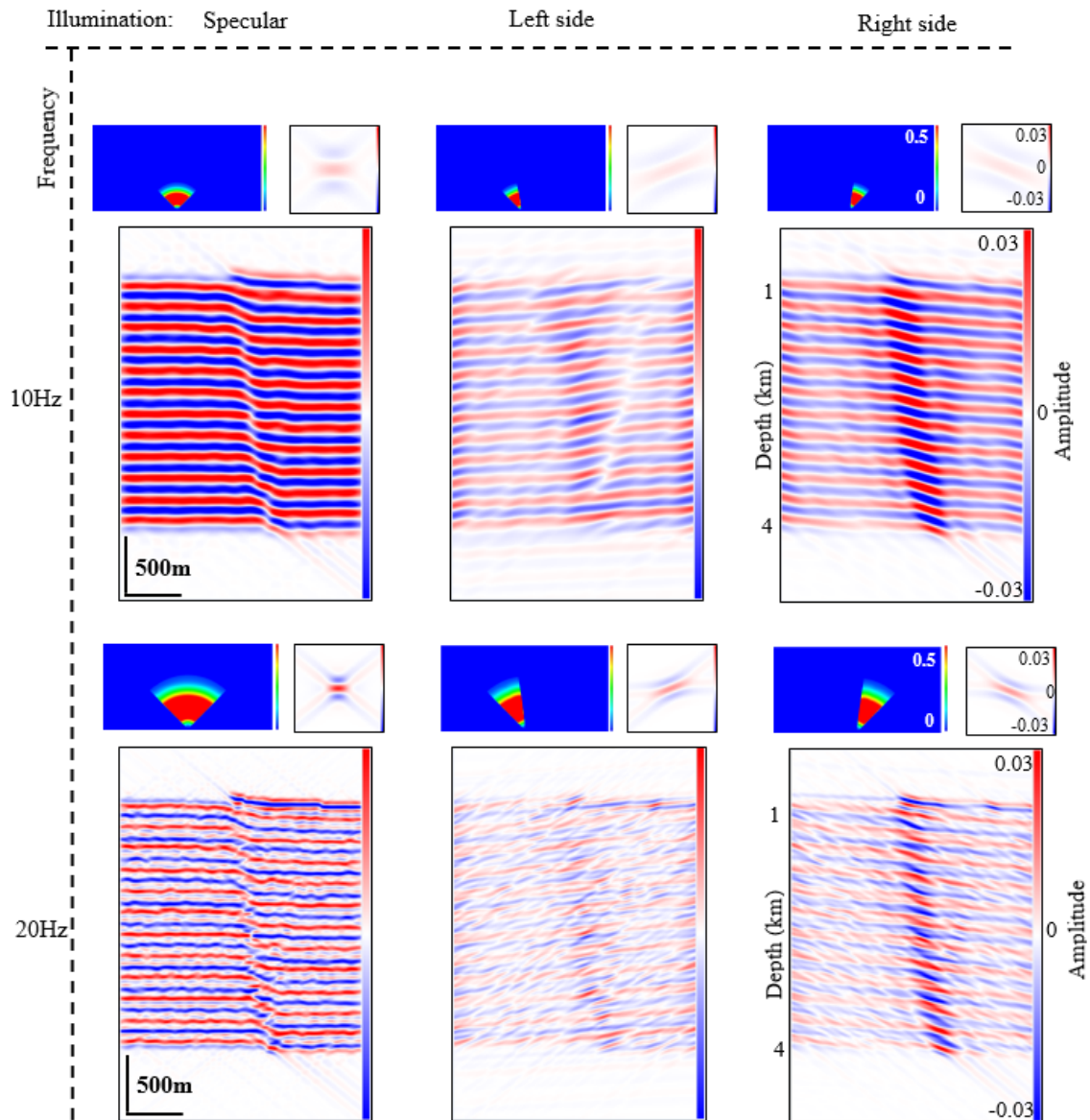
41
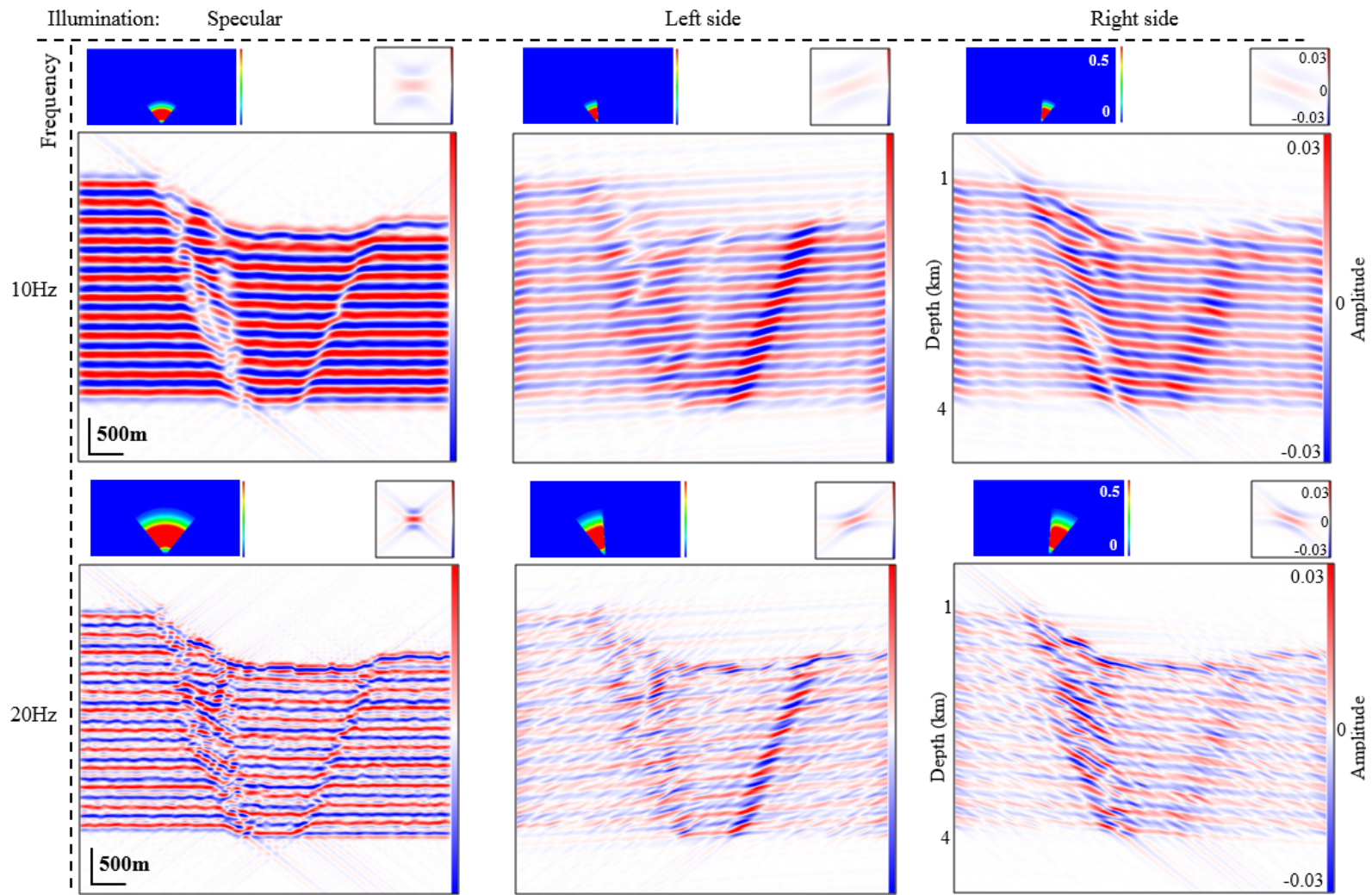
Figure 29: PSDM seismic images of model 1 at 800 m major fault displacement. The columns correspond to three different illumination directions: specular (left), left side (center) and right side (right). The rows correspond to two different frequencies: 10Hz (first row) and 20Hz (second row). The PSDM filter and point spread function (PSF) are shown above each seismic image.
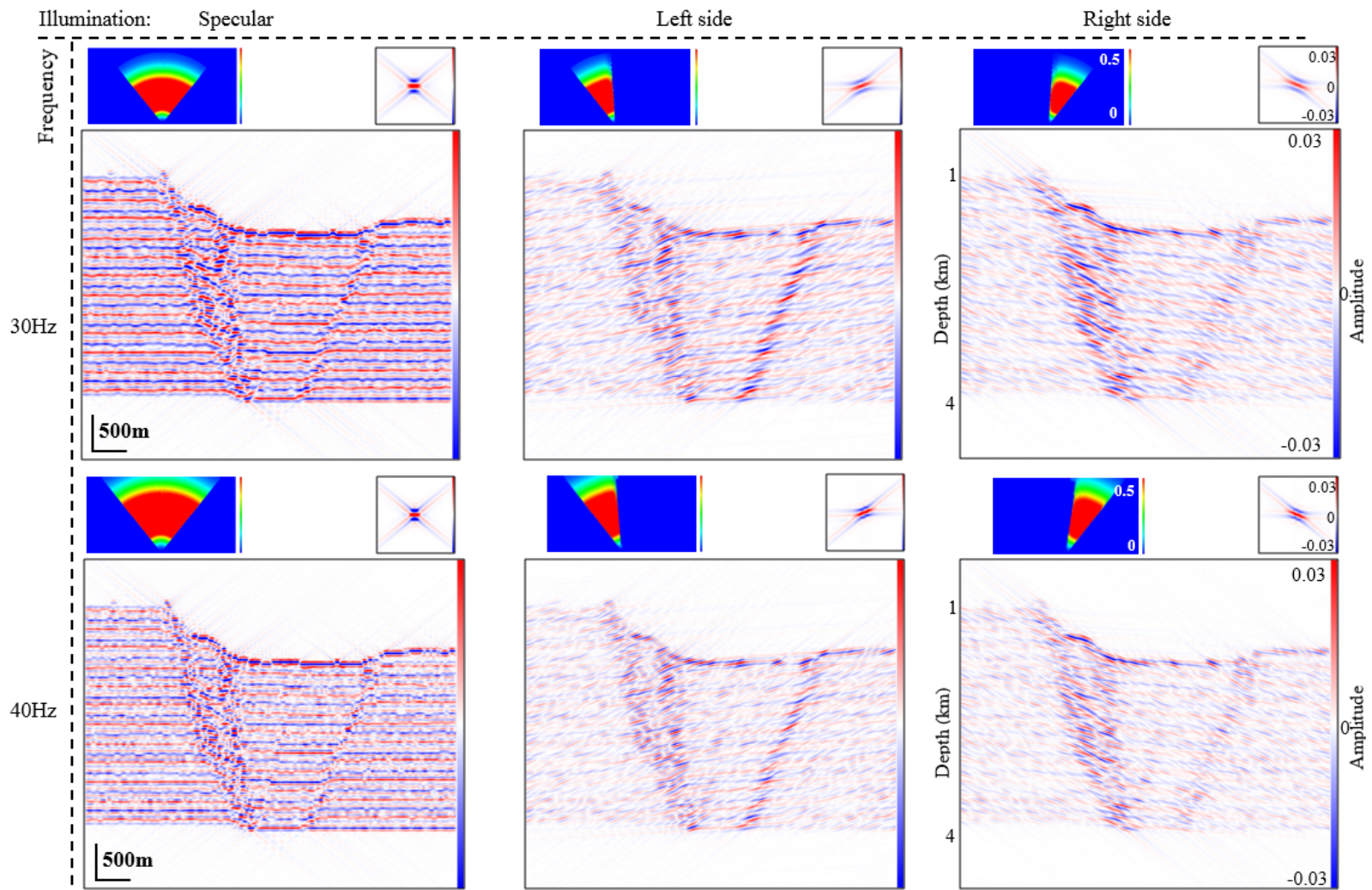
Figure 30: PSDM seismic images of model 1 at 800 m major fault displacement. The columns correspond to three different illumination directions: specular (left), left side (center) and right side (right). The rows correspond to two different frequencies: 30Hz (first row) and 40Hz (second row). The PSDM filter and point spread function (PSF) are shown above each seismic image.
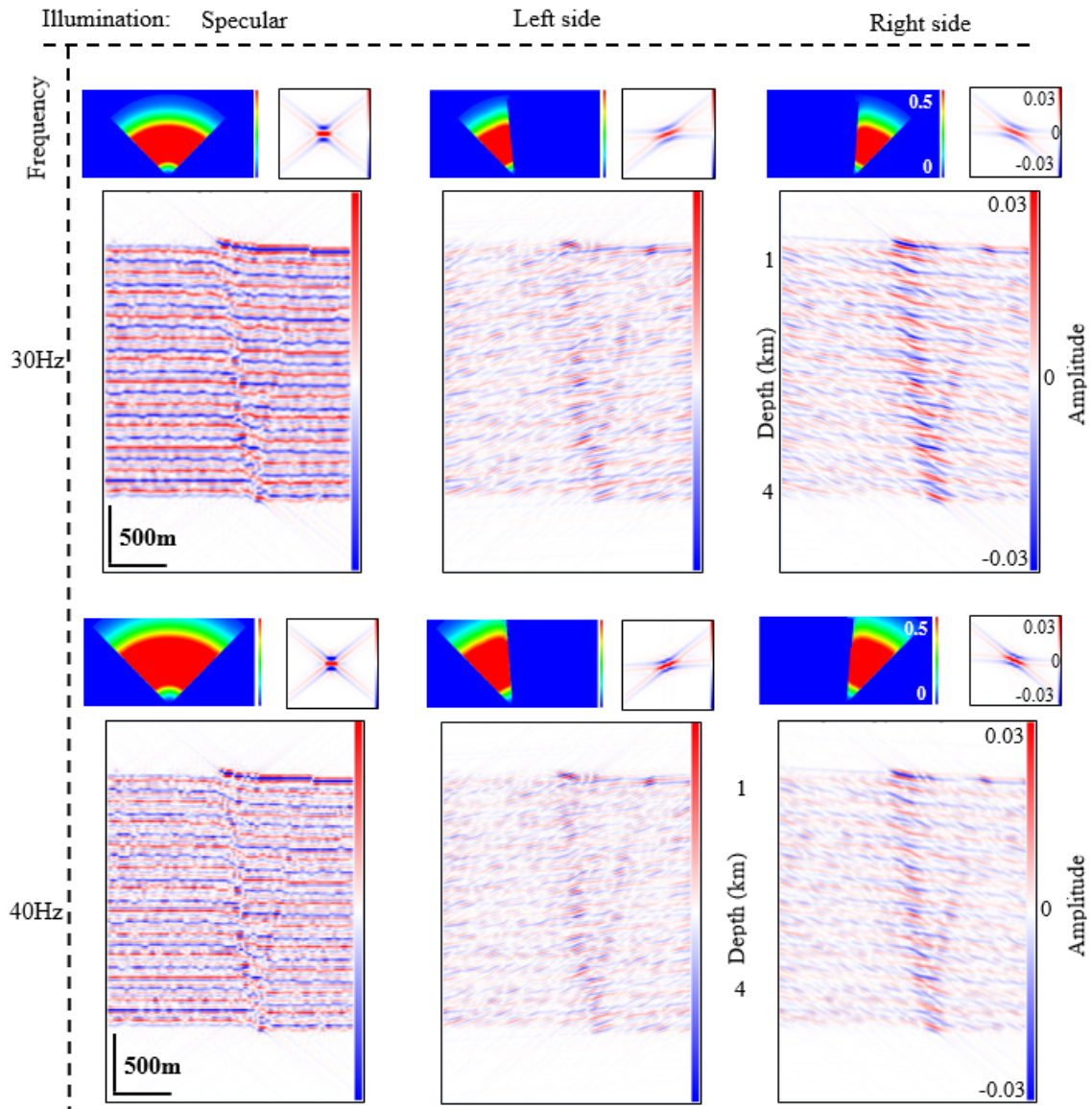
43
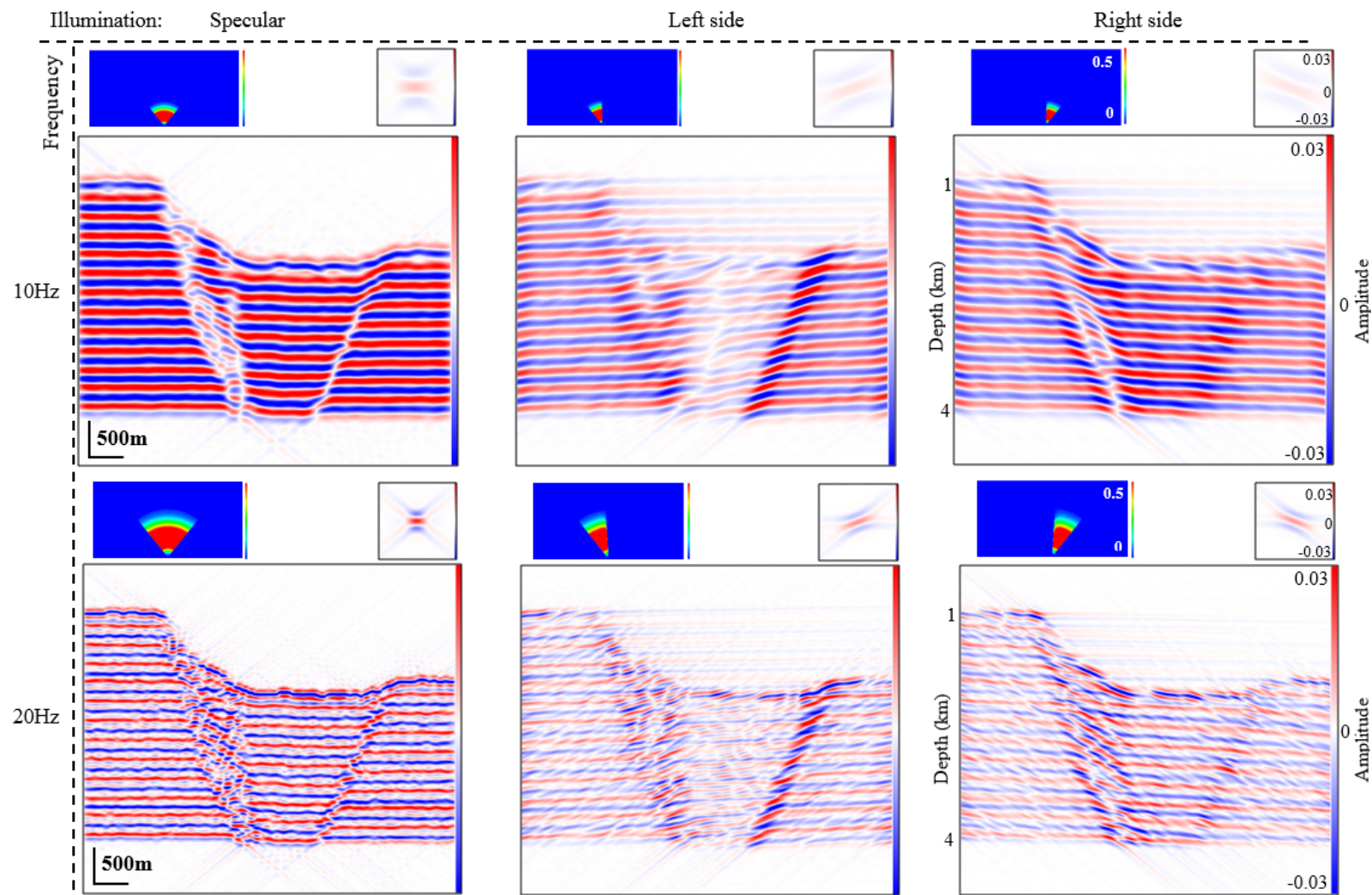
Figure 31: PSDM seismic images of model 1 at 1000 m major fault displacement. The columns correspond to three different illumination directions: specular (left), left side (center) and hanging wall or right side (right). The rows correspond to two different frequencies: 10Hz (first row) and 20Hz (second row). The PSDM filter and point spread function (PSF) are shown above each seismic image.
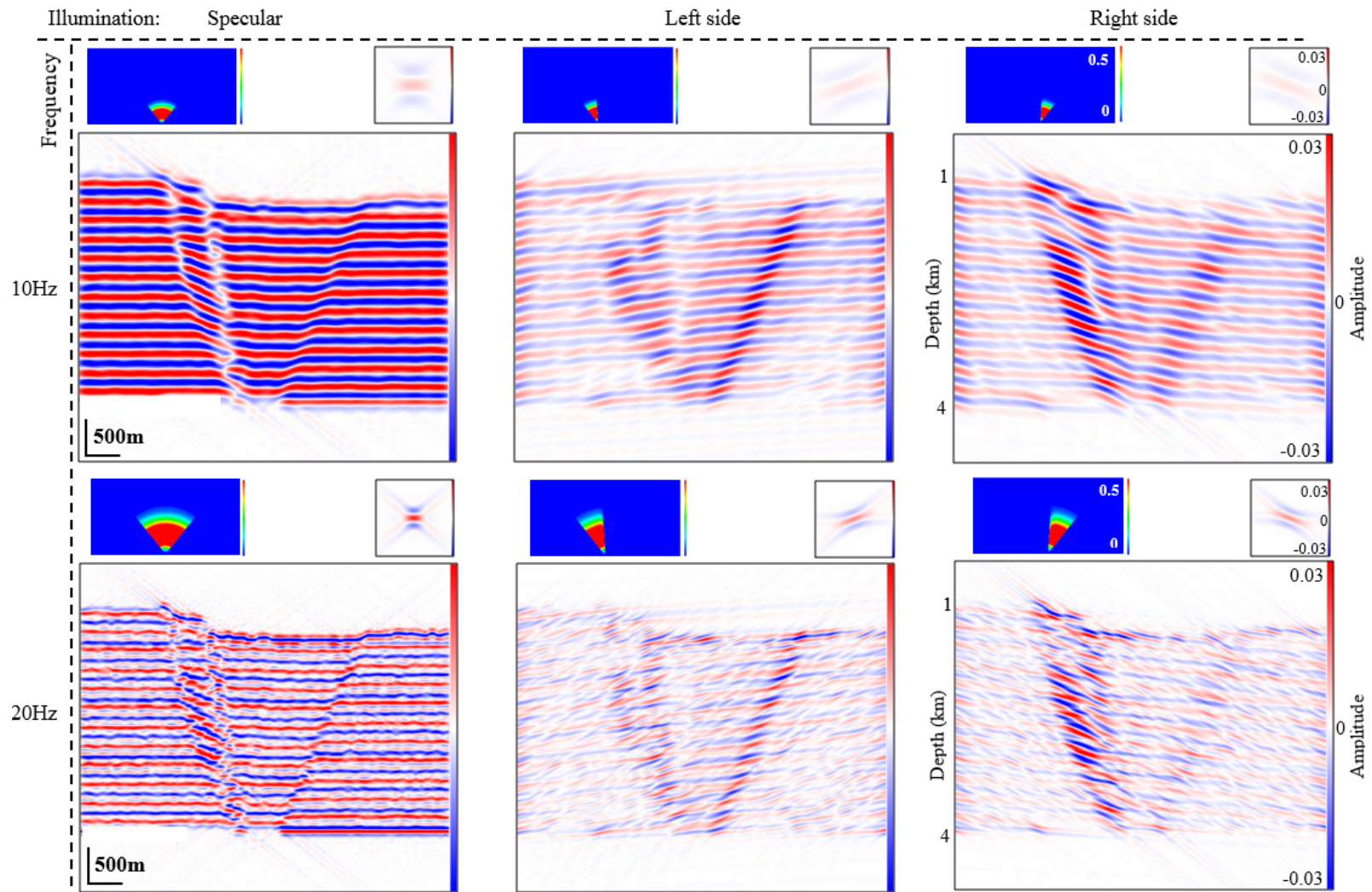
Figure 32: PSDM seismic images of model 1 at 1000 m major fault displacement. The columns correspond to three different illumination directions: specular (left), left side (center) and right side (right). The rows correspond to two different frequencies: 30Hz (first row) and 40Hz (second row). The PSDM filter and point spread function (PSF) are shown above each seismic image.
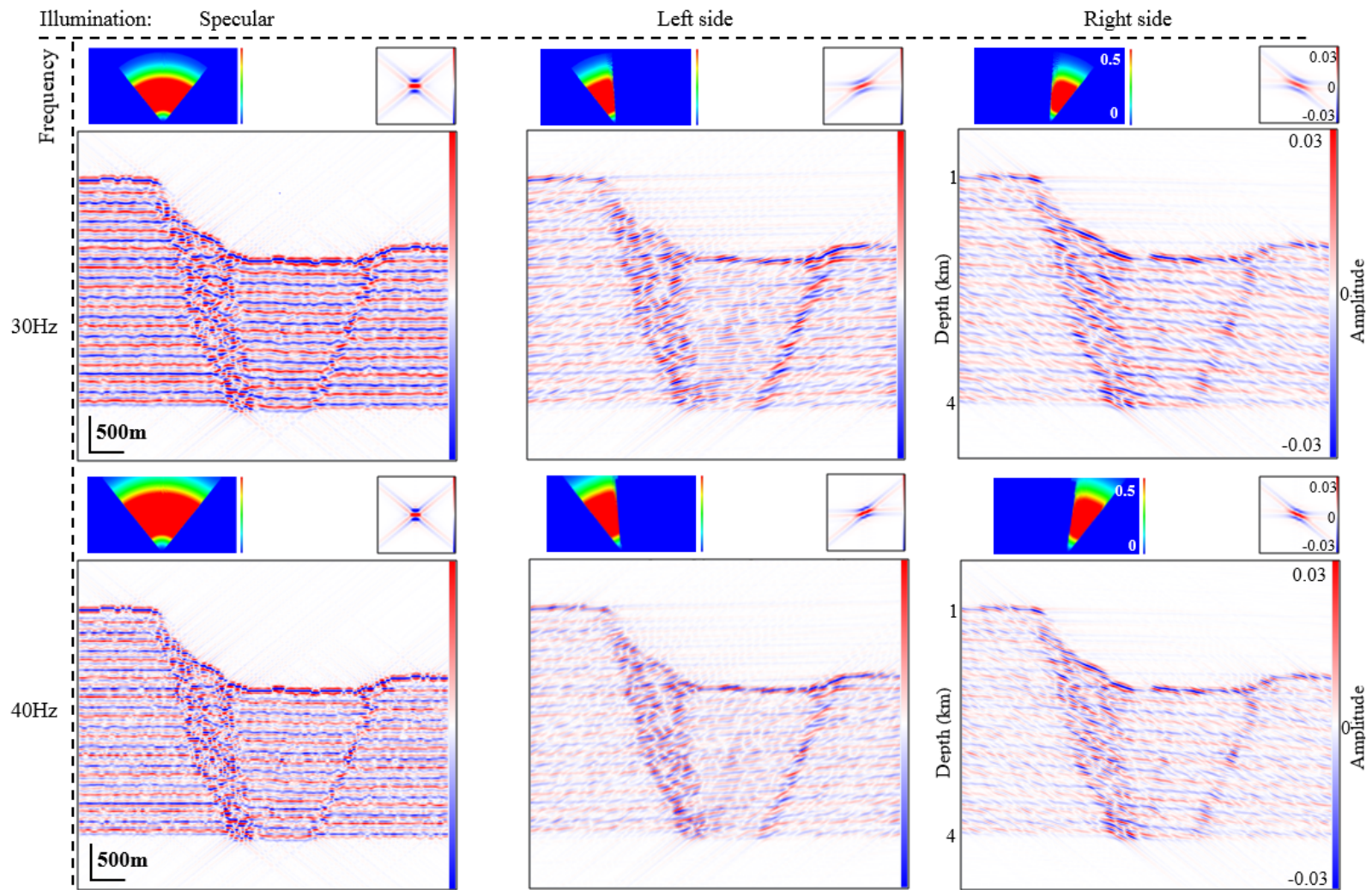
45

3.3.1.2 Model 2

The specular illumination at all evolutionary stages of this model show that the flat reflectors outside the fault locations are well imaged (Figures 33 to 40). Therefore the salt-siliciclastic and shale-sandstone interfaces are well imaged in these areas. At a low frequency of 10 Hz, the salt-siliciclastic and shale-sandstone interfaces are difficult to distinguish, due to the reflectors large width, indicating its low resolution. At a low frequency of 10 Hz, using specular illumination the reflectors at the fault zones are curved and continuous, therefore could potentially be misinterpreted as folding instead of faulting (Figures 33, 35, 37, and 39). In comparison, at higher frequencies of 20 to 40 Hz, using specular illumination, faulting is more distinguishable due to reflector offsets. With the use of specular illumination, although the fold and faults are evident by the offset of reflectors, these structures remain poorly imaged. Therefore, offside illuminations are required, as these illumination directions directly target the dipping reflectors of the forelimb of the forced fold and the internal structure of the fault plane.

The left side illumination generates low amplitude, blurry reflectors of the forced fold, synthetic faults and reverse faults, making difficult to distinguish these structures (Figures 33 to 40). However, additional information is visible from these images. At 1000 m major fault displacement, the left side illumination targets the internal structure of the antithetic fault (fault C2) (Figures 39 and 40). Although a low frequency of 10 Hz, generates low resolution, it can provide additional information. At 500 m major fault displacement, using left side illumination at 10 Hz, the diffracted energy of the side faults (faults A2, B2, F2 and G2) are poorly visible, by an offset in the siliciclastic layers marked by a low amplitude (Figure 35).

Right side illumination targets the dipping reflectors of the forced fold, synthetic faults and reverse faults. The evolution of model 2 on the resultant seismic images indicates that the impact of deformation affects the intensity on the seismic images. For example, according to the geomechanical model (Figure 14b), faults A2, B2, F2 and G2 developed at approximately 350, 450, 400 and 500 m major fault displacement, respectively. Therefore, these secondary faults do not have high amount of displacement at 500 m major fault displacement, hence they don't have a significant impact on the seismic image at the earlier stages of evolution (500 m major fault displacement) in comparison to the later stages (800 and 1000 m major fault displacement) (Figures 35 to 40).

At the later stages of the model evolution (800 and 1000 m major fault displacement), for right side illumination, the synthetic and reverse faults are well imaged, by its high amplitude, showing the internal structure of the fault planes and the salt-siliciclastic and shale-sandstone interfaces (Figures 37 to 40). At 1000 m major fault displacement, using right side illumination, at a low frequency of 10 Hz, the diffracted energy of fault C2 is poorly imaged, marked by a low amplitude (Figures 39). At 1000 m major fault displacement, the right side illumination at high frequencies (20 to 40 Hz) fault C2 is not distinguishable (Figures 39 and 40). This is because the right side illumination does not target antithetic faults. For the right side illumination, the normal faults (faults A2, B2, D2 and E2) are more prominent in the seismic images, in comparison to the reverse faults (faults F2 and G2) (Figures 39 and 40).

At all evolutionary stages of the model, the right side illumination clearly images the forelimb of the forced fold, whilst the two limbs of the fold which remain near horizontal, are poorly imaged due to its low amplitude (Figures 33 to 40). Although the flat reflectors representing the two relatively horizontal limbs of the fold are poorly imaged, the forced fold remains visible with the right side illumination.

In all the evolutionary stages of the model, at a high frequency of 20 to 40 Hz, the reflectors are better defined and there is a strong reflection amplitude of the forced folding, synthetic faults, reverse faults and antithetic fault structure using right side illumination and left side illumination, respectively.

Figure 33: PSDM seismic images of model 2 at 200 m fault displacement. The columns correspond to three different illumination directions: specular (left), left side (center) and right side (right). The rows correspond to two different frequencies: 10Hz (first row) and 20Hz (second row). The PSDM filter and point spread function (PSF) are shown above each seismic image.

Figure 34: PSDM seismic images of model 2 at 200 m fault displacement. The columns correspond to three different illumination directions: specular (left), left side (center) and right side (right). The rows correspond to two different frequencies: 30Hz (first row) and 40Hz (second row). The PSDM filter and point spread function (PSF) are shown above each seismic image.
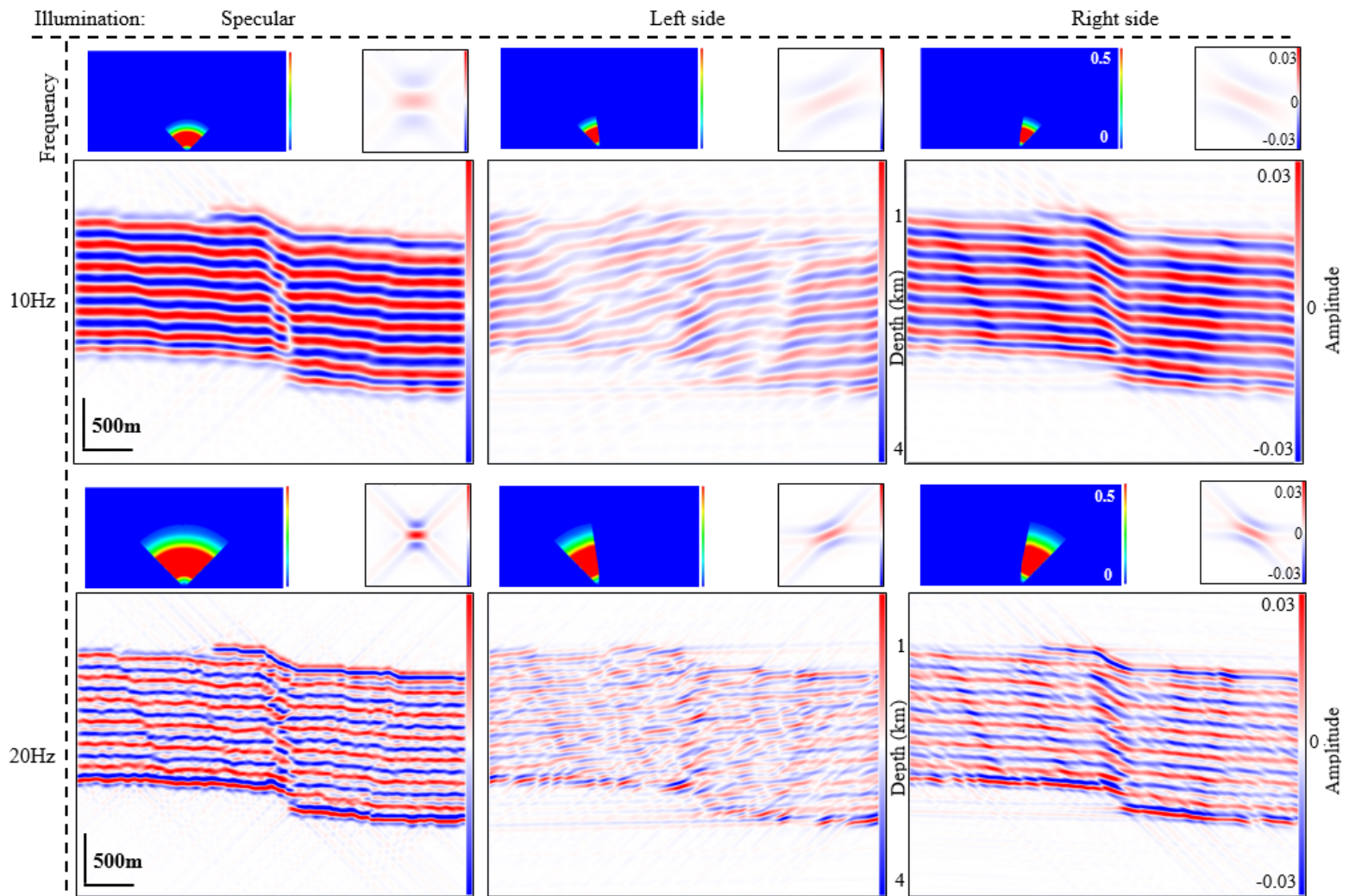
Figure 35: PSDM seismic images of model 2 at 500 m fault displacement. The columns correspond to three different illumination directions: specular (left), left side (center) and right side (right). The rows correspond to two different frequencies: 10Hz (first row) and 20Hz (second row). The PSDM filter and point spread function (PSF) are shown above each seismic image.
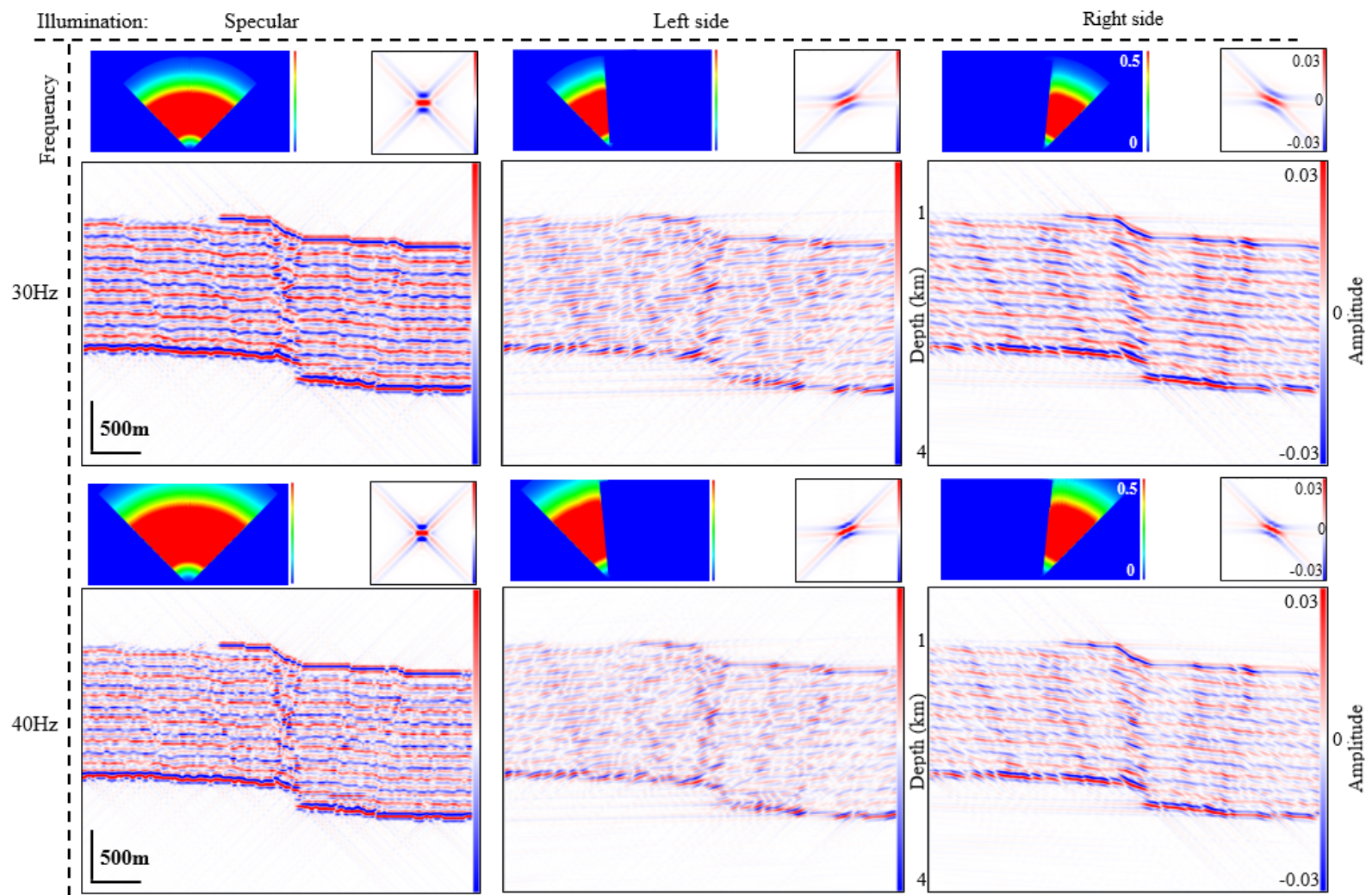
Figure 36: PSDM seismic images of model 2 at 500 m fault displacement. The columns correspond to three different illumination directions: specular (left), left side (center) and right side (right). The rows correspond to two different frequencies: 30Hz (first row) and 40Hz (second row). The PSDM filter and point spread function (PSF) are shown above each seismic image.
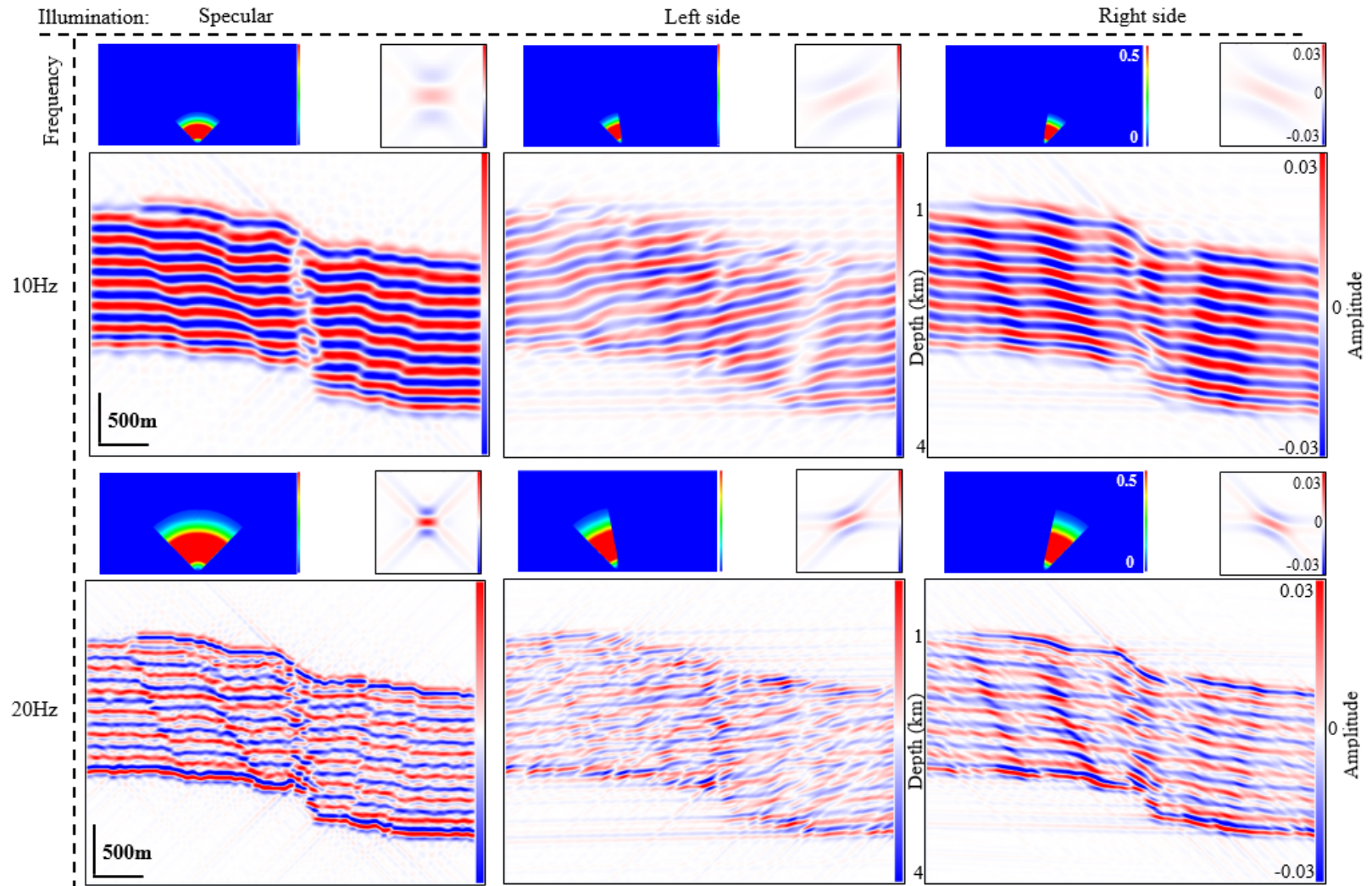
Figure 37: PSDM seismic images of model 2 at 800 m fault displacement. The columns correspond to three different illumination directions: specular (left), footwall side or left side (center) and right side (right). The rows correspond to two different frequencies: 10Hz (first row) and 20Hz (second row). The PSDM filter and point spread function (PSF) are shown above each seismic image.
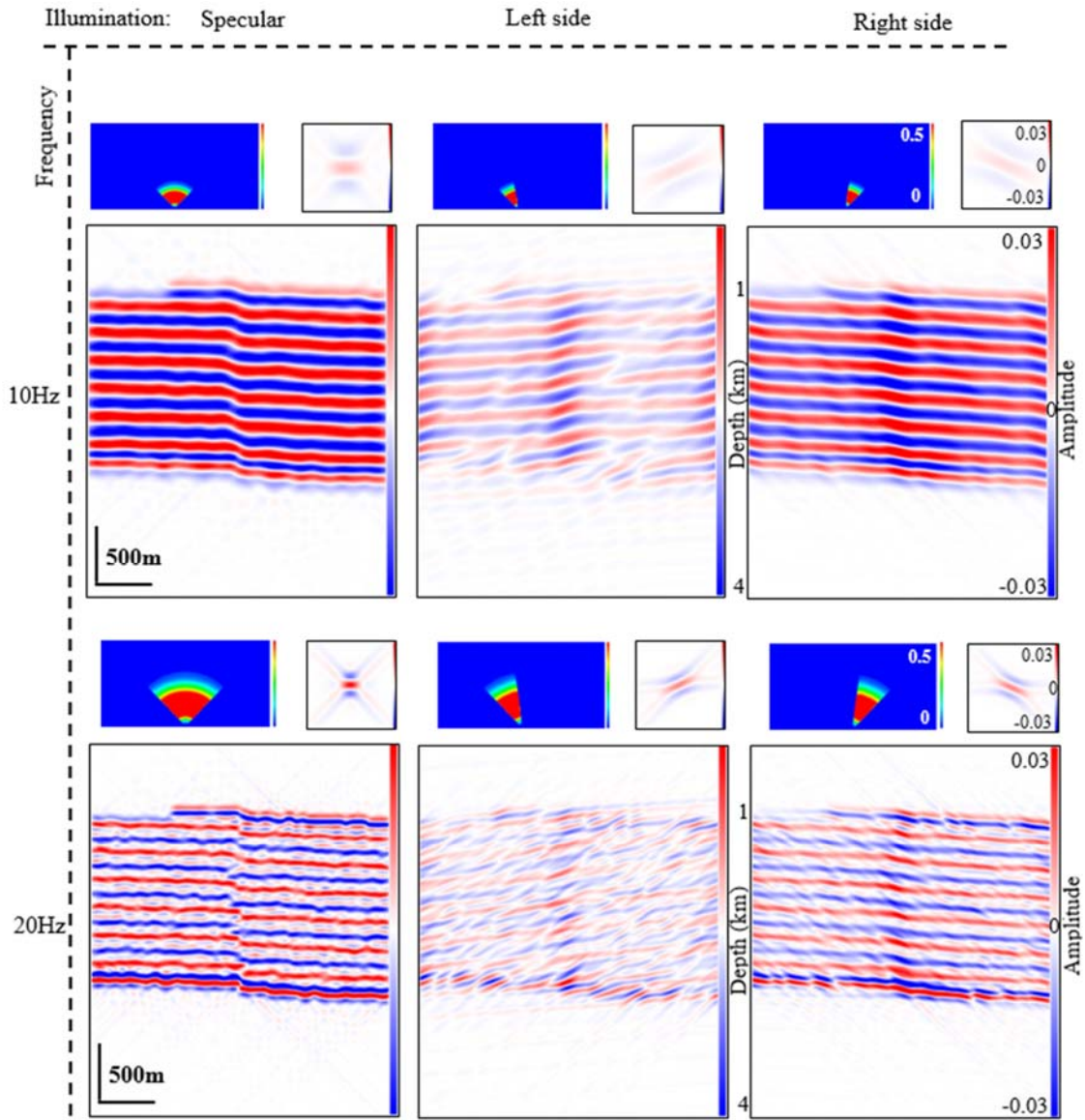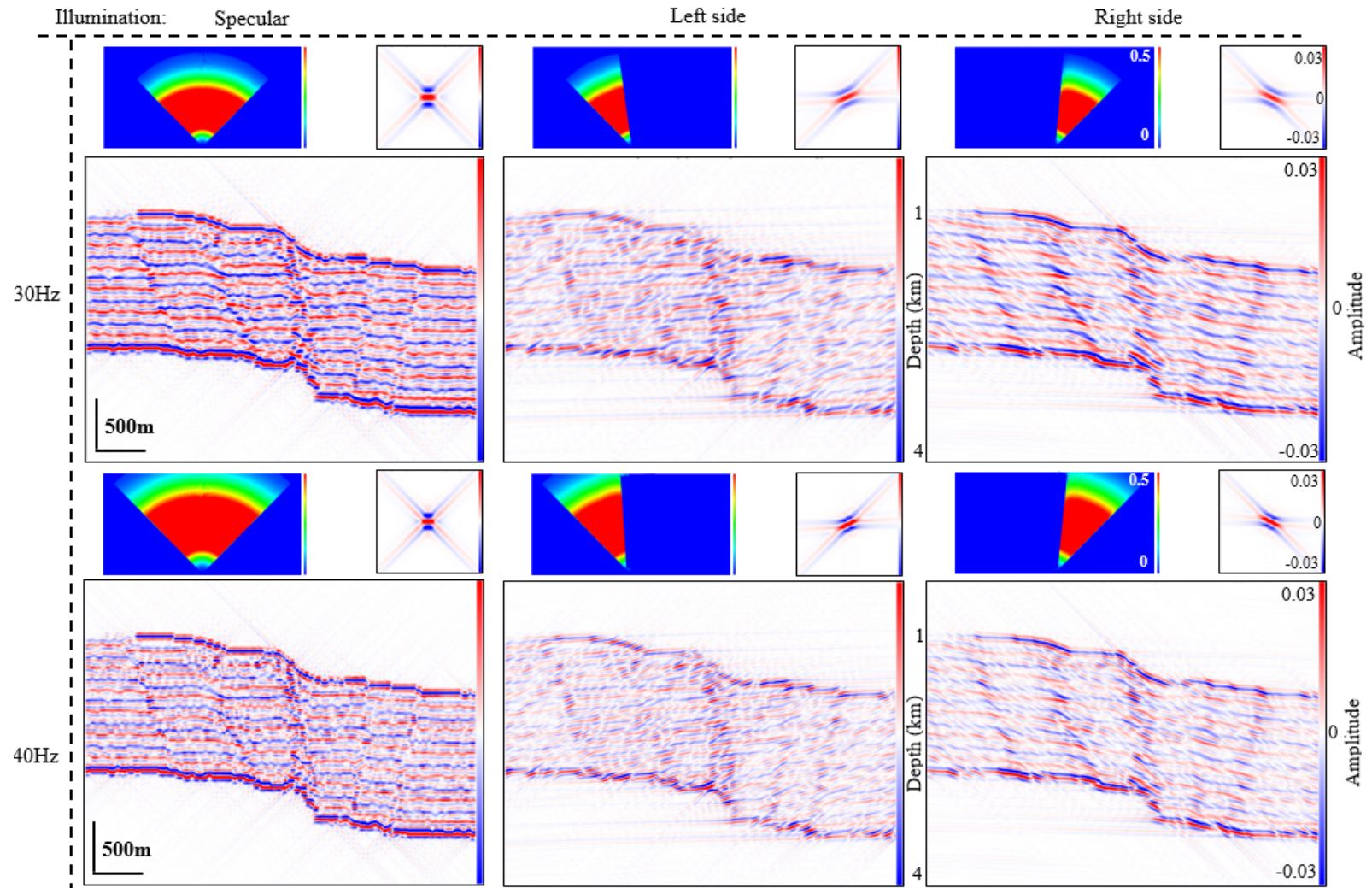
Figure 38: PSDM seismic images of model 2 at 800 m fault displacement. The columns correspond to three different illumination directions: specular (left), left side (center) and right side (right). The rows correspond to two different frequencies: 30Hz (first row) and 40Hz (second row). The PSDM filter and point spread function (PSF) are shown above each seismic image.
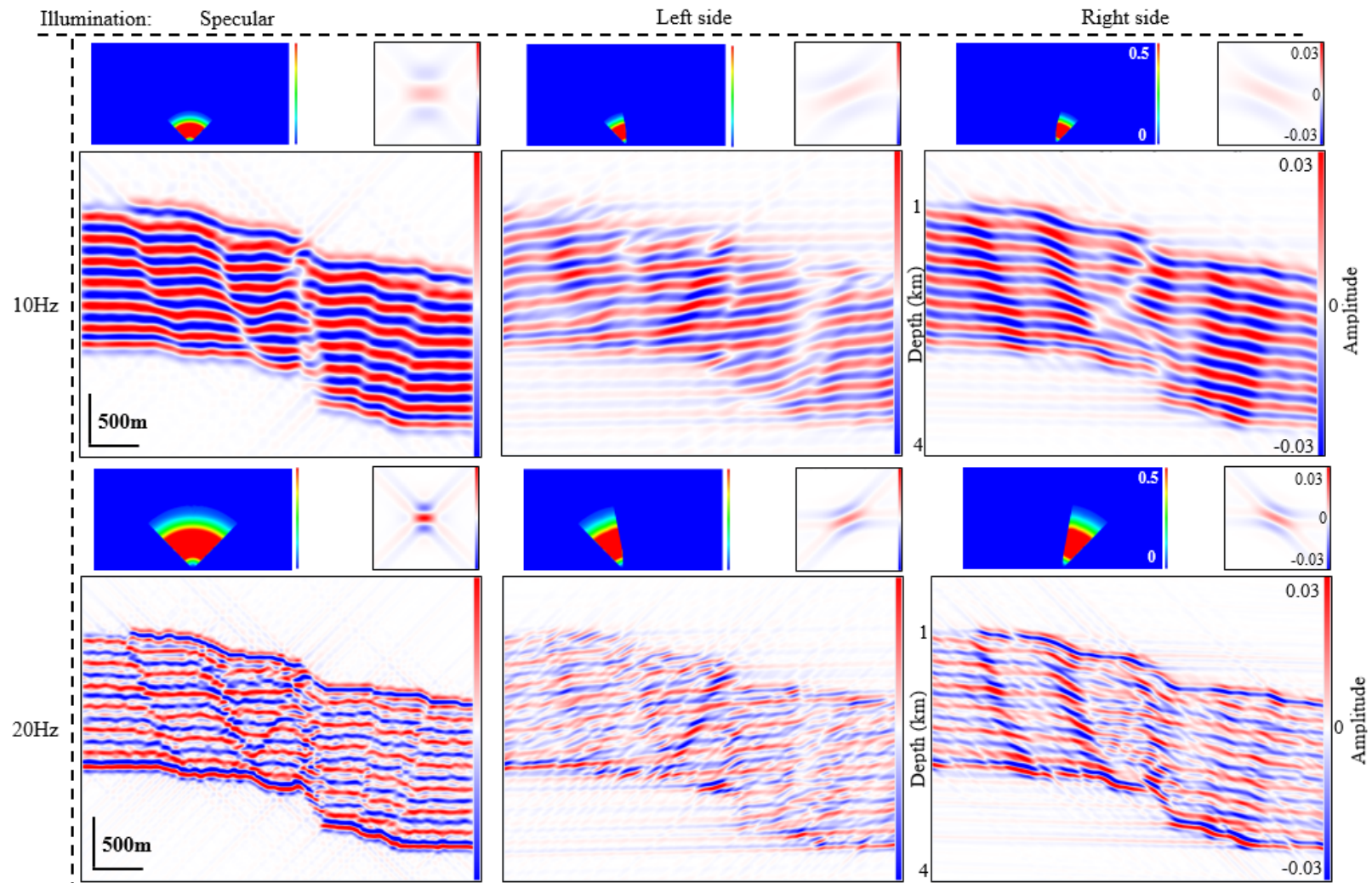
Figure 39: PSDM seismic images of model 2 at 1000 m fault displacement. The columns correspond to three different illumination directions: specular (left), left side (center) and right side (right). The rows correspond to two different frequencies: 10Hz (first row) and 20Hz (second row). The PSDM filter and point spread function (PSF) are shown above each seismic image.
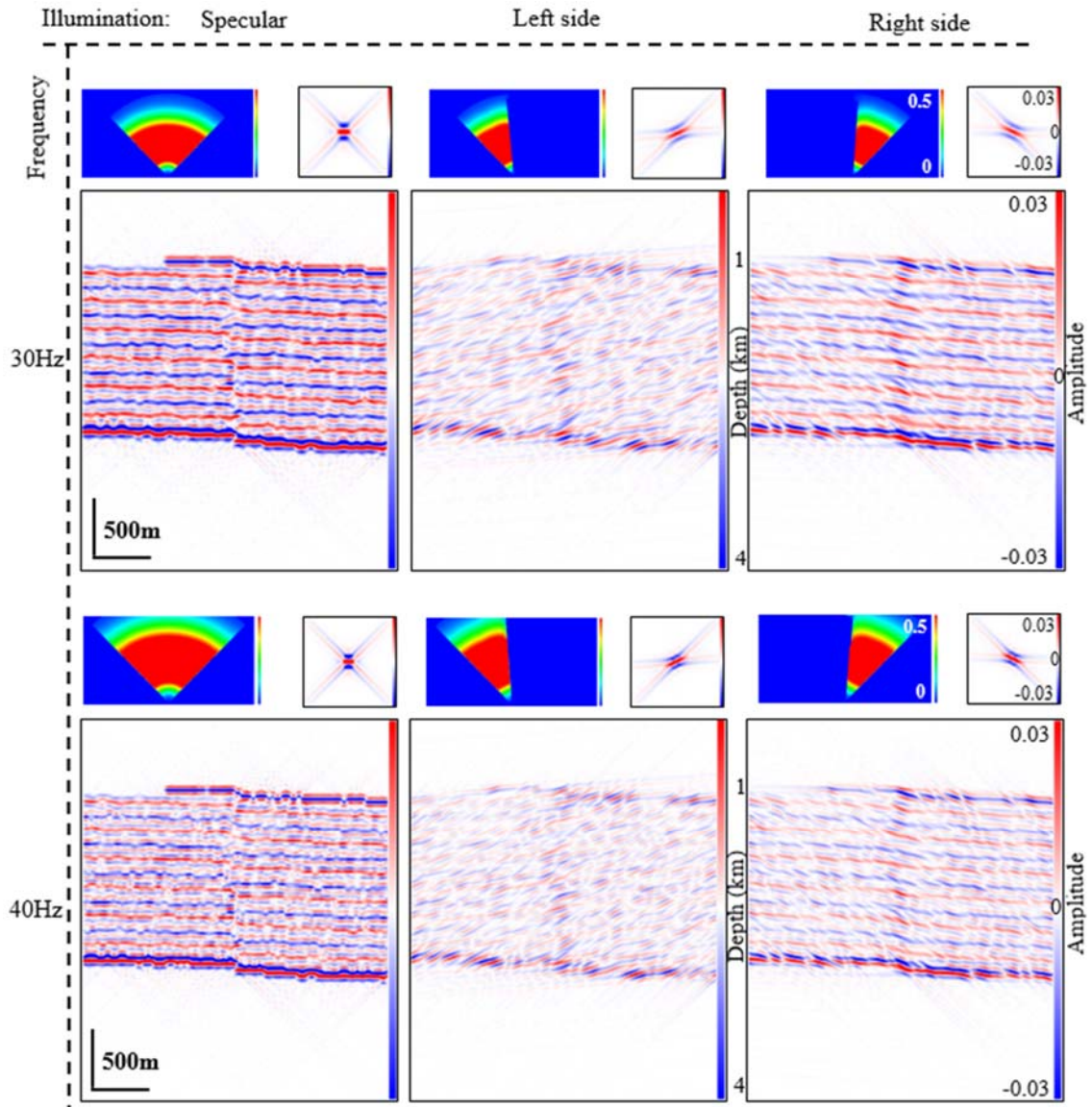
Figure 40: PSDM seismic images of model 2 at 1000 m fault displacement. The columns correspond to three different illumination directions: specular (left), footwall side or left side (center) and hanging wall or right side (right). The rows correspond to two different frequencies: 30Hz (first row) and 40Hz (second row). The PSDM filter and point spread function (PSF) are shown above each seismic image.
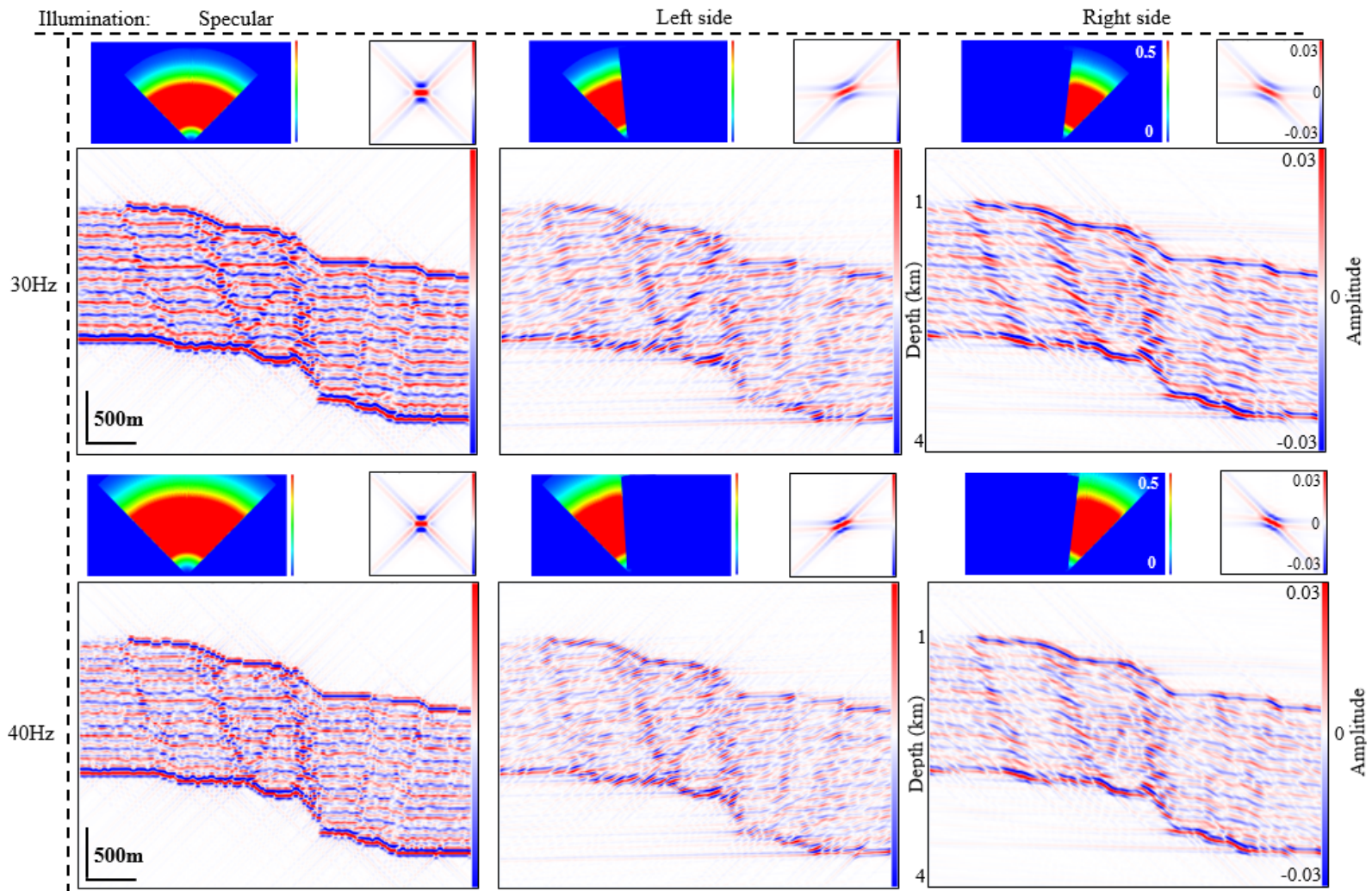
3.3.1.3 Model 3

Growth strata are mostly sub-horizontal, therefore specular illumination images the growth strata clearly (Figures 41 to 48). The offside illuminations do not target the horizontal layers of growth strata, causing low amplitude, weak and blurry reflectors. Growth strata is poorly imaged at a low frequency of 10 Hz, as it generates a low amplitude, blurry and weak reflectors of growth strata, therefore making it difficult to distinguish in the resultant seismic image (Figures 41, 43, 45, and 47). For specular illumination, at high frequencies of 20 to 40 Hz, the horizontal reflectors of growth strata are well imaged, as they are clearly visible, strong and illuminated reflectors (Figures 42, 44, 46, and 48). At 500 m major fault displacement, for specular illumination, since the growth strata are well imaged, the contact between the pre-kinematic sediments (siliciclastic cover sequence) and syn-kinematic sediments (growth strata) are clearly imaged by the onlap of reflectors (Figures 43 and 44). Onlap is distinguished on the resultant seismic image by the termination of low-angle reflectors in the growth strata, against a steeper reflector in the pre-growth, which is the forelimb of the forced fold. The growth strata onlap onto the pre-kinematic sediments is not as visible on the seismic image at 800 and 1000 m major fault displacement, in comparison to 500 m major fault displacement. This is because the increase in major fault displacement at 800 and 1000 m, generates more deformation in the pre-kinematic sediments, which is illustrated in the geomechanical model (Figures 15b and 15c). This increase in deformation makes more difficult to illuminate the contact between the siliciclastic cover sequence and the growth strata.

The specular illumination at all evolutionary stages of the model, image well the flat reflectors outside the fault locations (Figures 41 to 50). At a high frequency of 20 to 40 Hz, of specular illumination, the salt-siliciclastic and shale-sandstone interfaces are better imaged, due to its high resolution. Similarly to model 2, at a low frequency of 10 Hz, using specular illumination the reflectors at the fault zones are curved and continuous, therefore could potentially be misinterpreted as folding instead of faulting (Figures 41, 43, 45, and 47). In comparison, at higher frequencies of 20 to 40 Hz, using specular illumination, faulting is more distinguishable due to reflector offsets, therefore fault-related diffractions are visible (Figures 41 to 50). An anticline is located in the hanging wall of model 3 at 800 and 1000 m major fault displacement (Figures 45 to 48). The anticline is evident in the growth strata and

56

siliciclastic layer assemblage. The anticline is not visible in the offside illuminations, as these illumination directions did not target both antiformal limbs (Figures 45 to 48).

The left side illumination generates poor images of the forced fold and its associated faults, with low amplitude, weak and blurry reflectors (Figures 41 to 50). This is because the left side illumination does not correspond to the direction of the forelimb of the forced fold, synthetic faults (faults A3, B3, C3 and D3), and reverse faults (fault E3). At 500 to 1000 m major fault displacement, for left side illumination, with higher frequencies (30 and 40 Hz), the fault related diffractions are visible, due to its high resolution (Figures 44, 46, and 48).

Right side illumination clearly images the forced fold shown by top reflector dipping, representing the forelimb of the forced fold, whilst the two limbs of the fold which remain horizontal are poorly imaged (Figures 41 to 48). At 200 to 1000 m major fault displacement, the right side illumination targets the internal structure of the fault planes (Figures 41 to 48). For right side illumination, the evolution of model 3, indicates that the impact of deformation affects the intensity on the seismic images. According to the geomechanical model (Figure 15b), faults A3 and E3 developed at ≈ 400 m fault displacement, therefore at 500 m fault displacement, the reflectors of these faults are not dipping enough to have significant impact on the seismic image. Furthermore, fault planes of B3, C3 and D3, for right side illumination at 500 m major fault displacement, are clearly shown by high amplitudes (Figures 43 and 44). This is because, according to the geomechanical model (Figure 15), faults B3, C3 and D3 developed earlier than faults A3 and E3. Therefore at this evolutionary stage of the model, faults B3, C3 and D3 have more displacement, resulting in more deformation, hence having more of an impact on the seismic image.

At the later stages of the model evolution (800 and 1000 m major fault displacement), for right side illumination, the synthetic normal and reverse faults are well imaged, by its high amplitude, evidently showing the internal structure of the fault planes, and the salt-siliciclastic and shale-sandstone interfaces (Figures 45 to 48). Similarly to model 2, the right side illumination images the normal faults (faults A3, B3, C3 and D3) having higher amplitude values in comparison to the reverse fault (fault E3) (Figures 47 and 48). This is because there is less strain in the reverse faults and more strain in the normal faults.

The structure resembling a graben at 1000 m major fault displacement are imaged. For specular illumination, faults F3 and G3 have a slight offset in the reflectors. However, it is not very evident as there is only a small displacement of these faults (Figures 49 and 50). The left side illumination targets the dipping reflectors of the fault plane G3, and the right side illumination targets the dipping reflectors of the fault plane F3 (Figures 49 and 50). Faults F3 and G3 have low amplitudes in comparison to the other faults in model 3. This is because these faults are located furthest from the major fault zone, resulting in less displacement. In all three models, the amplitude values seem to correlate with the amount of finite strain. Lower amplitude values are located in the less deformed siliciclastic layers associated with less strain. The higher amplitude values are located in the more deformed siliciclastic layers associated with more strain.

In all evolutionary stages of model 3, at a high frequency of 20 to 40 Hz, the reflectors are better defined and there is a strong reflection amplitude of the forced folding, synthetic normal faults, reverse faults and antithetic faults using right side illumination and left side illumination, respectively.

Figure 41: PSDM seismic images of model 3 at 200 m fault displacement. The columns correspond to three different illumination directions: specular (left), left side (center) and right side (right). The rows correspond to two different frequencies: 10Hz (first row) and 20Hz (second row). The PSDM filter and point spread function (PSF) are shown above each seismic image.

Figure 42: PSDM seismic images of model 3 at 200 m fault displacement. The columns correspond to three different illumination directions: specular (left), left side (center) and right side (right). The rows correspond to two different frequencies: 30Hz (first row) and 40Hz (second row). The PSDM filter and point spread function (PSF) are shown above each seismic image.

Figure 43: PSDM seismic images of model 3 at 500 m fault displacement. The columns correspond to three different illumination directions: specular (left), left side (center) and right side (right). The rows correspond to two different frequencies: 10Hz (first row) and 20Hz (second row). The PSDM filter and point spread function (PSF) are shown above each seismic image.

Figure 44: PSDM seismic images of model 3 at 500 m fault displacement. The columns correspond to three different illumination directions: specular (left), left side (center) and right side (right). The rows correspond to two different frequencies: 30Hz (first row) and 40Hz (second row). The PSDM filter and point spread function (PSF) are shown above each seismic image.
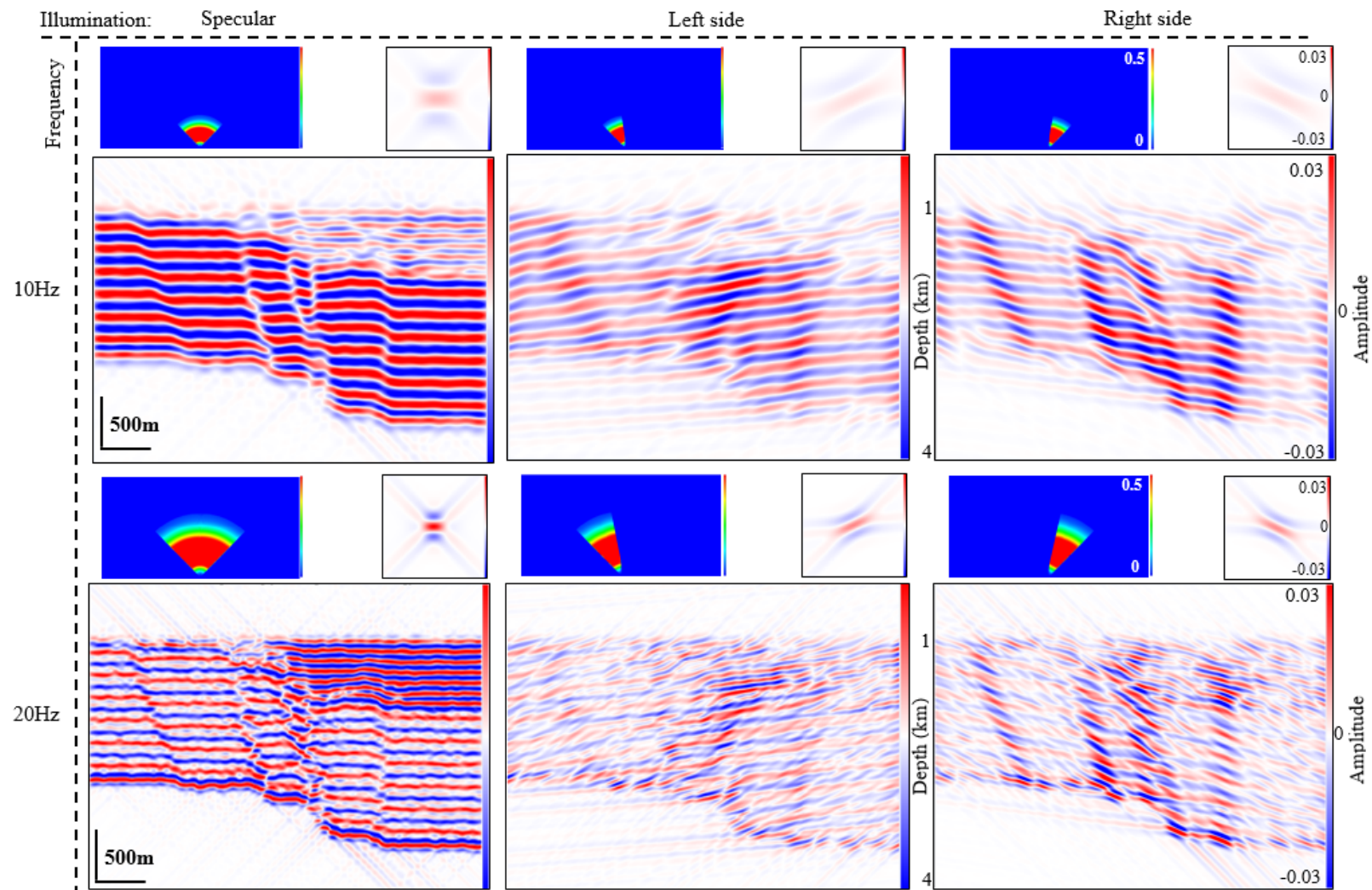
Figure 45: PSDM seismic images of model 3 at 800 m fault displacement. The columns correspond to three different illumination directions: specular (left), left side (center) and right side (right). The rows correspond to two different frequencies: 10Hz (first row) and 20Hz (second row). The PSDM filter and point spread function (PSF) are shown above each seismic image.
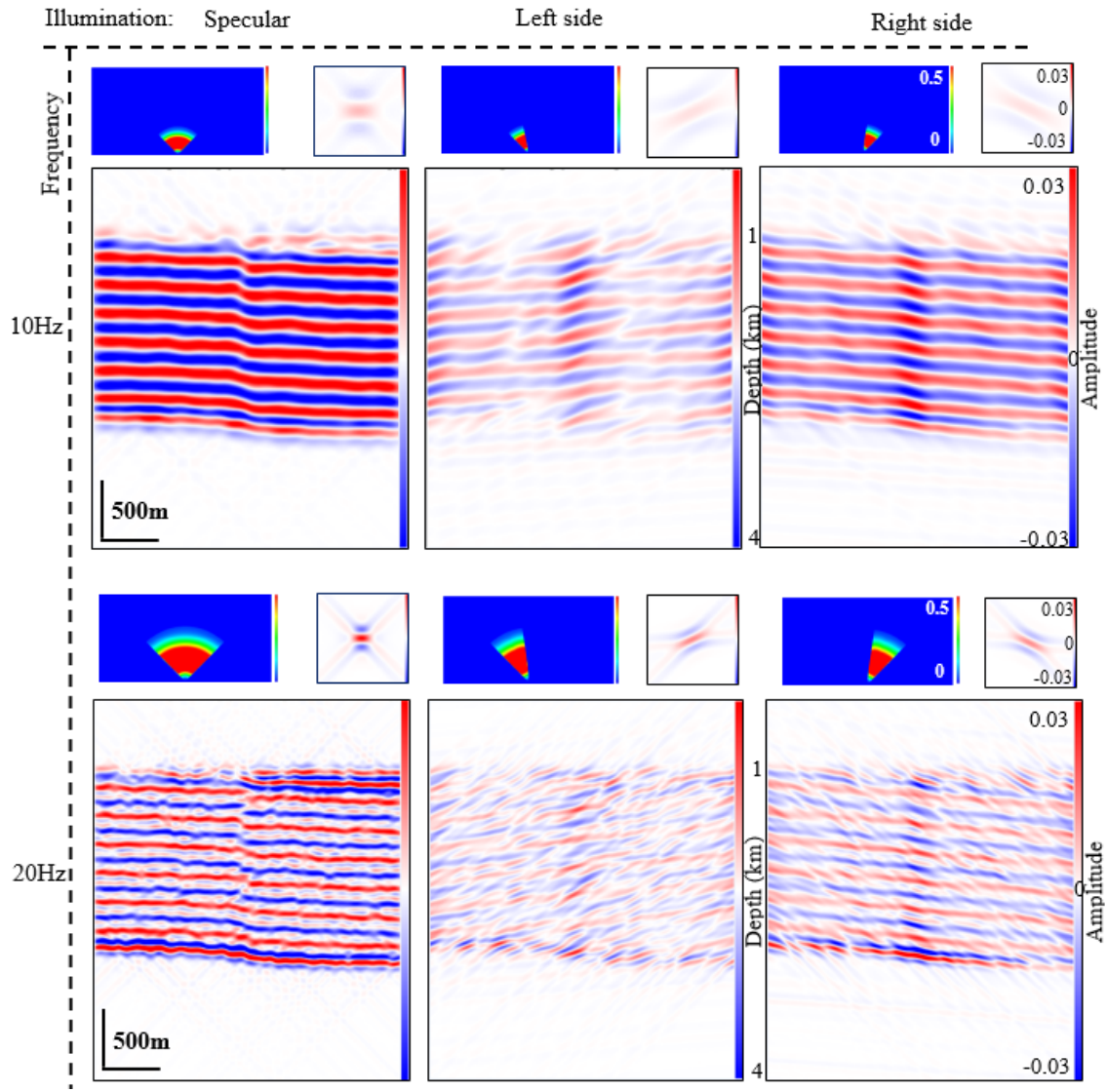
63
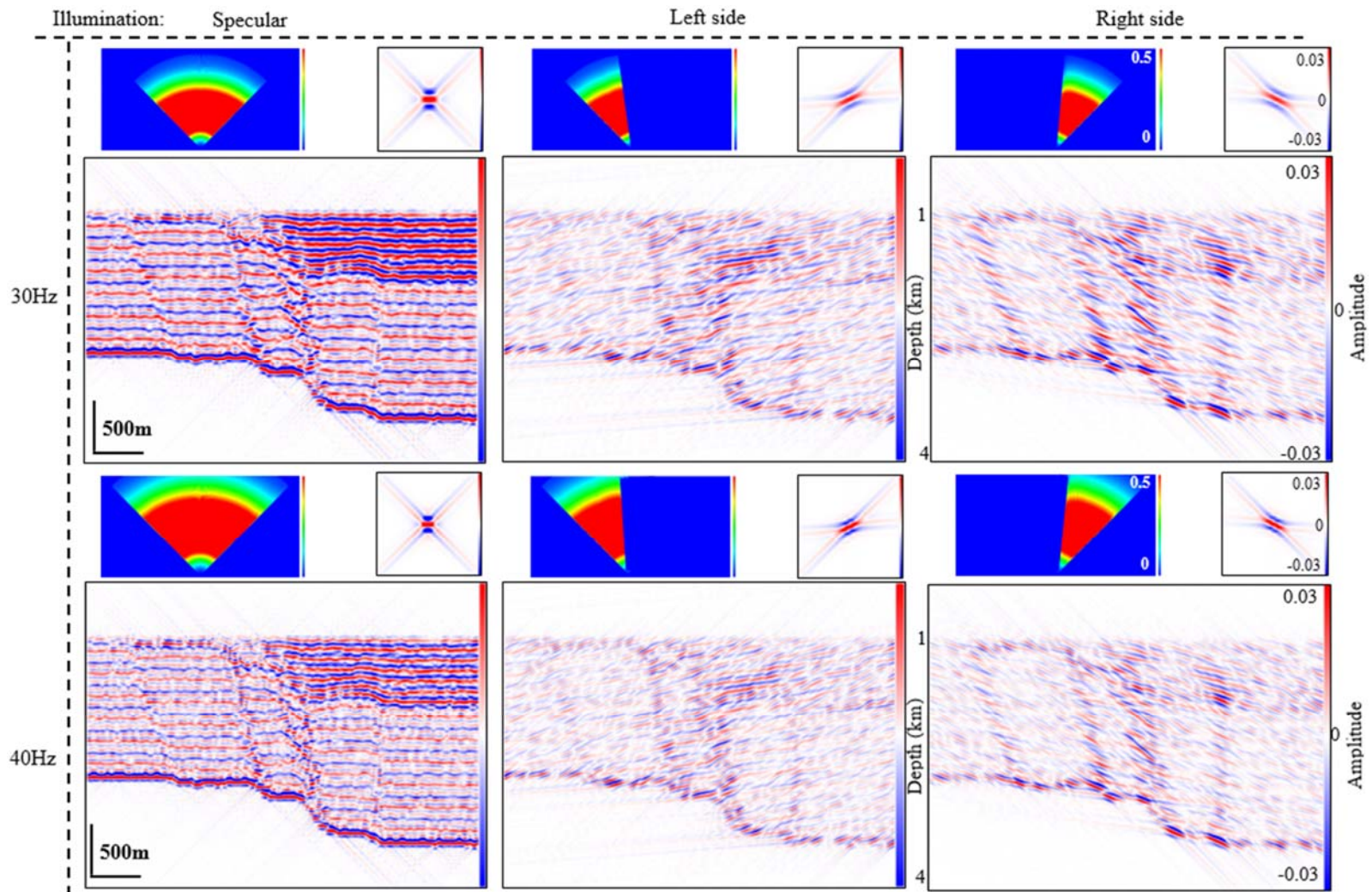
Figure 46: PSDM seismic images of model 3 at 800 m fault displacement. The columns correspond to three different illumination directions: specular (left), left side (center) and right side (right). The rows correspond to two different frequencies: 30Hz (first row) and 40Hz (second row). The PSDM filter and point spread function (PSF) are shown above each seismic image.
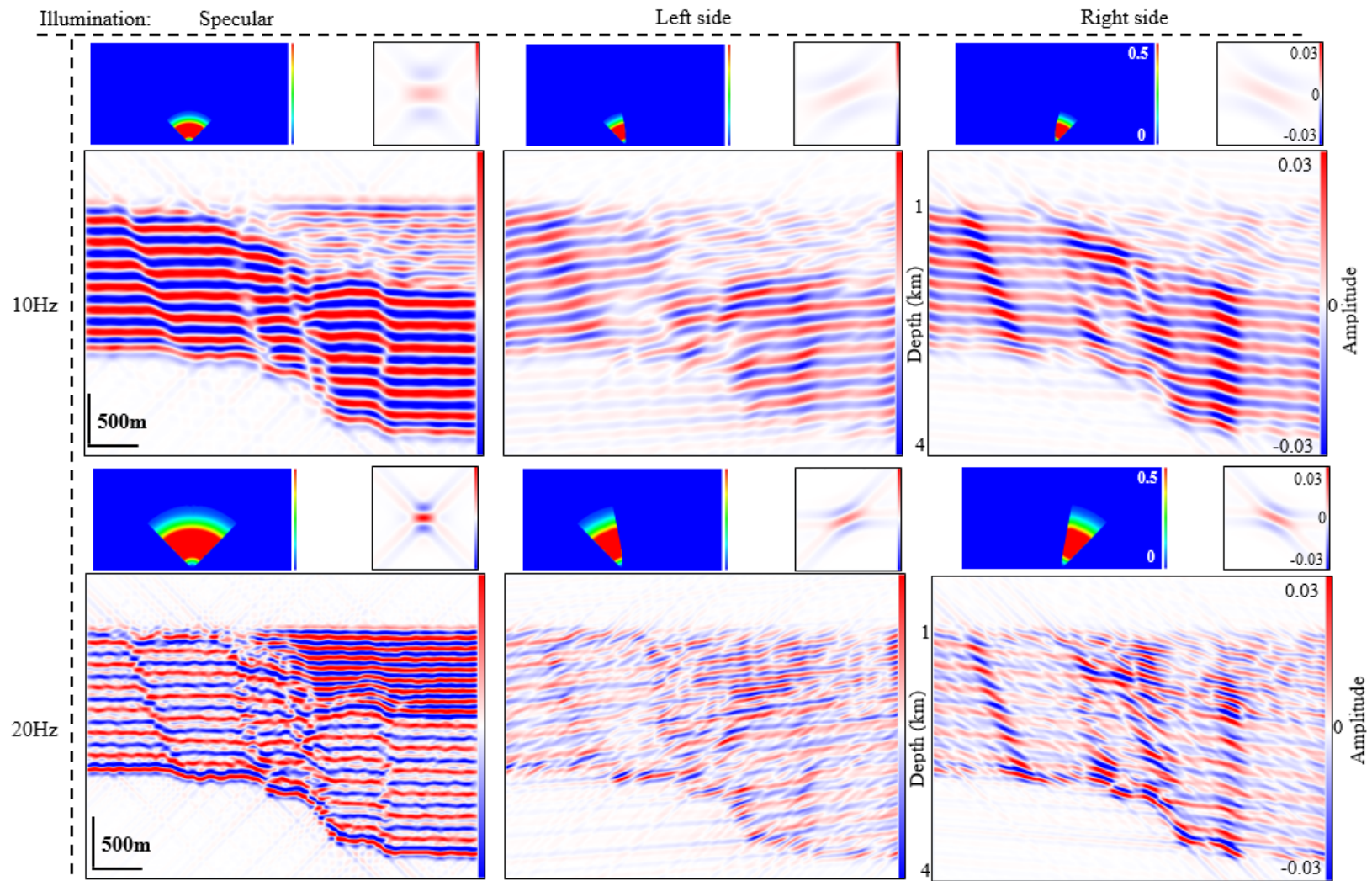
Figure 47: PSDM seismic images of model 3 at 1000 m fault displacement. The columns correspond to three different illumination directions: specular (left), left side (center) and right side (right). The rows correspond to two different frequencies: 10Hz (first row) and 20Hz (second row). The PSDM filter and point spread function (PSF) are shown above each seismic image.
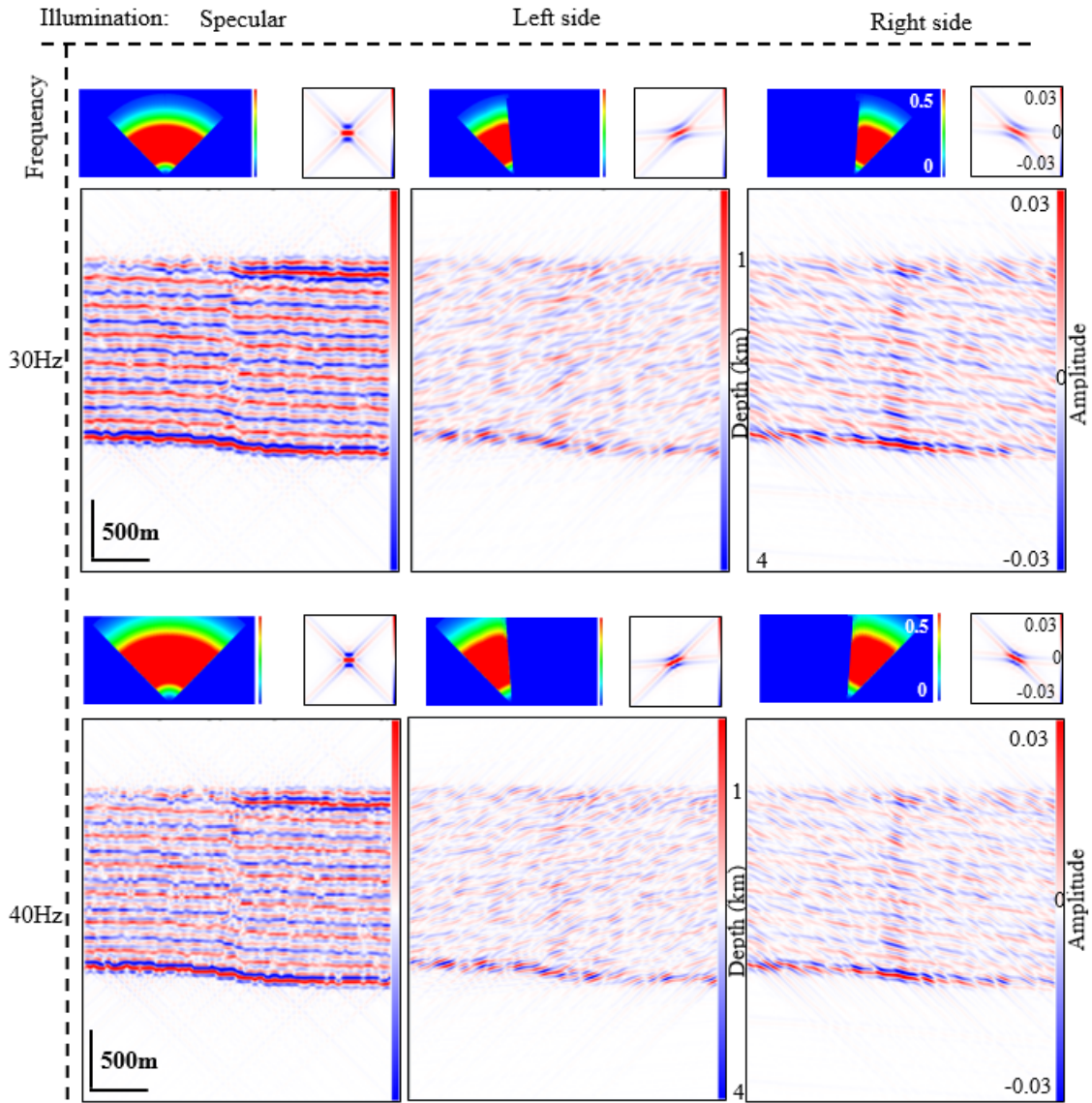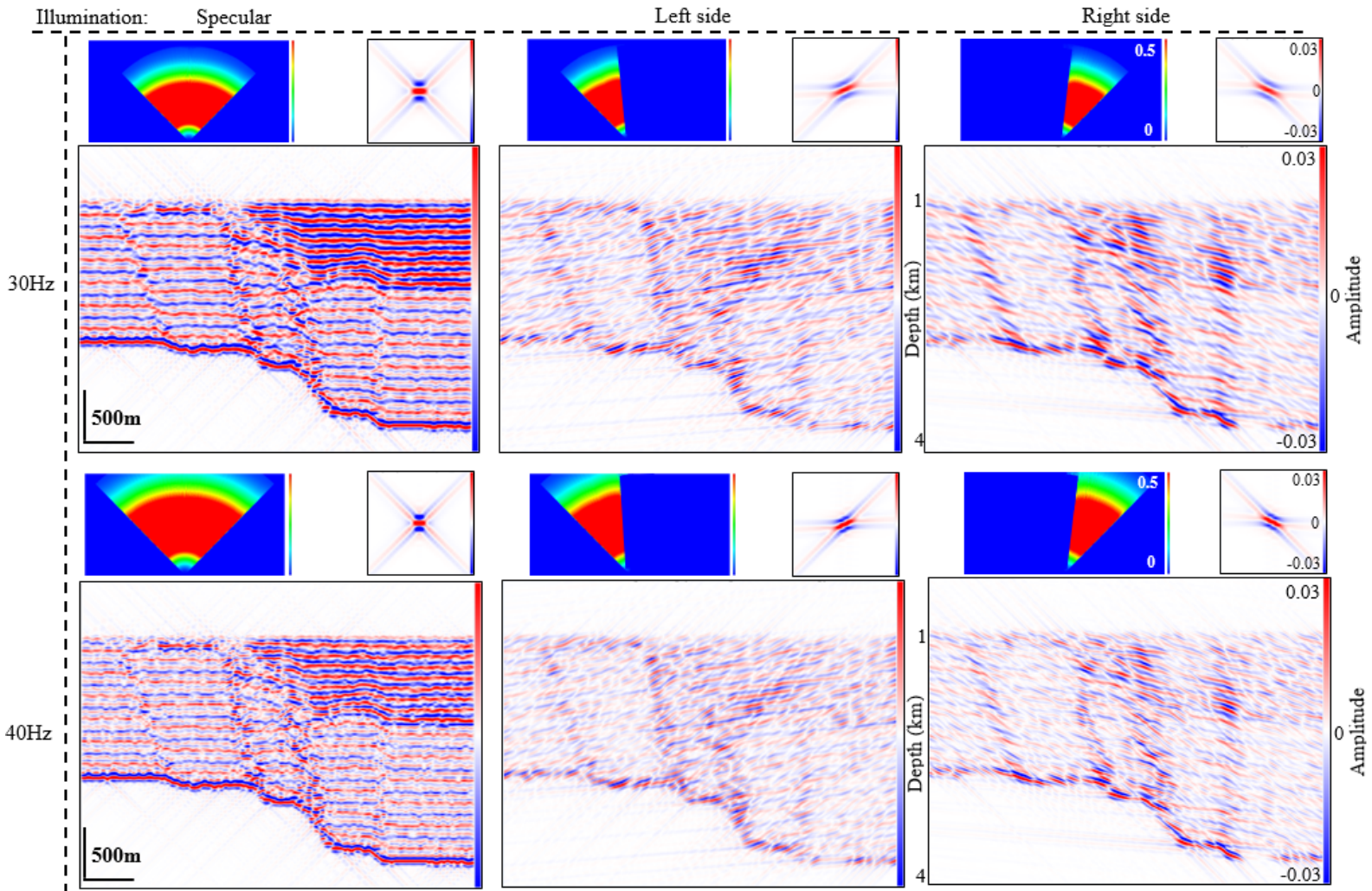
Figure 48: PSDM seismic images of model 3 at 1000 m fault displacement. The columns correspond to three different illumination directions: specular (left), left side (center) and right side (right). The rows correspond to two different frequencies: 30Hz (first row) and 40Hz (second row). The PSDM filter and point spread function (PSF) are shown above each seismic image.
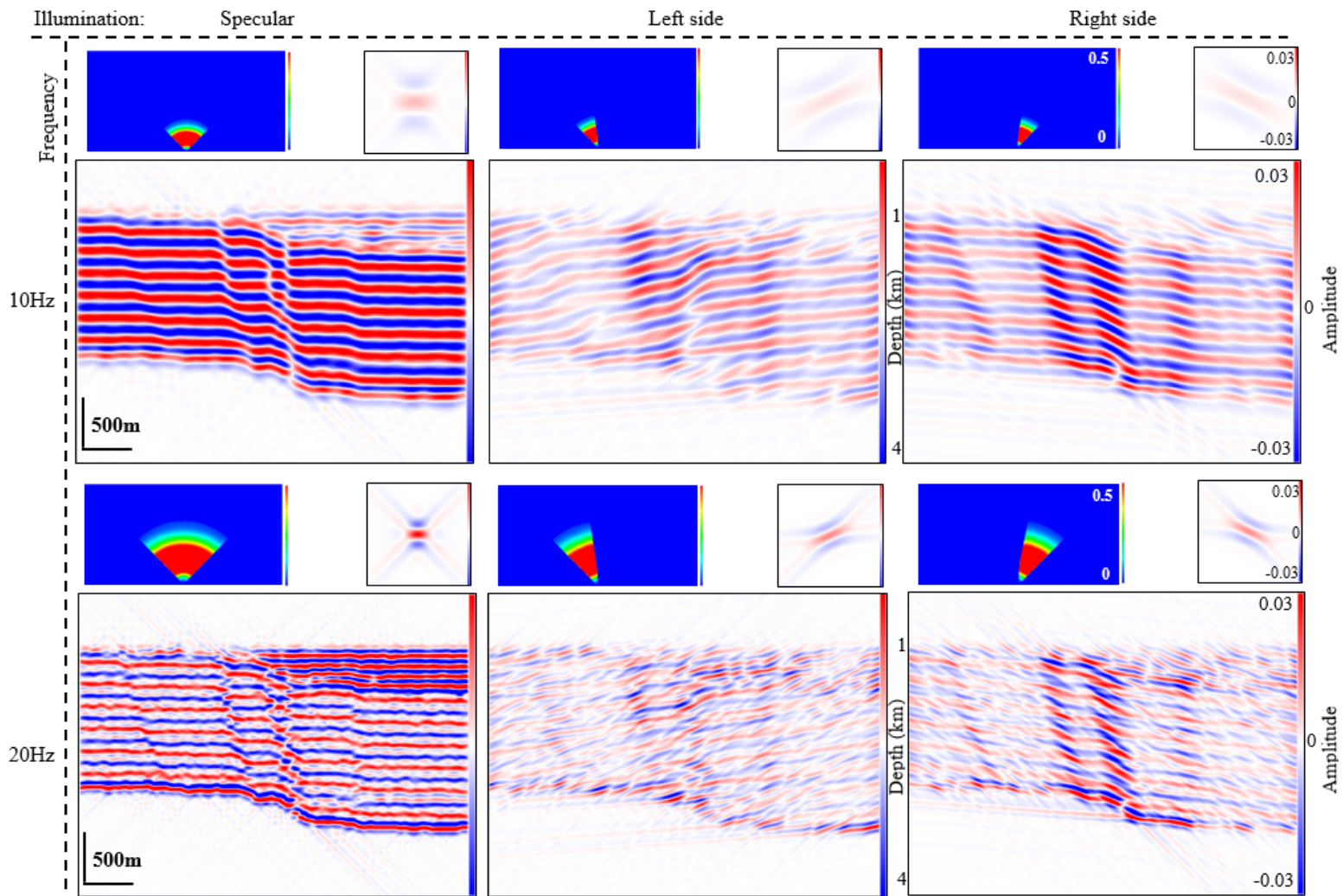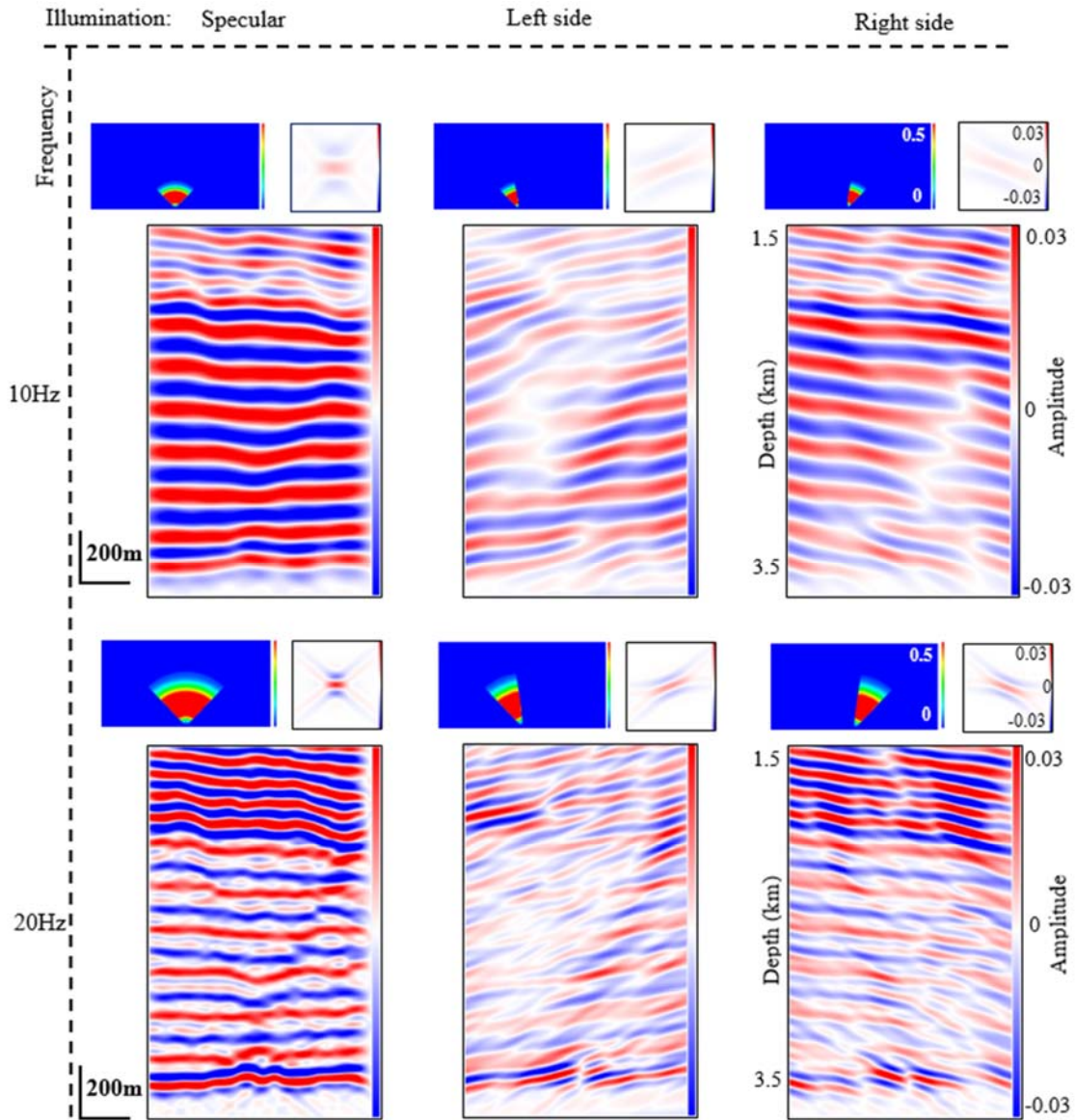
Figure 49: PSDM seismic images of model 3 (Faults F3 and G3) at 1000 m fault displacement. The columns correspond to three different illumination directions: specular (left), left side (center) and right side (right). The rows correspond to two different frequencies: 10Hz (first row) and 20Hz (second row). The PSDM filter and point spread function (PSF) are shown above each seismic image.
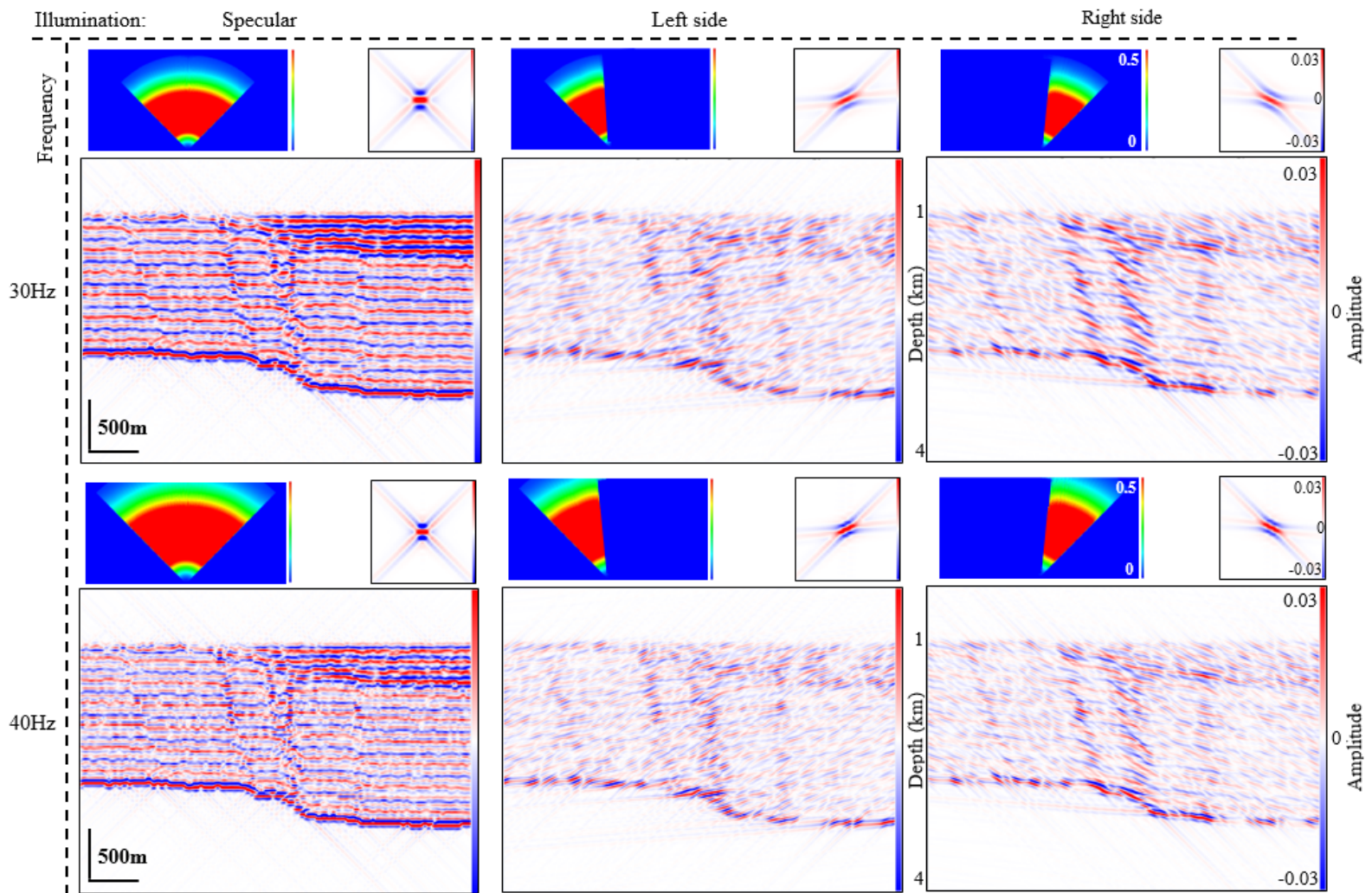
Figure 50: PSDM seismic images of model 3 (Faults F3 and G3) at 1000 m fault displacement. The columns correspond to three different illumination directions: specular (left), left side (center) and right side (right). The rows correspond to two different frequencies: 30Hz (first row) and 40Hz (second row). The PSDM filter and point spread function (PSF) are shown above each seismic image.
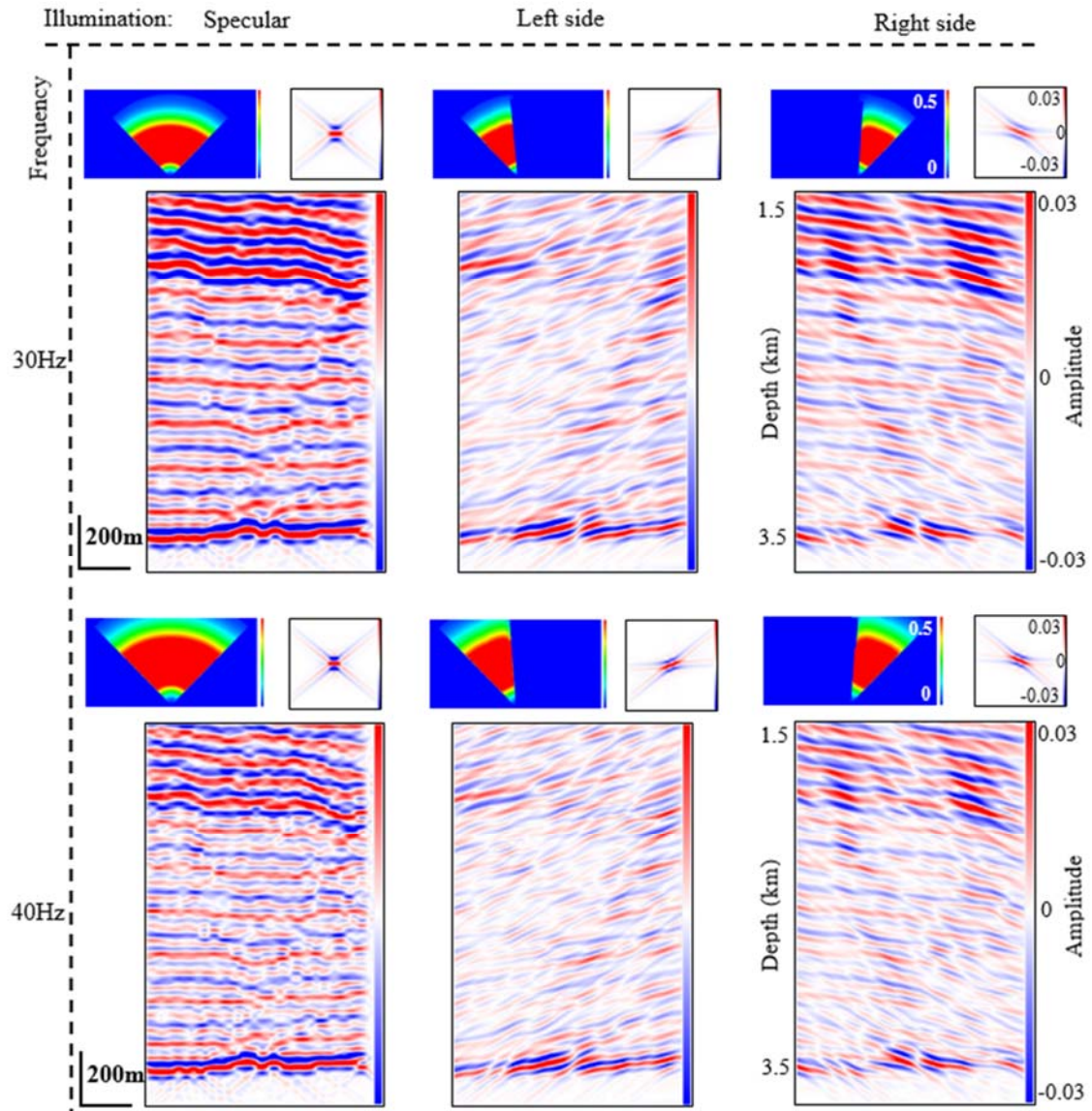
3.3.2 Impact of wave frequency

Wave frequency controls the resolution in the resultant seismic image. The change of resolution due to wave frequency combined with a different illumination direction, e.g., specular, left side or right side, has the potential to generate a better seismic characterization of the forced fold and associated faults. Seismic resolution encompasses two aspects; vertical and horizontal resolution (Chopra et al., 2006). Vertical resolution involves the capability of distinguishing seismic events corresponding to different depths (Chopra et al., 2006). Horizontal resolution involves the capability of distinguishing two laterally displaced features (Chopra et al., 2006). The three models of figures 25 to 50 show that the PSF response indicates the proficiency of the PSDM simulator, providing vertical and lateral resolution effects, angle and direction of the reflectors. The lowest frequency generates the lowest vertical and lateral resolution and vice versa.

The resolution can be calculated using the wavelength (λ), which is velocity (V) divided by frequency (f) (Rafaelsen, 2005). Tables 5 calculates the wavelength, and from this the vertical resolution is also calculated in Table 6. The vertical resolution is defined as the wavelength (λ) divided by four (Rafaelsen, 2005). Table 6 shows that at a lower frequency, the longer wavelength results in a larger vertical resolution in meters. At higher frequencies, there are shorter wavelengths, resulting in a higher resolution, therefore making the interfaces and folding and faulting structures more defined.

Resolution involves distinguishing two separate features that are located close together (Sheriff, 1997). In reference to the models 2 and 3 at 500, 800 and 1000 m major fault displacement, although right side illumination specifically targets fault planes, in regards to faults D2 and E2 (model 2) and faults C3 and D3 (model 3), they can potentially be interpreted as one fault instead of two. According to the geomechanical model, faults D2 and E2 in model 2, and faults C3 and D3 in model 3 are located very closely (Figures 14 and 15). Therefore the offset and dip in reflectors are not clearly defined to separate the two faults.

In models 1, 2 and 3 at a low frequency of 10 Hz, the salt-siliciclastic and shale-sandstone interfaces are difficult to distinguish, and can potentially distort the image of forced folding and faulting structures due to the low resolution. On the other hand, at a high frequency of 20 to 40 Hz, result in a better characterization of forced folding and faulting structures and

growth strata. The geometry and internal structures are better defined at higher frequencies due to its high resolution.

Frequency (Hz)	Wavelength (m)
10	$\lambda = \dfrac{v}{f} = \dfrac{3500 \text{ m/s}}{10 \text{ Hz}} = 350 \text{ m}$
20	$\lambda = \dfrac{v}{f} = \dfrac{3500 \text{ m/s}}{20 \text{ Hz}} = 175 \text{ m}$
30	$\lambda = \dfrac{v}{f} = \dfrac{3500 \text{ m/s}}{30 \text{ Hz}} = 117 \text{ m}$
40	$\lambda = \dfrac{v}{f} = \dfrac{3500 \text{ m/s}}{40 \text{ Hz}} = 87.5 \text{ m}$

Table 5: Calculation of wavelength

Frequency (Hz)	Vertical Resolution (m)
10	$\dfrac{\lambda}{4} = \dfrac{350\text{m}}{4} = 87.5 \text{ m}$
20	$\dfrac{\lambda}{4} = \dfrac{175\text{m}}{4} = 43.8 \text{ m}$
30	$\dfrac{\lambda}{4} = \dfrac{117\text{m}}{4} = 29.3 \text{ m}$
40	$\dfrac{\lambda}{4} = \dfrac{87.5\text{m}}{4} = 21.9 \text{ m}$

Table 6: Calculation of vertical resolution

4 Discussion: Seismic Imaging

The seismic modeling results are essential for the evaluation of which seismic parameters (i.e. illumination direction and wave frequency) generate a better seismic characterization of complex geological structures such as salt-influenced extensional forced folds or faults. Faults are commonly distinguished by the offset of continuous reflectors (Nicholas, 2009), which are observed in the seismic sections using specular illumination. Specular illumination illuminates fault related diffractions, which are important to delimit the extent of faulting (Botter et al., 2014). With the use of specular illumination, although there is recognition of the forced fold and secondary faults, from the offset of reflectors, these structures remain poorly imaged. A seismic distortion zone represents an area of uncertainty, where the seismic response is distorted by imaging problems associated with the high angle faults or steeply dipping limbs of folds (Dutzer et al., 2010). Figure 51a shows an illustration of the seismic distortion zone. The distortion zones are clearly shown at 10 Hz and 30 Hz of specular illumination, marked by a low amplitude (Figure 51b-c). Therefore, changing the illumination direction can help to highlight features that would typically not be visible in seismic. The use of offside illuminations is to target the dipping reflectors, which are the fault planes and steeply dipping limb of the forced fold. Hence, the zone that was previously distorted at specular illumination is evidently imaged by the offside illumination, imaging the internal structure of the faults (Figure 51d).
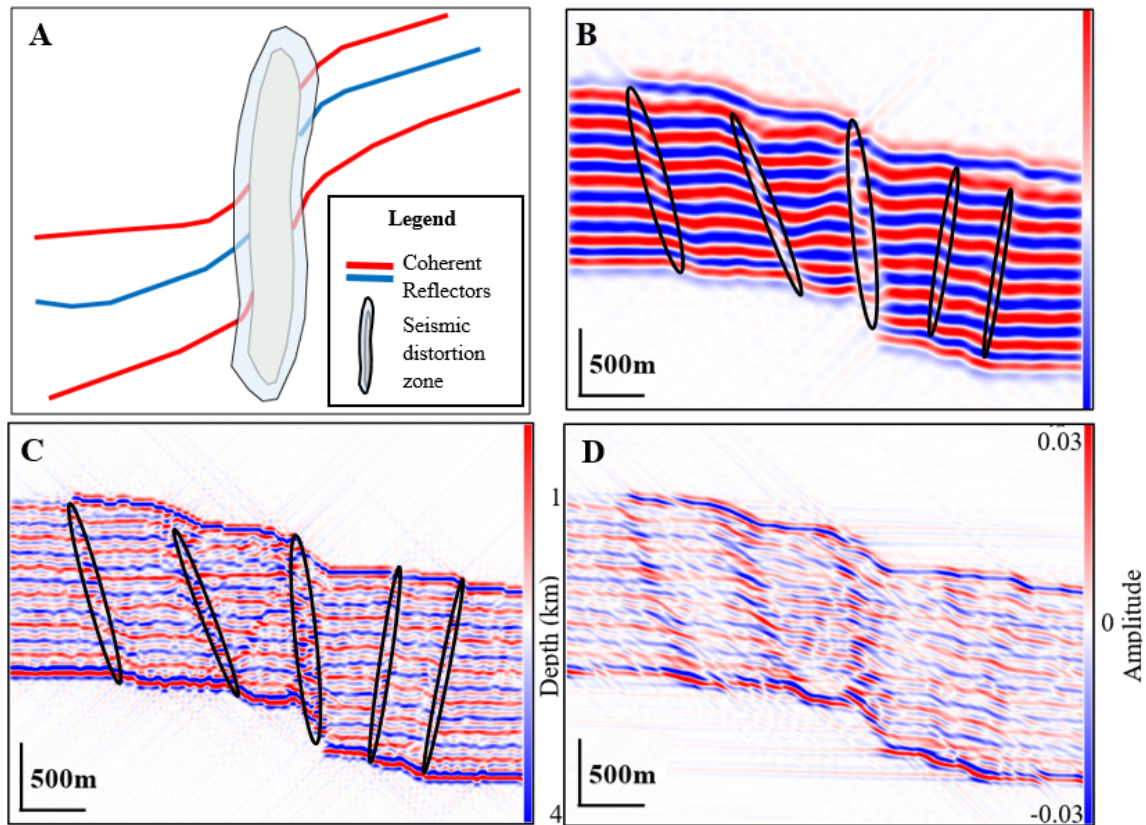
Figure 51: Illustration of seismic distortion zone. (A) Illustration of seismic distortion zone (Modified from Dutzer et al., 2010). Model 2 at 1000 m fault displacement: (B) Specular illumination at 10 Hz: circles highlighting the distortion zone of the faults and steeply dipping limb of the forced fold. (C) Specular illumination at 30 Hz: circles highlighting the distortion zone of the faults and steeply dipping limb of the forced fold. (D) Right side illumination at 30 Hz: evidently imaging the internal structure of the faults and steeply dipping limb of the forced fold.

The workflow shows that the definition and resolution of the forced fold and associated fault architecture have an important effect on the resultant seismic image. In models 1, 2 and 3 higher frequencies (20 to 40 Hz) result in high resolution and better recognition of the forced fold and faults. However, at 30 Hz, faulting in model 1 and the forced fold and its associated faults in models 2 and 3 appear better defined in the resultant seismic images. However, a high resolution does not necessarily mean a better image. At 40 Hz, the seismic images become more unclear, therefore it is challenging to differentiate the fault zone using specular and offside illuminations. Typically, in the North Sea, reservoirs are deeper than 3 km and at this depth it is difficult to obtain frequencies higher than 30 Hz. The maximum depth of models 1, 2 and 3 are 4km, therefore it would be challenging to obtain frequencies higher than 30 Hz. Other parameters which influence the resolution of the forced fold and faults are the overburden and depth. The three models are set at a relatively shallow depth (1 km – 4 km).

Increasing depth results in less seismic resolution, as with increasing depth, frequency decreases, while there is an increase in wavelength (Rafaelsen, 2005). Therefore, if these models were set at a deeper depth, the resultant seismic images would have a poorer seismic resolution.

The following structures are better imaged with the following combination of seismic parameters (i.e. illumination direction and wave frequency):

Extensional Forced Folding

The forced fold is better imaged with right side illumination. This is because the steeper limb of the forced fold is in the direction corresponding to the right side illumination direction. Therefore, a wave frequency of 30 Hz combined with right side illumination generates a better seismic characterization of the forelimb of the forced fold (Figure 52). The relatively horizontal limbs are better imaged at a wave frequency of 30 Hz combined with specular illumination, as this illumination targets flat reflectors.

Secondary Faults

In models 1, 2 and 3, synthetic faults and reverse faults are better imaged with the use of right side illumination and 30 Hz. Left side illumination and 30 Hz generates an enhanced seismic image of the internal structure of the antithetic fault planes: C1, C2, G3 in models 1, 2 and 3, respectively (Figure 52). Therefore, it is important to apply both offside illuminations to determine folding and faulting.
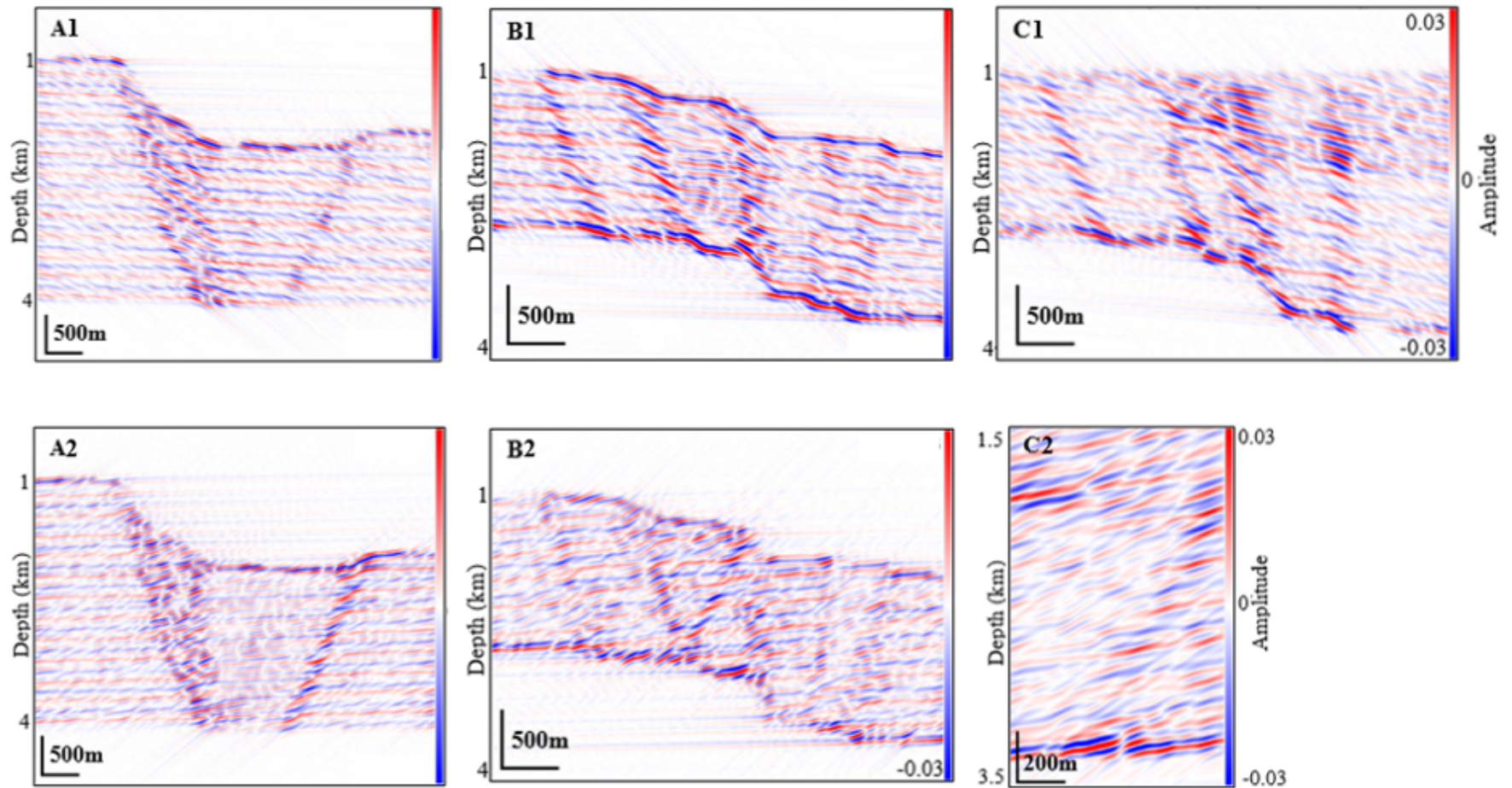
Figure 52: First row: PSDM seismic images of right side illumination and 30 Hz at 1000 m major fault displacement: (A1) Model 1: synthetic faults, (B1) Model 2, (C1) Model 3: synthetic faults and forced folding. Second row: PSDM seismic images of left side illumination and 30 Hz at 1000 m major fault displacement: antithetic faults in (A2) model 1, (B2) model 2, and (C2) model 3.

74

Salt-siliciclastic interface, Shale-sandstone interface and Growth Strata

Specular illumination at 30 Hz, illuminates the flat reflectors, clearly imaging the salt-siliciclastic and shale-sandstone interface and growth strata. A wave frequency of 30 Hz combined with specular illumination generates a better seismic image of the growth strata (Figure 53). There is a stronger amplitude in the growth strata, in comparison to the siliciclastic sediments (Figure 53). This may be due to the growth strata being unconsolidated and therefore their velocities are assumed to be 75% of the velocity values of the pre-growth sandstone and shale.

Anticlinal Fold

Specular illumination evidently images the anticlinal structure in model 3. The anticline is not visible in the offside illuminations, as these illumination directions do not target both limbs and only target reflectors in one specific direction. A wave frequency of 30 Hz combined with specular illumination generates a better seismic image of the anticline (Figure 53).

Figure 53: PSDM seismic image of specular illumination and 30 Hz of growth strata and antiformal fold in model 3 at 1000 m major fault displacement.

5 Conclusions

A synthetic workflow was carried out, similar to that of Botter et al (2014), to analyze the impact of salt-influenced extensional forced folding, its associated secondary faults and seismic parameters on the resultant seismic image. The evolution of forc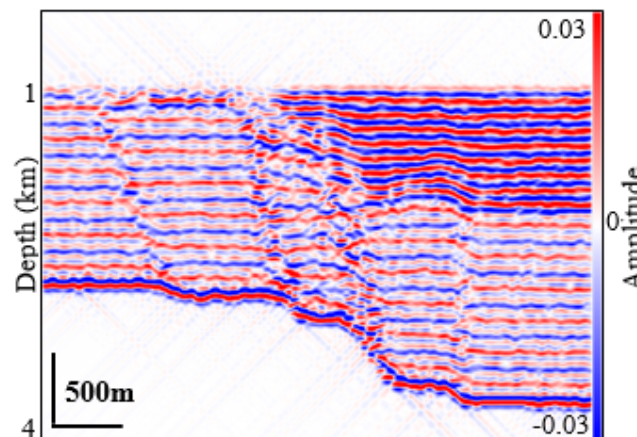ed folding and faulting was simulated with a DEM, allowing the investigation of these structures at large scale and the impact of faulting and folding with the influence of a salt layer and growth strata. The DEM models capture the complex features of forced folding and fault evolution and produce realistic forced fold and fault geometries and strain models. Model 1 consisted of siliciclastic sediments, the deformation was localized above the major fault zone, resembling a graben structure. Model 2 consisted of siliciclastic sediments with salt, the evolution of this model produced a forced fold with a wider distribution of secondary faulting. Model 3 consisted of siliciclastic sediments with salt and growth strata, the evolution of this model produced a steeper forced fold, and a wider distribution of secondary faulting.

Seismic imaging simulation requires an input reflectivity model of elastic properties; density, Vp and Vs. Equations 1-4 allows the computation of the change of seismic properties (density, Vp and Vs) due to finite volumetric strains. Since the structure and properties of the extensional setting are known, it is possible to run sensitivity analyses in the PSDM simulator to potentially improve the resultant seismic images of the forced fold and associated secondary faults. The four different evolutionary stages of the three models were chosen to seismic image. The seismic images show that the more deformation a structure has experienced, the higher the amplitude of the reflectors. This indicates that at later stages of the evolution of the model (i.e. 800 and 1000 m major fault displacement), the structures have more impact on the resultant seismic image. The seismic parameters which are fine-tuned are the illumination direction and wave frequency.

The illumination direction influences how the forced fold and faults can be imaged on seismic. Specular illumination illuminates flat reflectors and fault related diffractions, which are important to delimit the extent of faulting. Offside illuminations target the dipping reflectors which are the internal structure of the forced fold and fault planes. Right side illumination clearly images the forced fold and synthetic faults, reverse faults and left side illumination clearly images the antithetic faults, as it generates relatively high amplitude reflectors of these structures. Wave frequency is the parameter that influences the resolution

of the resultant seismic image. At a low frequency of 10 Hz the forced fold and fault structures appear less defined, due to the low resolution. At higher frequencies of 20 to 40 Hz these structures are more visible. However, at 30 Hz the seismic images are more defined, creating better characterization of forced folds and fault zones.

The combination of seismic parameters (i.e. illumination direction and frequency), allows a better seismic characterization of salt-influenced extensional forced folds and faults. A wave frequency of 30 Hz combined with specular illumination generates a better seismic characterization of the salt-siliciclastic and shale-sandstone interfaces, growth strata and antiformal fold. A wave frequency of 30 Hz combined with left side illumination generates a better seismic characterization of the antithetic faults. A wave frequency of 30 Hz combined with right side illumination generates a better seismic characterization of the forelimb of the forced fold and synthetic faults. The limitation of this study is that the resolution analysis from wave frequency is only based on qualitative interpretation of the seismic image (Laurain et al., 2004). Therefore, in future work, quantitative data can be considered.

Despite the limitations, this study has contributed to improve our knowledge of seismic forced fold and fault characterisation. This study contributes towards an important procedure to evaluate which combination of the two seismic parameters (illumination direction and wave frequency) generate a better seismic characterization of salt-influenced extensional forced folds and faults. This study could help identify, assess and improve poor seismic imaging of extensional forced folding and its associated faults, which is important, as hydrocarbons are generally trapped within secondary structures of extensional forced folds. This work can contribute to better seismic acquisition, imaging, and interpretation of these structures. Future work, can also consider, other seismic parameters, and more complex cases, such as lateral variations in overburden, geological structures at deeper depths, other geological structures in 2D or 3D, and varying lithology to conform to a source, reservoir and seal rock , to potentially produce and evaluate analogue models for a specific reservoir characterisation.

References

Abe, S., Van Gent, H. and Urai, J.L., 2011. DEM simulation of normal faults in cohesive materials. *Tectonophysics*, *512*(1), pp.12-21.

Bjorlykke, K., 2010. *Petroleum geoscience: From sedimentary environments to rock physics*. Springer Science & Business Media.

Botter, C., Cardozo, N., Hardy, S., Lecomte, I. and Escalona, A., 2014. From mechanical modeling to seismic imaging of faults: A synthetic workflow to study the impact of faults on seismic. *Marine and Petroleum Geology*, *57*, pp.187-207.

Cardozo, N. and Allmendinger, R.W., 2009. SSPX: A program to compute strain from displacement/velocity data. *Computers & Geosciences*, *35*(6), pp.1343-1357.

Cardozo, N., Allmendinger, R.W. and Morgan, J.K., 2005. Influence of mechanical stratigraphy and initial stress state on the formation of two fault propagation folds. *Journal of Structural Geology*, *27*(11), pp.1954-1972.

Chopra, S., Castagna, J. and Portniaguine, O., 2006. Seismic resolution and thin-bed reflectivity inversion. *CSEG recorder*, *31*(1), pp.19-25.

Cosgrove, J.W. and Ameen, M.S., 1999. A comparison of the geometry, spatial organization and fracture patterns associated with forced folds and buckle folds. *Geological Society, London, Special Publications*, *169*(1), pp.7-21.

Cundall, P.A. and Strack, O.D., 1979. A discrete numerical model for granular assemblies. *Geotechnique*, *29*(1), pp.47-65.

Dutzer, J.F., Basford, H. and Purves, S., 2010, January. Investigating fault-sealing potential through fault relative seismic volume analysis. In*Geological Society, London, Petroleum Geology Conference series* (Vol. 7, pp. 509-515). Geological Society of London.

Egholm, D.L., 2007. A new strategy for discrete element numerical models: 1. Theory. *Journal of Geophysical Research: Solid Earth*, *112*(B5).

Egholm, D.L., Clausen, O.R., Sandiford, M., Kristensen, M.B. and Korstgård, J.A., 2008. The mechanics of clay smearing along faults.*Geology*, *36*(10), pp.787-790.

Finch, E., Hardy, S. and Gawthorpe, R., 2004. Discrete-element modelling of extensional fault-propagation folding above rigid basement fault blocks.*Basin research*, *16*(4), pp.467-488.

Fossen, H., 2010. Structural geology. Cambridge University Press.

Gray, G.G., Morgan, J.K. and Sanz, P.F., 2014. Overview of continuum and particle dynamics methods for mechanical modeling of contractional geologic structures. *Journal of Structural Geology*, *59*, pp.19-36.

Hardy, S., 2011. Cover deformation above steep, basement normal faults: Insights from 2D discrete element modeling. *Marine and Petroleum geology*,*28*(5), pp.966-972.

Hardy, S. and Finch, E., 2005. Discrete-element modelling of detachment folding. *Basin Research*, *17*(4), pp.507-520.

Hardy, S. and Finch, E., 2006. Discrete element modelling of the influence of cover strength on basement-involved fault-propagation folding.*Tectonophysics*, *415*(1), pp.225-238.

Hardy, S., McClay, K. and Muñoz, J.A., 2009. Deformation and fault activity in space and time in high-resolution numerical models of doubly vergent thrust wedges. *Marine and Petroleum Geology*, *26*(2), pp.232-248.

Jackson, C.A.L., Gawthorpe, R.L. and Sharp, I.R., 2006. Style and sequence of deformation during extensional fault-propagation folding: examples from the Hammam Faraun and El-Qaa fault blocks, Suez Rift, Egypt. *Journal of Structural Geology*, *28*(3), pp.519-535.

Jackson, C.A.L. and Lewis, M.M., 2016. Structural style and evolution of a salt-influenced rift basin margin; the impact of variations in salt composition and the role of polyphase extension. *Basin Research*, *28*(1), pp.81-102.

Jones, I.F. and Davison, I., 2014. Seismic imaging in and around salt bodies. *Interpretation*, *2*(4), pp.SL1-SL20.

Kane, K.E., Jackson, C.A.L. and Larsen, E., 2010. Normal fault growth and fault-related folding in a salt-influenced rift basin: South Viking Graben, offshore Norway. *Journal of Structural Geology*, *32*(4), pp.490-506.

Kearey, P., Brooks, M. and Hill, I., 2002. *An introduction to geophysical exploration*. Blackwell Science Ltd.

Kruggel-Emden, H., Simsek, E., Rickelt, S., Wirtz, S. and Scherer, V., 2007. Review and extension of normal force models for the discrete element method. *Powder Technology*, *171*(3), pp.157-173.

Laurain, R., Vinje, V. and Strand, C. [2004] Simulated migration amplitude for improving amplitude estimates in seismic illumination studies. The Leading Edge, 23(3), 240-245.

Lecomte, I., 2008. Resolution and illumination analyses in PSDM: A ray-based approach. *The Leading Edge*, *27*(5), pp.650-663.

Lecomte, I. and Kaschwich, T., 2008, January. Closer to real earth in reservoir characterization: a 3D isotropic/anisotropic PSDM simulator. In *2008 SEG Annual Meeting*. Society of Exploration Geophysicists.

Lecomte, I., Lavadera, P.L., Anell, I., Buckley, S.J., Schmid, D.W. and Heeremans, M., 2015. Ray-based seismic modeling of geologic models: Understanding and analyzing seismic images efficiently. *Interpretation*, *3*(4), pp.SAC71-SAC89.

Lecomte, I., Lavadera, P.L., Botter, C., Anell, I., Buckley, S.J., Eide, C.H., Grippa, A., Mascolo, V. and Kjoberg, S., 2016. 2 (3) D convolution modelling of complex geological targets beyond–1D convolution. *First Break*, *34*(5), pp.99-107.

Lecomte, I. and Pochon-Guerin, L., 2005. Simulated 2D/3D PSDM images with a fast, robust, and flexible FFT-based filtering approach: 75th Annual International Meeting. In *SEG, Expanded Abstracts* (Vol. 1813).

Lewis, M.M., Jackson, C.A.L. and Gawthorpe, R.L., 2013. Salt-influenced normal fault growth and forced folding: The Stavanger Fault System, North Sea. *Journal of Structural Geology*, *54*, pp.156-173.

Massimi, P., Quarteroni, A., Saleri, F. and Scrofani, G., 2007. Modeling of salt tectonics. *Computer methods in applied mechanics and engineering*, *197*(1), pp.281-293.

Maurin, J.C. and Niviere, B., 1999. Extensional forced folding and décollement of the pre-rift series along the Rhine graben and their influence on the geometry of the syn-rift sequences. *Geological Society, London, Special Publications*, *169*(1), pp.73-86.

Mavko, G., Mukerji, T. and Dvorkin, J., 2009. The rock physics handbook: Tools for seismic analysis of porous media. Cambridge university press.

Nichols, G., 2009. Sedimentology and stratigraphy. John Wiley & Sons.

Rafaelsen, B., 2005. Seismic resolution and frequency filtering. *Mat. Svalex*, pp.1-4.

Ratcliff, D.W., Gray, S.H. and Whitmore Jr, N.D., 1992. Seismic imaging of salt structures in the Gulf of Mexico. *The Leading Edge*, *11*(4), pp.15-31.

Raymer, D.G., Tommasi, A. and Kendall, J.M., 2000. Predicting the seismic implications of salt anisotropy using numerical simulations of halite deformation. *Geophysics*, *65*(4), pp.1272-1280.

Saltzer, S.D. and Pollard, D.D., 1992. Distinct element modeling of structures formed in sedimentary overburden by extensional reactivation of basement normal faults. *Tectonics*, *11*(1), pp.165-174.

Sharp, I.R., Gawthorpe, R.L., Underhill, J.R. and Gupta, S., 2000. Fault-propagation folding in extensional settings: examples of structural style and synrift sedimentary response from the Suez rift, Sinai, Egypt. *Geological Society of America Bulletin*, *112*(12), pp.1877-1899.

Sheriff, R.E., 1997. Seismic resolution a key element. *AAPG Explorer*,*18* (10), pp.44-51.

Sigernes, L.T.W., 2004. Rock Physics of extensional Faults and their seismic imaging Properties (Doctoral thesis, monograph). Norwegian University of Science and Technology, 305 p.

Strayer, L.M., Erickson, S.G. and Suppe, J., 2004. Influence of growth strata on the evolution of fault-related folds—distinct-element models. Thrust tectonics and hydrocarbon systems: AAPG Memoir 82, pp. 413–437.

Strayer, L.M. and Suppe, J., 2002. Out-of-plane motion of a thrust sheet during along-strike propagation of a thrust ramp: a distinct-element approach.*Journal of Structural Geology*, *24*(4), pp.637-650.

Suppe, J., Chou, G.T. and Hook, S.C., 1992. Rates of folding and faulting determined from growth strata. In *Thrust tectonics* (pp. 105-121). Springer Netherlands.

Tavani, S. and Granado, P., 2015. Along-strike evolution of folding, stretching and breaching of supra-salt strata in the Plataforma Burgalesa extensional forced fold system (northern Spain). *Basin Research*, *27*(4), pp.573-585.

Vendeville, B.C., Ge, H. and Jackson, M.P.A., 1995. Scale models of salt tectonics during basement-involved extension. *Petroleum Geoscience*, *1*(2), pp.179-183.

Vidal-Royo, O., Hardy, S. and Muñoz, J.A., 2011. The roles of complex mechanical stratigraphy and syn-kinematic sedimentation in fold development: insights from discrete-element modelling and application to the Pico del Águila anticline (External Sierras, Southern Pyrenees). *Geological Society, London, Special Publications*, *349*(1), pp.45-60.

Whipp, P. S., 2011, Fault-propagation folding and the growth of normal faults, PhD., thesis, University of London, 520 p

Wibberley, C.A., Yielding, G. and Di Toro, G., 2008. Recent advances in the understanding of fault zone internal structure: a review. *Geological Society, London, Special Publications*, *299*(1), pp.5-33.

Withjack, M.O. and Callaway, S., 2000. Active normal faulting beneath a salt layer: an experimental study of deformation patterns in the cover sequence.*AAPG bulletin*, *84*(5), pp.627-651.

Withjack, M.O., Meisling, K.E. and Russell, L.R., 1989. Forced folding and basement-detached normal faulting in the Haltenbanken area, offshore Norway. *AAPG Bull.;(United States)*, *72*(CONF-880301-).